

University of Bath



PHD

Signals of Opportunity for Atmospheric Remote Sensing

Goudar, Balsubramani

Award date:
2017

Awarding institution:
University of Bath

[Link to publication](#)

General rights

Copyright and moral rights for the publications made accessible in the public portal are retained by the authors and/or other copyright owners and it is a condition of accessing publications that users recognise and abide by the legal requirements associated with these rights.

- Users may download and print one copy of any publication from the public portal for the purpose of private study or research.
- You may not further distribute the material or use it for any profit-making activity or commercial gain
- You may freely distribute the URL identifying the publication in the public portal ?

Take down policy

If you believe that this document breaches copyright please contact us providing details, and we will remove access to the work immediately and investigate your claim.

Download date: 22. May. 2019

Signals of Opportunity for Atmospheric Remote Sensing

submitted by

Balsubramani Goudar

for the degree of Doctor of Philosophy

of the

University of Bath

Department of Electronics and Electrical Engineering

June 2017

COPYRIGHT

Attention is drawn to the fact that copyright of this thesis rests with its author. This copy of the thesis has been supplied on the condition that anyone who consults it is understood to recognise that its copyright rests with its author and that no quotation from the thesis and no information derived from it may be published without the prior written consent of the author.

This thesis may be made available for consultation within the University Library and may be photocopied or lent to other libraries for the purposes of consultation.

Signature of Author

Balsubramani Goudar

To obtain the crucial information about the boundary layer(Troposphere), there is a need for measurement of large areas($>25,000 \text{ km}^2$) with fine scale measurements of less than 1-2 km area. Over the past years, several methods have been developed to measure atmospheric water vapour fields, but none of them provide information on such small scales($< 1\text{-}2 \text{ km}$). With the recent development of high resolution numerical weather model, the need to provide high temporal and spatial data is ever so significant for proper utilization of the model.

This thesis presents a novel approach to estimate the water vapour/refractivity from the propagation path link delay by using a network of links. We also present in this thesis a different and unique approach to remote sensing of the atmosphere using broadcast free-view TV signals. The theoretical background into the effects of the radio wave propagation through the lower atmosphere has been explored, thereby laying out the issues and shortcomings of existing remote sensing instruments.

The focus of this research is to determine the feasibility of using digital radio and television signals (DVB-T and DAB) data for Tropospheric propagation delay modelling. To estimate the path delay variability of signal propagation through the troposphere we have used the ray tracing approach.

For the estimation of phase delay between the transmitter and receiver, a two dimensional ray tracing algorithm was developed to use different atmospheric remote sensing data to calculate the propagation delay in the troposphere. Statistical analysis of the path delays to showing the variation effects due to different seasons, distance and time has been presented. This thesis further describes the retrieval algorithm which uses the path delay from ray tracing to implement tomography inversion modelling technique. The technique uses a network of path link delays to estimate refractivity. The simulation results obtained from this investigation show that water vapour/refractivity can be estimated from path link delays using tomography reconstruction technique.

ACKNOWLEDGEMENTS

Firstly, I would like to thanks my parents and family for their support and encouragement throughout my Ph.D. I would like to thank my supervisor Dr. Robert Watson for his continuous guidance and support during the course of this study.

I am very grateful to my brother (Devkumar) and my sister in law (Sridevi) for all the help and support during my study.

I am very thankful and would like to acknowledge the financial sponsorship from University of Bath Graduate school towards this research course fees, without which undertaking this course would not have been possible.

I would like to thank the British Atmospheric Data Center(BADC) for providing the data for this research study.

I would also like to thanks my laboratory colleagues and friends (Rania & Mehriyar) for their continued support both inside and outside the research. Finally, I would like to very thankful to my friend Santhseelan for his support and encouragement during my study.

CONTENTS

List of Figures	iv
List of Tables	ix
1 Introduction	2
1.1 Importance of Water Vapour	2
1.2 Research Background	3
1.3 Research Objectives	4
1.4 Structure of the Thesis	5
2 Background/Literature Review	7
2.1 Tropospheric Refraction	8
2.1.1 Structure of the Atmosphere	8
2.2 Refractive Index to Refractivity	9
2.3 Classification of Types of Delay	11
2.3.1 Atmospheric Propagation Delay	11
2.3.2 Types of Path Length (Actual Path Length Vs Geometric Path)	12
2.3.3 Path Length to Delays(Signal Delay)	13
2.4 Troposphere Delay	14
2.5 History of Water Vapour(refractivity) Measurement Techniques of the Atmosphere	15
2.5.1 Radiosonde	15
2.5.2 Water Vapour Radiometer	16
2.5.3 Microwave Radiometer	17
2.5.4 Water Vapour From GPS	18

2.6	Significance of Tropospheric Modelling	19
2.7	Summary	22
2.8	Overview of the following Chapters	22
3	Signals of Opportunity	23
3.1	Introduction to Broadcast Signals	23
3.2	Features of DAB and DVB Network	24
3.3	DAB/DVB Signal Availability in UK	26
3.4	Experimental Set-up	26
3.5	Methodology and Algorithms Used to Retrieve Refractivity	28
3.5.1	Single Site Autocorrelation/Multiple Site Cross-correlation	28
3.5.2	Pilot Symbol Tracking	30
3.6	Summary	34
4	Ray Tracing	35
4.1	Ray Tracing - A Review	35
4.2	Ray Tracing Schemes	37
4.2.1	Ray Shooting Method	37
4.2.2	Ray Bending Methods(Relaxation Method)	38
4.3	Refractivity Calculation From Atmospheric Parameters	40
4.4	Ray Tracing Approach	40
4.5	Ray Tracing Algorithm	41
4.6	Ray tracing Using Eikonal Equation	44
4.7	Interpolation of Raw Radiosonde Data	47
4.8	Summary	47
5	Path Delay Variational Analysis	48
5.1	Delay Variability and It's Effects on Signals	49
5.2	Ray Tracing Simulation and Analysis	49
5.2.1	Simulation Results Using Tri-linear Synthetic Refractivity Profile Data	49
5.2.2	Ray Caustics and Reflections	55
5.2.3	Ray Tracing Using Radiosonde Data-set Profile Data	57
5.3	Statistical Analysis of the Ray-traced Delay	67
5.4	Delay as a Function of Season	69
5.5	Delay as a Function of Distance	71
5.6	Path Delay Analysis using Moving Average	73

5.6.1	Delay as a Function of the Day	73
5.7	Summary	76
6	Tomography Inversion	77
6.1	Introduction to Tomographic Approach	77
6.2	Background and Procedure	79
6.3	Refractivity Profile Generator Model	80
6.4	Path Integrated Refractivity Retrieval	81
6.5	Inversion Algorithm	84
6.6	Basis Function Using Principle Component Analysis(PCA)	85
6.6.1	Gaussian Basis Function	86
6.6.2	Calculation of PCA Methodology	87
6.7	Tomography Reconstruction Technique	88
6.8	Results And Error Analysis	94
6.8.1	Varying the Number of Basis Function	94
6.8.2	Varying the Number of Links	100
6.9	Summary	103
7	Conclusions & Further Work	105
	References	110

LIST OF FIGURES

2-1	Structure of the Earth's atmosphere layers shown including the region of neutral atmosphere[70]	8
2-2	A typical vertical profile showing the variation of refractivity against height obtained from the Radiosonde datasets.	11
2-3	Typical ray propagation environment showing the comparison between the straight line propagation path and the bent path from the transmitter to receiver	13
2-4	Typical example of a water vapour derived from UK GPS network(Source: Met office UK.	19
2-5	The chart shown above gives different stages of modelling of atmospheric delay	21
3-1	Illustration of an SFN network. Here the transmitters with (-) are closer to the receivers and the transmitters with (—) are the one far away from the receiver and these are the ones with interfering signals [39].	26
3-2	Map from ordinance survey showing location of DAB transmitters in and around the city of Bath.	27
3-3	Illustration of the experimental set-up for sampling and processing of DAB signal.	28
3-4	A typical example showing the illustration of multi-site correlation wherein there are more than one transmitter (Tx_1 and Tx_2) lying on the foci of the ellipse, and a pair of receivers (Rx_1 and Rx_2) to receive the signals from the transmitters.	29

3-5	Illustration of the DAB signal data from showing the pattern of CAZAC synchronization symbol.	30
3-6	Figure(a) represents magnitude and phase of the data recorded at University of Bath from nearest transmitter site Mendip using Single-site autocorrelation of 222.064MHz DAB signal. Part(b)shows the variability of refractivity against time(days) using the data from UK meteorological station data collected at Bristol Airport - 11th July 2012	32
3-7	Figure(a) represents magnitude and phase of the data recorded at University of Bath from nearest transmitter site Mendip using Single-site autocorrelation of 222.064MHz DAB signal. Part(b) shows the variability of refractivity against time(days) using the data from UK meteorological station data collected at Bristol Airport - 12th July 2012	33
4-1	A typical vertical refractivity profile showing variation of refractivity against height.	37
4-2	A typical example of a ray shooting method showing a fan of rays from the transmitter and some rays shown reaching the receiver. .	38
4-3	Example Illustrating the ray tracing using bending method by perturbation of the initial two point path until it satisfies Fermat's principle[31].	39
4-4	Geometrical representation of a ray tracing algorithm.	42
5-1	A vertical refractivity profile for constant refractivity.	50
5-2	A plot showing a vertical refractivity profile for the variation of refractivity with height.	51
5-3	Ray tracing in a constant refractivity with predefined initial conditions.	52
5-4	Illustration of a fan of ray propagating through the atmosphere with varying refractivity conditions - source height = 50m, total range = 2500, maximum height = 300 m, initial angle = 75 degrees, final angle = 120 degrees, angle increment = 1 degrees, step size = 1 and finally the slope of the refractivity was set to 0.001 km. The ducting and the anti-ducting conditions were at 50m and 100m.	53

5-5	Typical example of ray tracing showing a fan of rays through an environment with varying refractivity conditions showing ray caustics and reflections from the surface.	55
5-6	Ray path comparison with a straight line path for a ray shot at an angle of 88 degree, as it propagates through the medium.(Source height: 0.1 km, Total range = 250 km, Max height = 30 km, Initial angle = 88 deg, final angle = 88 deg, step size = 0.05).	57
5-7	A plot showing a vertical refractivity profile using the UK BADC Radiosonde data-set(Variation of refractive index(n) with height(m)).	58
5-8	Another example of a two ray traced signals using the radiosonde data set through an environment with varying refractivity, where green line represents straight line propagation with no refractivity and red line represents shows bending due to refractivity	59
5-9	A fan a rays propagating through the environment with varying refractivity conditions, where the green line indicates a straight line path and red line indicates ray traced path.	60
5-10	Illustration of the refractive index profile for the simulation results shown in the following figure and refractivity profile was created using the radiosonde data.	61
5-11	An Illustration of a fan of signals ray traced for a specific location from Bath to Mendip through the model of an atmosphere with refractivity conditions obtained using the radiosonde data set. . .	62
5-12	An Illustration of a fan of signals ray traced for a specific location from Bath to Wenvoe through the model of an atmosphere with refractivity conditions obtained using the radiosonde data set. . .	63
5-13	An Illustration of a fan of signals ray traced for a specific location from Bath to Hannington/Ray propagation path from Bath to Hannington.	64
5-14	Statistical analysis of the atmospheric refractivity at Aberporth over the months for year 2008.	68
5-15	Variation of monthly path delay over different years at Aberporth.	70
5-16	Comparison of monthly mean averaged path delay against time(Months) using different ranges(10 km, 15 km & 20 km) for the year 2012 at Aberporth.	72

5-17	Variation of path delay analysis with respect to the mean refractivity for the year 2010 at Aberporth, over different ranges based on number of days.	74
5-18	Illustration of mean averaged daily refractivity through the use of moving averages.	75
6-1	A simple representation of the Inversion process.	78
6-2	The Process Of Tomography Inversion.	79
6-3	Magnitude and phase recorded at University of Bath from the nearest transmitter site Mendip using the Single-site autocorrelation of 222.064MHz DAB signal is shown in part(a). Lower part(b) shows the refractivity data from the UK meteorological station data at Bristol Airport	83
6-4	An Illustration showing the quality of the path link coverage over an area.	89
6-5	An Illustration of the steps for the overall process of the reconstruction inversion methodology.	90
6-6	Comparison analysis between the original and the reconstructed refractivity field.	91
6-7	Illustration showing the comparison analysis between the original and the reconstructed refractivity field.	92
6-8	Illustration of the inversion methodology, here the left part of the Figure shows link and pixel intersection (R) & the right part of Figure represents the 4 orthogonal basis function(P)	93
6-9	Case 1: Illustration of the reconstruction on a 100×100 scale with number of link = 100 and the min scale of the basis function = 5.	95
6-10	Case 2: Illustration of the comparison analysis of refractivity reconstruction from the original field on a 100×100 scale with number of link = 100 and the min scale of the basis function = 7.	96
6-11	Case 3: Illustration of the comparison analysis of refractivity reconstruction from the original field on a 100×100 scale with number of link = 100 and the min scale of the basis function = 10.	97
6-12	Case 4: Illustration of the comparison analysis of refractivity reconstruction from the original field on a 100×100 scale with number of link = 100 and the min scale of the basis function = 15.	98

6-13	RMS error analysis of the reconstruction field with the basis function for a 100×100 region.	99
6-14	Illustration of the analysis of refractivity reconstruction from the original field on a 100×100 scale with number of link = 200 and the min scale of the basis function = 7.	101
6-15	Illustration of the analysis of refractivity reconstruction from the original field on a 100×100 scale with number of link = 450 and the min scale of the basis function = 5.	102
6-16	Variation of the mean averaged RMS error of the reconstructed field against the number of links.	103

LIST OF TABLES

2.1	Comparison of horizontal and vertical temporal resolution of various remote sensing instruments.	20
5.1	Analysis and comparison between the different combination of ray angle, range and the step size.	66
6.1	Values of the parameters used for the refractivity profile generation	81

ACRONYMS

AMS	American Meteorological Society
ADC	Analog to Digital Converter
AOA	Angle of Arrival
ASCII	American Standard Code for Information Interchange
BBC	British Broadcasting Corporation
CAZAC	Constant Amplitude Zero-Autocorrelation
DAB	Digital Audio Broadcast
DVB-T	Digital Video Broadcast - Terrestrial
GPS	Global Positioning System
NWM	Numerical Weather Modelling
LOS	Line of Sight
MWR	Microwave Radiometer

MATLAB	Matrix Laboratory
NWP	Numerical Weather Prediction
OFDM	Orthogonal Frequency Division Multiplexing
PCA	Principle Component Analysis
RMS	Root Mean Square Error
SRTM	Shuttle Radar Topography Mission
SFN	Single Frequency Network
WVR	Water Vapour Radiometer
UKV	High Resolution UK Model

1.1 Importance of Water Vapour

The term signal of opportunity for remote sensing of the troposphere refers to the use of opportunistic radio signals DVB/DAB to estimate refractivity(water vapour), as the signal propagates along the path from the transmitter to the receiver. Due to the complex structure of the troposphere and high variation in the water vapour all the signals that travel from transmitter to receiver are often delayed. Hence a detailed knowledge of the water vapour fields is required to correct for such delays.

Water vapour - an important factor of the Earth's atmosphere is key for meteorology in terms of the spatial and temporal scales over a significant range. Atmospheric processes such cloud formation, convection, precipitation, storms and other climate systems can be identified with the knowledge of the water vapour field from the boundary layer of the atmosphere.

Rainfall and formation of clouds are closely related to distribution of water vapour. The atmospheric vertical stability and atmospheric storm initiation is largely affected by the distribution of the water vapour, this is due to the fact that high latent heat is related to the phase change of the water. It also affects how the dynamics of the evolution of the whole weather systems and hence plays a important role in stability of the atmosphere. It is also one of the significant contributors to the greenhouse effect than any other atmospheric parameters.

Timely warning of extreme weather related events can be achieved through accurate measurement of distribution of the water vapour content in the atmosphere, especially the data on the moisture from the boundary layer. Also the storm scale weather formation is directly relative to the moisture content in the boundary layer [1]. Furthermore, understanding the information on the scale of 2-5 km is required for forecasting in the boundary layer [2].

Even though, considered to be one of the important elements in the atmospheric weather forecasting, the measurement of moisture or water vapour is still very erroneous. Hence, the need for improving the accuracy and this can be achieved with the increased resolution of spatial and temporal variation of the water vapour content in the NWP model. Numerical weather model have improved enormously over the past few years in terms of spatial and temporal scale resolution..

The Met office NWP model UKV which has been recently developed for higher resolution runs with a grid spacing as small as 1 km as compared to the previous models which was being operated at 12 km. The advantage of running such a model is to provide improved and accurate warning of severe weather and also provides important information regarding the convection initiation and cloud formation.

1.2 Research Background

There are a variety of sensors to monitor and measure the variation of water vapour in the atmosphere. However, there are relatively very few instruments which measure distribution of moisture content in the atmosphere on the spatial and temporal scales, which is less than few hours and less than few hundreds of kilometer. With the development and efficient use of the new high resolution NWP model, the need to provide or obtain the data on the spatial and temporal scales is ever so important. The common techniques used to measure the water vapour distribution are through radiosondes, water vapour radiometer, water vapour from GPS and other satellite based methods. A new and efficient way to measure the moisture content of the atmosphere is from the use of broadcast (DAB/DVB-T) signals [1] [3].

When compared with the existing methods DAB/DVB-T water vapour measuring technique have the following advantages:

Low cost

Radiosonde is one of the most commonly used technique and very expensive. This limits the number of launches and hence data cannot be acquired consistently. Water vapour radiometer is another type of radiometer which is even more expensive than radiometer. GPS water vapour technique one of the recently developed technique to measure moisture content uses dual frequency receivers (each costs £10K-£15K) is much effective but also very expensive. DAB receivers are much cheaper in comparison to all of the above remote sensing measurement instruments.

High Spatial and Temporal Variation

Due to its extremely high cost of operation, radiosonde based method does not provide adequate water vapour information about the spatial and temporal resolution. Due to its cost efficiency to operate only a few times a day leads to gap/limitation in the water vapour dataset. This leads to the short term weather forecasting being limited and error prone. GPS water vapour technique is very expensive set-up to run, and requires a dense array of receiver to obtain high resolution information on the spatial scale. This is in the order of few kilometres(1-2 km) to obtain the data within the boundary layer [1]. Observations made through satellite methods do not have the capability to provide the fine scale information in the range of (1-4 km).

1.3 Research Objectives

To examine the feasibility of making measurements of refractivity by the reception and processing of digital radio broadcasting (DAB) and digital video broadcasting television (DVB-T) signals, which are more commonly known as Freeview TV signals)[1]. This research study will help estimate water vapour over large areas on a very small scale ranging between 1 km and 4 km and thereby contributing to the formation of a sensor network to make measurements at such small scales. This will therefore help towards the proper and full utilization of the high-resolution numerical weather models. The basic concept is similar to that of the

GPS water vapour technique. A radio signals travelling from the transmitter to receiver is affected by the presence of water vapour in the troposphere, which introduces an extra delay in the signal propagation in addition to the normal propagation path. The velocity of propagating radio signals decreases as a result of an increase in refractive index, which is due to the presence of water vapour. The changes in the signal path delay can be estimated through the measurement of the signal phase and can be linked to the water vapour from the transmitter to receiver. There are however many challenges in achieving this:

This project will answer the following key questions:

- 1) What is the feasibility of using a network of sensors receiving broadcast terrestrial radio signal to measure path- integrated water vapour?
- 2) What is the likely accuracy of the delay estimates and under what circumstances and locations can these be expected?
- 3) Is it possible to estimate water vapour refractivity from tomography reconstruction technique by using a network of path link delays?

1.4 Structure of the Thesis

This thesis is divided into seven chapters.

In Chapter 2, we present the background theory into the tropospheric layer and its effects on the radio wave signal propagation through that layer. Initially, we begin with the details about the structure of the atmosphere and then the refractivity and its importance. The major focus of this chapter is looking into tropospheric delay and its effects on the signal. A detailed explanation is given about the types and significance of the delay in the troposphere. This chapter also introduces the reader to a review of the different remote sensing measurement techniques used for measuring atmospheric refractivity.

Chapter 3 introduces the reader to the opportunistic signals namely DAB & DVB broadcast signals for atmospheric remote sensing. This chapter gives details about the use of the broadcast signals to measure atmospheric refractivity. The DAB network and the signal availability in the UK is also shown. The methodology and the set-up to use the DAB/DVB as a remote sensing measurement tool is also further explained in this chapter. This chapter also details the

various phase delay retrieval algorithm.

In Chapter 4 we look introduce the Ray tracing technique. The main emphasis in this chapter is to estimate the signal propagation path delay. At first we give background theory and the types of ray tracing methods. We then also implement the ray tracing algorithm to estimate the delay due to the atmospheric refractivity/water vapour. This chapter also covers the refractivity formulation from atmospheric constituents and delay estimation.

In Chapter 5 we perform the analysis of the path delay obtained from the ray tracing. We start this chapter by showing the ray tracing signal propagation under different condition, ray angles and some other parameters. We also perform a statistical analysis of the ray traced delay. This chapter shows results and analysis of the delay variation based on the season, distance and the time of the day along with year is shown.

Chapter 6 introduces the solution of using tomography inversion technique to extract the atmospheric refractivity/water vapour from the ray traced delays. A broad introduction to tomographic approach is given. Here the analysis attempts to use a network of links and the ray tracing algorithm to extract the refractivity. This chapter shows the methodology of the inversion process along with the inversion reconstruction algorithm.

Chapter 7, this chapter concludes and summarizes the results. The Chapter 7 further presents the future research work.

CHAPTER 2

BACKGROUND/LITERATURE REVIEW

This chapter introduces you to background theory of troposphere delay contributions and the overview of various research methods to measure atmospheric water vapour. The chapter is organized as follows; In section 2.1, we give a brief summary about the structure of the atmosphere and then move into the details about the troposphere effects on the radio signals. In section 2.2, a description on how the characteristics of a signal propagation is affected by the environment and the steps to obtain delay. Further, we show the formulation of refractive index and refractivity from the atmospheric constituents/parameters. Section 2.3 we describe about the various delay terminologies. In the subsections, we define delay, where we show the different types of path lengths and understand the differences between the normal signal path in the atmospheric medium and the signal path with free atmosphere. In section 2.3.4, an explanation about how to obtain the delay from the path length is shown.

The main aim of this research is to understand how water vapour affects signal propagation through the atmosphere. Hence, we discuss the advantages and disadvantages of the existing atmospheric data measurement techniques. In section 2.5, we study the different existing water vapour measuring techniques.

Finally, the important part which is the focus of this research is delay modelling, and in Section 2.6 we go in to understanding the importance of delay modelling and the stages involved in the process of delay modelling. We conclude this chapter by giving a brief summary of the overall chapter, its scope and also an

introduction to the next chapter.

2.1 Tropospheric Refraction

2.1.1 Structure of the Atmosphere

Atmosphere consists of several layers. Figure 2.1 below shows the various layers of atmosphere. *Troposphere* - a layer of atmosphere, closest to the surface of the earth extends to a height of 12 km above the Earth's surface. Next to the Troposphere is the Tropopause layer, which is approximately 8 km between the troposphere and the next layer Stratosphere and exhibits the properties of both the troposphere and the stratosphere. From a height of about 16-70 Km from the surface of the earth exists a layer called *Stratosphere*. Troposphere, Tropopause

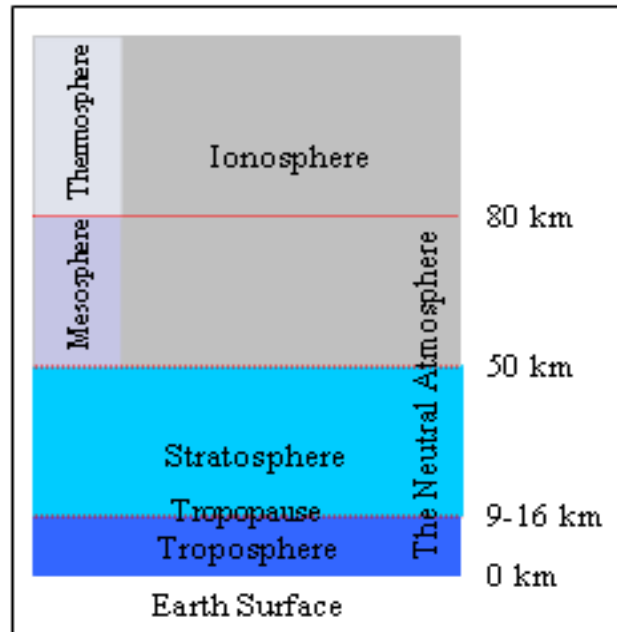


Figure 2-1: Structure of the Earth's atmosphere layers shown including the region of neutral atmosphere[70]

and Stratosphere are electrically neutral region, hence these layers are termed as neutral atmosphere. Above the Stratosphere is the region of atmosphere which consists of charged particles and molecules, called the *Ionosphere* / *Mesosphere* and extends from a range of about 70 to 1000 km from the surface. The radio signals travelling through these atmosphere are significantly affected by the delay

in time due to all of these atmospheric regions [55].

From the atmospheric layers shown above in the figure, one of the important region that this study is focussed on is the region of troposphere. “*Troposphere* is the region of atmosphere and one of the neutral atmosphere, where the molecules and the elements are in the neutral state”[55]. One of the factors influencing the signals travelling in the troposphere region is the effects of the water vapour refractivity. The major atmospheric events such as formation of the clouds, rain-fall, thunderstorm and snowstorm occur due to the presence of the water vapour with high variability [55].

2.2 Refractive Index to Refractivity

Estimating the time taken for a signal to travel from the transmitter to receiver on ground is an important observable in meteorology. The signals propagate at the speed of light in vacuum, which is approximately equal to $3 \times 10^8 \text{ ms}^{-1}$. The electromagnetic signals that travel through the neutral atmosphere(troposphere) are often delayed due to the presence of charged particle in the atmosphere.

Hence for a medium, the ratio of the velocity of an electromagnetic wave/signal in a vacuum to the speed of propagation in the medium is known as the refractive index (n) defined as:

$$n = \frac{c}{v} \quad (2.1)$$

Where ‘ c ’ is the speed of light in the vacuum and ‘ v ’ is the phase velocity in the medium.

For convenience, refractive index is mathematically easier to use in terms of refractivity (N), this is because ‘ n ’ does not vary by more than a few parts of a thousand from unity and ($n-1$) is small. Therefore, the refractivity (N unit) is defined as:

$$N = (n - 1) \times 10^6 \quad (2.2)$$

For the Earth’s neutral atmosphere, the total refractivity (N) of the atmosphere was formulated by [29] as,

$$N = K_1 \frac{P_d}{T} + K_2 \frac{P_w}{T} + K_3 \frac{P_w}{T} \quad (2.3)$$

Where k_1, k_2, k_3 represent the coefficients determined empirically. The term ' P_d ' and ' P_w ' are the partial pressures due to dry gases and Temperature(Kelvin) in the atmosphere.

Total refractivity in Equation 2.2 can be further separated into two components: a hydrostatic (dry) refractivity and non-hydrostatic refractivity (wet) [5][6].

$$N = N_d + N_w \quad (2.4)$$

The first term hydrostatic/dry refractivity is defined as:

$$N_d = K_1 \frac{P_d}{T} \quad (2.5)$$

The second term in the Equation 2.4,

$$N_w = K'_2 \frac{P_w}{T} + K_3 \frac{P_w}{T} \quad (2.6)$$

is the wet refractivity, where

$$K'_2 = K_2 - K_1 \frac{R_d}{R_w} \quad (2.7)$$

' P_d ' and ' P_w ' are the partial pressure of dry gases and partial pressure of water vapour in units of hecto Pascal (hPa), ' R_d ' and ' R_w ' denote the gas constant for dry air and water vapour, respectively and ' T ' is the temperature in units of Kelvin(K).

There have been several discussions and research that have been done to determine the refractivity coefficients k_1, k_2, k_3 . The coefficients determined by [7] was considered the "best average", which is $k_1 = 77.6890(\text{k/hPa})$, $k_2 = 71.2952(\text{K/hPa})$ and $k_3 = 3.75463(\text{K/hPa})$.

Hence, the general refractivity in terms of N unit can be written as,

$$N = 77.6 \frac{P}{T} + 3.73 \times 10^5 \frac{e}{T^2} (N \text{ units}) \quad (2.8)$$

Where ' P ' is the atmospheric pressure in [mb], ' T ' is the temperature in [K] and ' e ' is the partial pressure of water vapour in [mb].

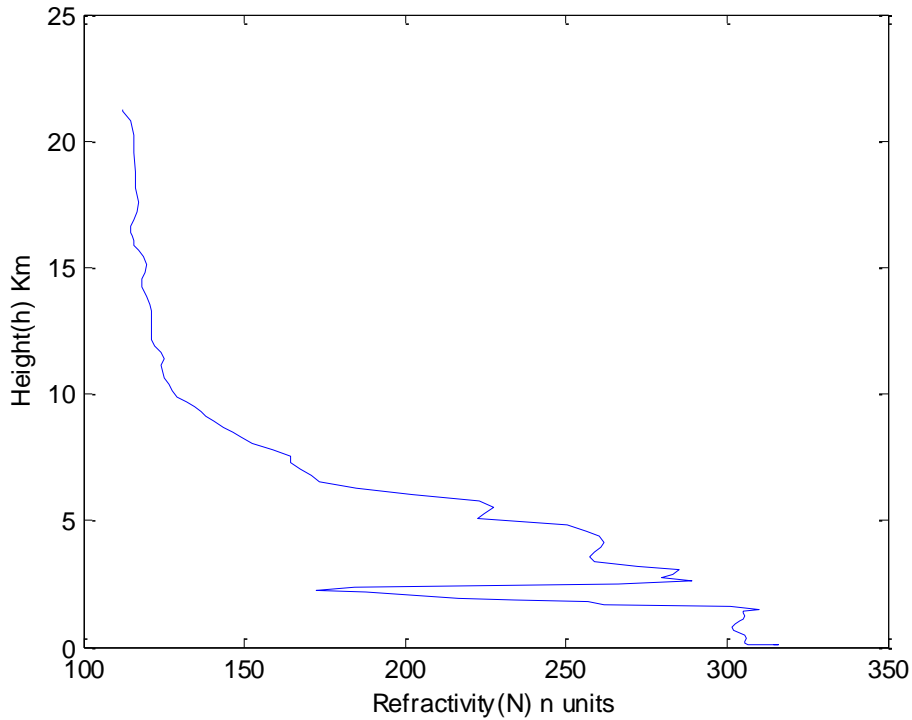


Figure 2-2: A typical vertical profile showing the variation of refractivity against height obtained from the Radiosonde datasets.

2.3 Classification of Types of Delay

2.3.1 Atmospheric Propagation Delay

One of the important factors affecting radio signal propagation time as the signals propagate through the atmosphere from the transmitter to receiver is the refractive index. The details about the refractivity medium and its effects can be found in the section 2.2. The refractive index variation is higher near the atmospheric layers closer to the surface of the Earth[6] and decreases as we move up the layers of atmosphere. This largely affects the propagation velocity of the signals passing through these layers by decreasing the propagation velocity. High variability in refractivity leads to signals propagating through these medium, no longer travel in a straight line propagation path, which is known as bending or ray bending. The ray bending is explained in section 2.3.2. The different propagation path can also be seen from Figure 2-3.

The bending of radio signals due to variability of refractive index in presence of atmospheric medium leads to the radio signals taking longer propagation time than the signal propagating through the medium with no atmosphere. The difference between the two propagation path which is signal propagation with and without the presence of the refractive index medium is more commonly described by the term “Delay”. In the next section we will discuss some common delay terminologies and types used to describe delay mathematically.

2.3.2 Types of Path Length (Actual Path Length Vs Geometric Path)

The path length is technically expressed in terms of integrals along the ray propagation path [6][34]. The integral along the path is further dependent on different component, the differential element, denoted as ds along the ray path, path distance ‘ L ’, and the medium from transmitter to the receiver.

The terms differential element ‘ ds ’, path distance ‘ L ’ and the refractive index(atmospheric medium) defines the “actual path length” also known as “optical path length” can be expressed in integral form as shown below:

$$L = \int_{Tx}^{Rx} n(s)ds \quad (2.9)$$

Where, ‘ n ’ is the refractive index. The introduction of atmospheric medium in this case introduces the bending of the signal propagation from transmitter to the receiver. As the ray signal propagates through these atmospheric refractivity medium the propagation velocity is affected. The decrease in the propagation velocity influences the directions the signal propagates and thereby ending with a bent ray path [6][34].

Another type of path length would be the geometric path length or more commonly referred to as “straight line path”. Here the propagation path is equivalent to travelling in a vacuum which is equivalent to travelling at the speed of light. All the elements from the definition of the actual path length except without the inclusion of atmospheric medium variation along the path integral define the “geometric path length” and can be expressed as:

$$L = \int_{Tx}^{Rx} ds \text{ or } L = \int_{Vac} ds \quad (2.10)$$

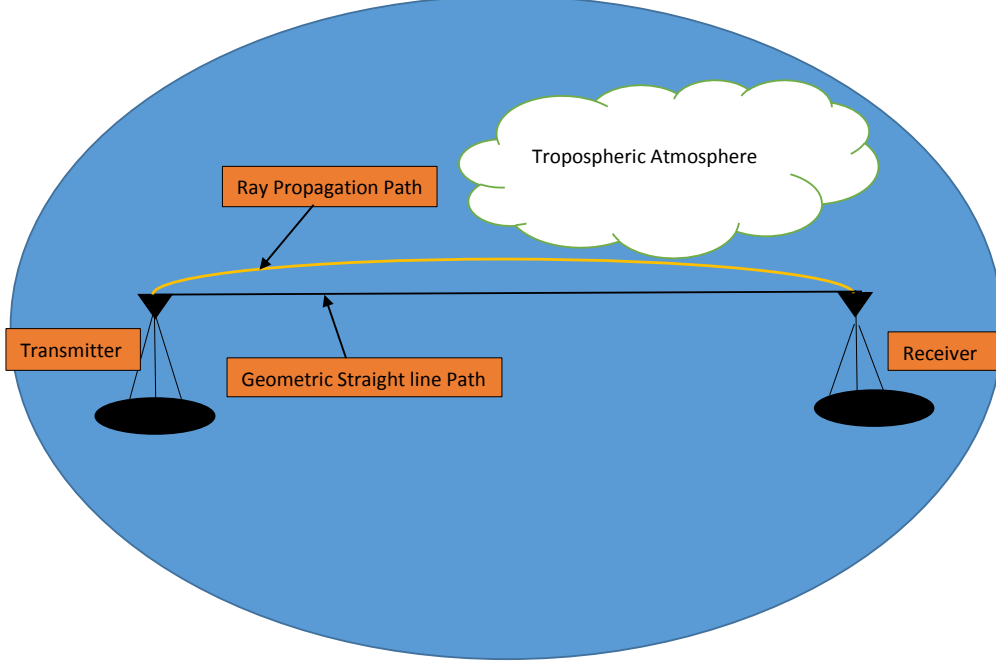


Figure 2-3: Typical ray propagation environment showing the comparison between the straight line propagation path and the bent path from the transmitter to receiver

Figure 2-3 is a typical example showing the difference between the normal propagation path in the presence of atmospheric medium and the geometric straight line path.

2.3.3 Path Length to Delays(Signal Delay)

From the different types of path length described in section 2.3.2 namely the actual path length and the geometric path length now further contributes to understanding and defining atmospheric delay. Atmospheric Signal delay (ΔS) also known as “excess path length”, can be defined as the difference between the propagation path length through the atmosphere and the actual geometric path length. The excess path length is given by the path integral between the transmitter and the receiver [12] [13].

$$\Delta S = \int_{Tx}^{Rx} n(s)ds - \int_{Tx}^{Rx} ds = \int_s (n - 1)ds \quad (2.11)$$

where ‘ $n(s)$ ’ is the refractive index as a function of position ‘ s ’, and the first integral is the propagation path with varying refractive index and the second one is the straight line path length between the transmitter and receiver[54]. The Equation 2.8 is simplified in terms of refractivity and can be expressed as,

$$\Delta S = 10^{-6} \int_{Tx}^{Rx} N(s) ds \quad (2.12)$$

Where, ‘ $N(s)$ ’ is the refractivity of the medium along the propagation path.

2.4 Troposphere Delay

The troposphere consists of a mixture of different gases. The refractivity index of the tropospheric layer is thus the sum of the contribution of each constituent gases that composes the troposphere multiplied by its own density [8] [9]. The delay caused by the troposphere’s refractive index can be categorized into two delay components, “dry delay” (or hydrostatic) component and the “wet delay” (or non-hydrostatic) component, with the latter containing only the water vapour contribution:

$$N_{troposphere} = N_{dry} + N_{wet} \quad (2.13)$$

The dry and wet delay are expressed as follows,

$$N_{dry} = 77.64 \frac{P}{T} \quad (2.14)$$

$$N_{wet} = 3.73 \times 10^5 \frac{e}{T^2} \quad (2.15)$$

Where ‘ P ’ is the atmospheric pressure in [mb], ‘ T ’ is the temperature in [K] and ‘ e ’ is the partial pressure of water vapour in [mb]. The dry delay component is the main error factor, accounting for 90% of the entire tropospheric delay [10]. The hydrostatic delay is caused by dry gases in the troposphere and the non-dipole component of water refractivity while the wet delay is caused solely by the dipole component of water refractivity, which we refer to as water vapour [11]. Despite its great influence, the dry component is easily modelled since the behaviour of gases composing the atmosphere is uniform. Using the laws of physics, the behaviour of atmospheric gases can be defined into an equation for calculating the delay caused by dry component.

Wet delay is roughly 10% of the total delay and is difficult to predict and model because it depends on the water vapour content, clouds, and rain present in the troposphere along the signal propagation path [65]. The wet component, although accounting for only 10% of the entire delay, is the problematic one. The wet component, the humidity percentage, cannot be modelled and its atmospheric spread is not uniform as the many factors influence it, such as vicinity to water, temperature, air pressure, altitude and so on [65]. The wet tropospheric path delay depends on the water vapour distribution and changes much faster in both space and time. Further, this delay is dependent on the atmospheric pressure and can be estimated by utilizing the surface pressure on Earth[9].

2.5 History of Water Vapour(refractivity) Measurement Techniques of the Atmosphere

2.5.1 Radiosonde

A Radiosonde is a device wherein, the sensors are hung off a balloon and are released into the atmosphere to measure tropospheric/atmospheric parameters such as temperature, humidity, and pressure and is sent to the ground via a radio communication link. Also known as “Dropsondes”, where the sensors are dropped off an aircraft and are received through a parachute. It is the base for prediction system and analysis for almost all the meteorological centres worldwide.

The data sources obtained from Radiosonde can be called the actual/real observations, as it is very close to reality[14]. Measurement of Water vapour through Radiosonde has many advantages. Data obtained has proved to be very reliable and accurate based over the years. Real values of atmospheric parameters such as pressure and temperature is obtained hence not much data processing is required.

Even with all the advantages in providing large vertical resolution, the Radiosonde measurements do still have several disadvantages. One of the main drawbacks is the non re-usability of the kit, as it can be used only once. Hence it's very expensive, cost ineffective thereby limiting the number of balloons that can be launched to only twice daily [12][15]. Radiosonde measurements are mostly inadequate during sudden or speedily changing weather because of the amount of

time it takes to reach the lower layer of the troposphere and therefore providing less data on a very large time scale [15]

Data obtained are only for the zone in which the Radiosonde is released, and not for the neighbouring locations around the area. Hence it calls for the need of horizontal interpolation for areas other than the release locations [16]. Radiosonde measurements inefficiently/inaccurately solve the variation of temporal and spatial water vapour, because the variation of temperature or pressure occurs at much larger scales than the water vapour measurement (which occurs at very fine spatial and temporal scales). This lack of accuracy in the analysis of water vapour are the foremost cause of error in forecasting rapidly changing weather and short term weather forecasting(less than 24 hours).

2.5.2 Water Vapour Radiometer

Space borne or Land based water vapour radiometer (WVR) are instruments that can determine the integrated water vapour content by measuring the background microwave radiation/temperature produced by atmospheric water vapour along the given line of sight [12][17][18][20]. There are two types of radiometers namely, land based and satellite based radiometers.

Ground based WVR (Upward looking)- Water vapour emission measurements against the cold background of deep space between the ground and space bore sight. The Space WVR are installed on satellite and point downwards to the ground. The space based WVR (downward looking) estimate the atmospheric conditions by the absorption lines (background temperature) against the Earth's hot surface between the satellite and earth. Compared to radiosondes, WVR do not have the package or instrument travel time to measure atmospheric conditions. And also has been proven to be a reliable method over many years now as is the case with radiosondes for accurate measurement.

One of the major drawbacks of WVR as compared to the Radiosonde is the equipment cost which is around \$300000. Therefore, using array of VWR for measuring data is not feasible and cost-ineffective [15]. Hence measurement of spatial resolution of atmospheric data is limited for accurate modelling with lesser WVR in use [19].

Another important distinctive limitation is that the VWR cannot be used under severe rain and extreme overcast conditions [12] [17] [20]. As the temperature can vary considerably based on the surface the radio wave hits, the space based WVR are limited in retrieval of accurate water vapour measurements. And also the variation of temperature in the hot background is hard to determine. For example, even the formation of clouds can cause change in the background temperature from surface of the earth ≈ 290 K to clouds ≈ 220 K [12].

Even the Upward looking VWR are affected during the heavy cloud formation but are not affected by moderate light cloud cover. Both the VWR are more or less complementing each other rather than opposing systems. Hence Satellite Based VWR are usually used over large water surfaces like oceans where the temperature tend to be more or less the same across the surface [12] [15] [19] [21].

2.5.3 Microwave Radiometer

A device designed to measure the thermal emission from the regions of interest is known as Microwave Radiometers. MWR are very sensitive receiver which measures the atmospheric radiation due to black-body emission and also measuring the absorption along its path from the receiver to the atmospheric region of interest.

The microwave radiometer is used to determine the atmospheric water vapour and thereby the cloud convection and rain by operating at specific frequencies. The sky brightness obtained at these frequencies is converted into the water vapour.

Radiometer, even though they provide high spatial resolution, they are very expensive than most of the other remote sensing instruments. The main disadvantage is lower resolution and accuracy than in-situ instruments [22]. One of the significant advantages of the microwave radiometer (MWR) over the other radiometers is its ability to operate and measure under all weather conditions. The measured data are of high temporal resolution and hence can be used as meteorological parameter [23].

The vertical resolution of the MWR is low $\approx (500 \text{ to } 1 \text{ km})$ as compared to the Radiosonde $\approx (0.01 \text{ to } 0.5 \text{ km})$. But on the other hand they do provide a very high temporal resolutions in comparison with the radiosondes or any other remote sensing instruments which is of the order of few minutes.

2.5.4 Water Vapour From GPS

The GPS (Global Positioning System) is a system designed originally to determine one's position relative to the Earth. Since its invention GPS has been used in a wide range of applications, particularly in the field of space geodesy or more commonly called as "GPS Meteorology". The GPS system consists of numerous network of satellites, and this network is used to determine the atmospheric water vapour. This system was based on the delay of the propagation of the radio waves through the atmosphere. Since the water vapour is the only significant variable constituent, it contributes to delay in the radio waves.

In the UK, the Met Office operates a network of 120 GPS dual frequency receiver to derive the water vapour [1]. Typically, each of these dual frequency receivers cost approximately \$15K. For a network of 24 stations, the cost of the entire network of systems would be around \$400K [12] to estimate the water vapour. However, the data obtained is good enough but there is lack of higher spatial and temporal resolution data which is in the range of very few kilometres in the boundary layer. This is because to obtain the data from the boundary layer, there is a need for a large array of GPS receivers, and that would be very expensive.

Table 2.1 shows the differences between different water vapour refractivity measurement equipments in terms of horizontal, vertical resolution and temporal resolution. Also shown in table is how the variation in costs is directly proportional to temporal and spatial scale resolution. For sensors with fine resolution both on the horizontal and vertical scales such as radiometers, the cost of the equipment is relatively very high. In comparison to sensors with low cost such as radiosonde, the horizontal and vertical resolution is very high. Hence, an alternative to existing water vapour measurement techniques is needed. Here we introduce the feasibility study of using DAB/DVB to measure atmospheric refractivity. The scope of this research is very much into the path delay analysis

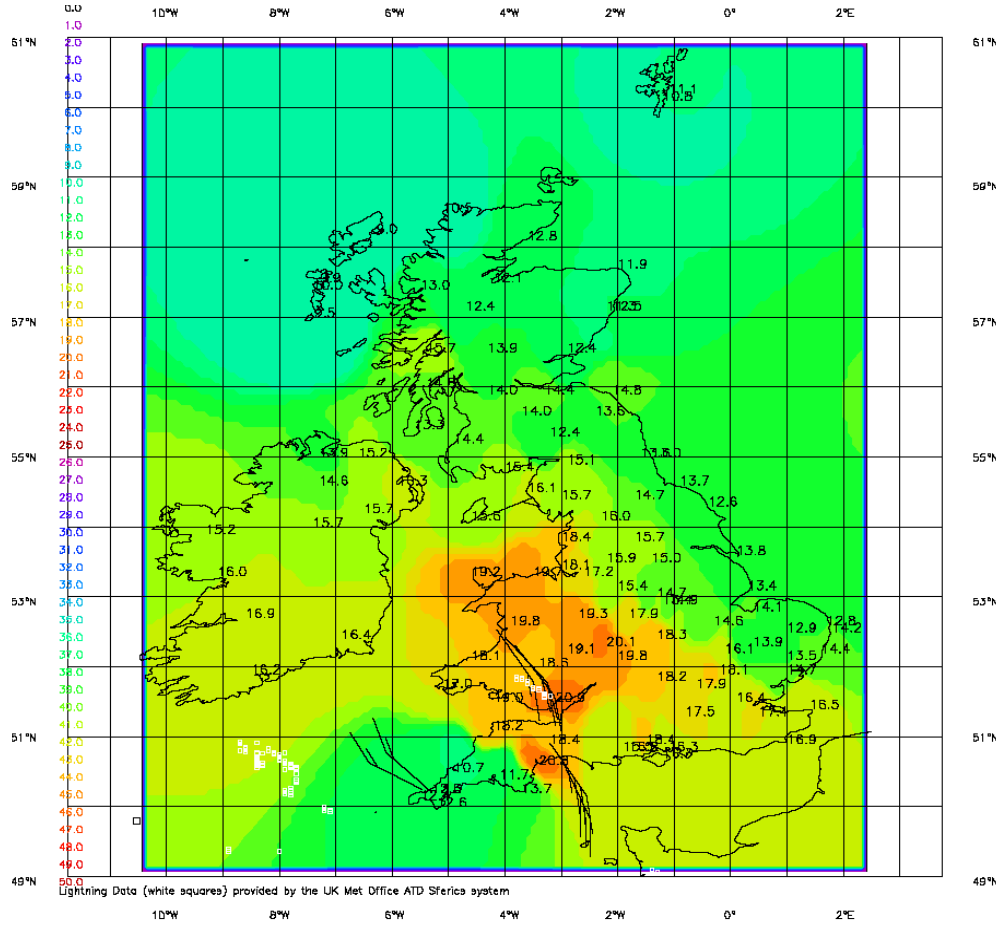


Figure 2-4: Typical example of a water vapour derived from UK GPS network(Source: Met office UK).

of the signals propagation through the atmospheric medium. The overall aim was to understand whether DAB/DVB data can be used for atmospheric remote sensing and to estimate the signal delay from the DAB/DVB data, hence we have included this in the research. We discuss the use of DAB/DVB and the methodology used in detail in Chapter 3.

2.6 Significance of Tropospheric Modelling

The objective here is to understand and estimate radio signal delays as they propagate through troposphere from transmitter to the receiver. Over the years different methods of prediction and estimations have been proposed to understand and study the neutral atmospheric delay(troposphere) from the data obtained using the different measuring techniques as detailed in section 2.3.

Sensor	Horizontal resolution (km)	Vertical resolution (Km)	Temporal resolution	Cost
Radiosondes	≈100 (National Weather Services USA)	0.01 – 0.5	12 hr (Operational)	Low-cost (but large numbers required)
Dual-frequency GPS	≈50	0.5 – 1 (Expected)	30 min	Medium
Profiling microwave radiometers	0.5 - 1	0.5 – 1	10 – 15 min	High
DAB/DVB-T	≈1	≈5	1-20 min	Cheap?

Table 2.1: *Comparison of horizontal and vertical temporal resolution of various remote sensing instruments.*

This process is generally achieved either by prediction modelling. So, how is modelling different from prediction; for example, when you obtain the delay observables directly from the measuring equipment then that process is termed as estimation. On the contrary, when the delay is calculated by modelling using the atmospheric constituents such as pressure ‘P’, temperature ‘T’ and relative humidity ‘RH’, here this process is defined as modelling or prediction. The dependence of variability in delay on various parameters of atmospheric constituents and its dependence on the speed of the propagation of the signals make it furthermore difficult to predict and estimate delay.

Figure 2-5, shows the different steps involved in modelling of the atmosphere delay. The general methodology for the modelling of troposphere delay can be defined as finding the delay between the transmitter and receiver under a certain model of atmosphere. The atmospheric model in this case would depict the

environment of the troposphere which would be modelled using the measured atmospheric data parameters. Another key element in modelling would be the calculation of refractivity from the data parameters such as pressure, temperature and relative humidity.

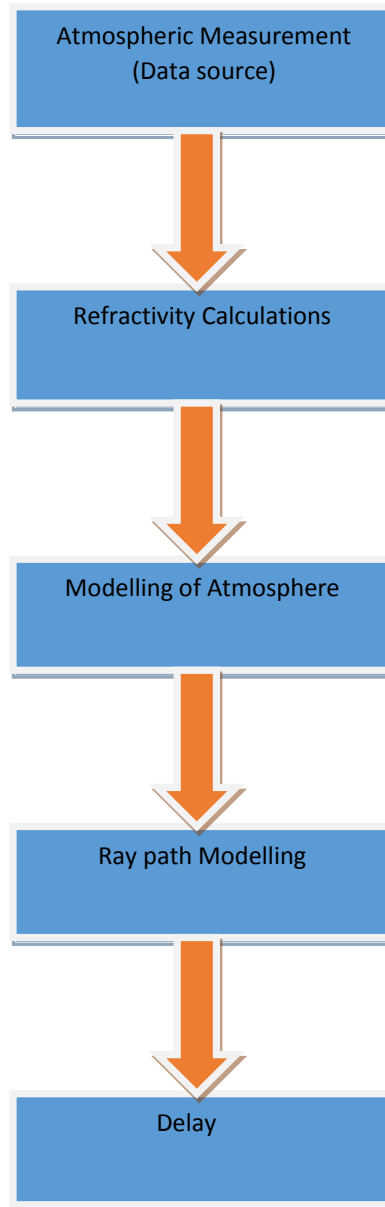


Figure 2-5: *The chart shown above gives different stages of modelling of atmospheric delay*

The methodology of calculation and formation of the model from atmospheric parameters to refractive index and finally to refractivity is explained in section 2.2. We will further discuss with more depth and detail about refractivity calcu-

lation in Chapter 4. And finally the most important part of the delay formulation is the modelling of ray path and its variations along the path from transmitter to the receiver positions. In Chapter 4, we will present a range of options available for modelling of ray propagation path.

2.7 Summary

The focus of this chapter was to understand the background and the terminologies required for modelling the troposphere delay. The formulation of delay was shown which can be calculated using data from various remote sensing instruments. We also introduced you about the different delay terms. We distinguished between different atmosphere data measurement techniques. We then discussed the need for modelling the delay and why it is important to model delay and the impracticality of directly obtaining the delay from atmospheric data parameters. Finally, we introduce you to the different stages involved in modelling the delay, some of these stages will be explained in detail in Chapter 4 of ray tracing.

2.8 Overview of the following Chapters

To overcome the drawbacks of the existing data measurement techniques and their limitations, we will introduce you to a feasibility study of using a different and cheaper atmospheric data measurement technique. The study is based on using the DAB/DVB data as an alternative to existing measurement techniques. In Chapter 3, we discuss about the methodology and techniques used to measure atmospheric data using DAB/DVB. Chapter 4, introduces the theory and background of ray tracing and then go on to show the ray tracing process for modelling the ray path in a modelled atmospheric environment.

CHAPTER 3

SIGNALS OF OPPORTUNITY

In Chapter 2, we discussed about the various existing remote sensing methodologies along with the advantages and disadvantages. We also discussed about the measurement principle used to calculate the delay from atmospheric constituents. In this chapter, we will introduce the feasibility study of using DAB/DVB as remote sensing instrument, which can be used as a source of measuring atmospheric constituents to estimate atmospheric refractivity.

In section 3.1, firstly we look into the overview and introduction of the DAB and DVB broadcast signals. In section 3.2, we discuss the important features of using the Digital Audio Broadcasting(DAB) and Digital Video Broadcasting(DVB) signals along with its advantages and disadvantages. In section 3.3, we look into the DAB/DVB signal availability in UK. In the later sections, we will then look into the experimental set-up and different methodology currently used along with the advantages and disadvantages to measure the propagation phase delay. Finally, we show some results obtained through the use of different retrieval algorithms to demonstrate the possibility of estimating the phase delay [1].

3.1 Introduction to Broadcast Signals

Digital broadcasting systems such as DAB and DVB-T are high power systems, which may also provide an opportunity for atmospheric remote sensing. Since the invention of the broadcasting signals, broadcasting signals have grown signif-

icantly over the years.

The feasibility of using the broadcast signals to monitor the atmospheric variations was first suggested by C.J. Coleman [3] and later by R.J. Watson [1]. An important feature of DAB/DVB is its excellent phase tracking and good auto correlation properties when compared to other radio signals[1]. Another significant benefit of using the DAB/DVB is the already existing network with a coverage about 95% in UK.

As the signals propagate in the atmosphere they are affected by the environment in which they are travelling due to various atmospheric factors. Signal phase and strength of the signals will vary if there is variation over time. Similarly, broadcast(DAB/DVB-T) signals are affected due to the variation in atmospheric characteristics such as temperature, pressure and refractivity, which in turn results in changes to the refractive index.

This change in refractive index induces a phase delay which is an addition path distance. The refractive index of the signal can be measured using the data obtained from the variations of atmospheric characteristics like temperature, pressure and humidity. The atmospheric parameter which is of importance in this study is the humidity, where maximum variation occurs.

Ideally, the aim here is to measure the refractivity of signal over the path length by building a network of sensors in close proximity to receive DAB and DVB-T broadcast signals. Then phase comparison is made between the transmission of signal affected by refractivity and the signals from direct line of sight. The advantage of this system over the previous measurement techniques are: low-cost/economical and easy to run and process as compared to previous techniques. Data obtained can be assimilated into the NWP and can be used for many other applications.

3.2 Features of DAB and DVB Network

The deployment of the digital system for broadcasting (DAB & DVB) over the years has given the opportunity to many new types of broadcasting applications. One such application is using broadcast signals such as DAB and DVB-T for

environmental remote sensing. The digital radio was first introduced and rolled out in United Kingdom in 1995 by BBC.

But transmission test goes back way into the early 1990's conducted by BBC. Currently UK has around 95% coverage for broadcast signal reception and consists of a wide range of network for both DAB and DVB-T. Hence the digital television signals can be received from almost all over UK when the digital switch-over is totally completed.

UK digital transmitter network is the largest radio network in the world. It comprises of 148 DAB transmitters and 87 DVB-T transmitters [25], broadcasting over 250 commercial and BBC radio stations across the UK. Further, another set of 137 DAB transmitter are run by Digital One for other applications such as classic FM.

DAB/DVB-T operation is the first standard based on orthogonal frequency division multiplexing 'OFDM', which is capable of successfully operating in the fading or multipath environment for wide band digital communication systems [24].

The concept of Single Frequency Network(SFN) is one of the most important elements of the digital broadcasting system standards. A SFN is a network in which a number of transmitters simultaneously send the signal over the same frequency channel. One of the more common examples is the DAB, where for each multiplex only one frequency is used. The advantages of using such a network are high frequency and lower power operation. One of the drawbacks of the SFN network is that it requires proper synchronization.

Figure 3-1 shown gives an example of the working of SFN network. Here the transmitters with (-) are closer to the receivers and the transmitters with (—) are far away from the receiver which consists of interfering signals [39].

The main advantages of the SFN approach are high frequency efficiency, low-power operation, internal network gain, high location probability, easy gap-filling (frequency re-use)[59].

The disadvantages are network splitting is not possible, synchronization is necessary, feed control is required[59].

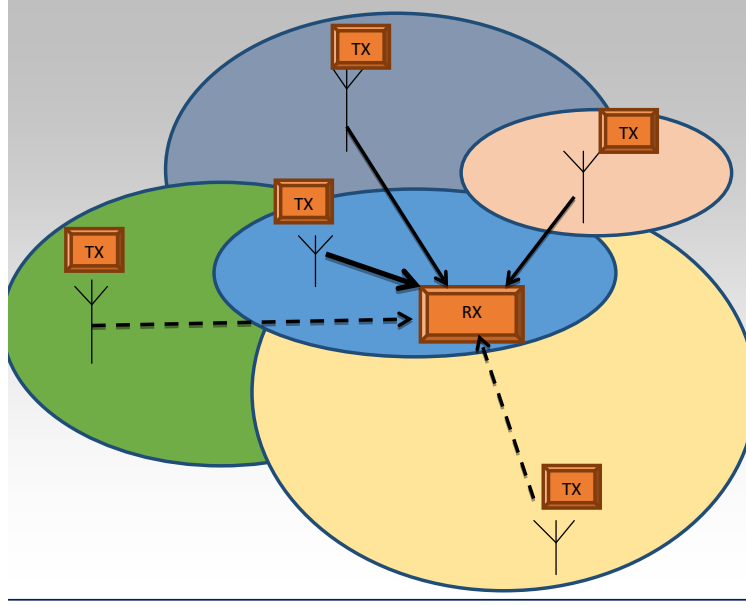


Figure 3-1: *Illustration of an SFN network. Here the transmitters with (—) are closer to the receivers and the transmitters with (---) are the one far away from the receiver and these are the ones with interfering signals [39].*

3.3 DAB/DVB Signal Availability in UK

The Figure 3-2 shown below is the map showing the DAB/DVB transmitter availability in and around the region of Bath and Bristol. The red circles indicate the locations of transmitters responsible for the strongest receivable signals at the University of Bath campus. These transmitters are usually a mix of small local transmitters and main transmission towers. The strongest transmitters are Mendip, Bathampton(near Bath), and Wenvoe in Wales. UK region has a good coverage of DAB and DVB availability.

3.4 Experimental Set-up

The methodology used to calculate the delay between a pair of transmitter and receiver is similar to that used in the current GPS refractivity measurement system. The methodology works on estimating the changes in the propagation velocity between a transmitter and the receiver which in turn dependent on the changes in the pressure, temperature and the relative humidity. It is based on the principle given by the Equation [2.1] as,



Figure 3-2: Map from ordinance survey showing location of DAB transmitters in and around the city of Bath.

$v = c/n$, where, ‘ v ’ = phase velocity, ‘ c ’ = speed of light in a vacuum and ‘ n ’ is the refractive index. The propagation velocity is affected by the changes in water vapour density leading the occurrence of delay.

The first preliminary atmospheric refractivity work at Bath was conducted using equipment designed for DAB passive radar [3]. Figure 3-3 is shown demonstrating the experimental set-up used for the data-processing and collection using the DAB signals. The experimental test set-up consisted of a log periodic antenna, an anti-aliasing band pass filter and a 105 M-samples per second 14 bit ADC and digital receiver (GE/ICS-554). The DAB signal obtained was first sub-sampled, digitally down converted and then streamed to disk.

An ADC sample clock (low-jitter) was produced by phase-locking a low phase-noise generator (Rhode & Schwartz SMIQ03C) to the rubidium oscillator (Stanford Research PRS10). The estimated phase changes obtained were of the order of those expected from changes in water vapour. Time averaging and the other parameters of the phase locked loop were determined empirically in this analysis.

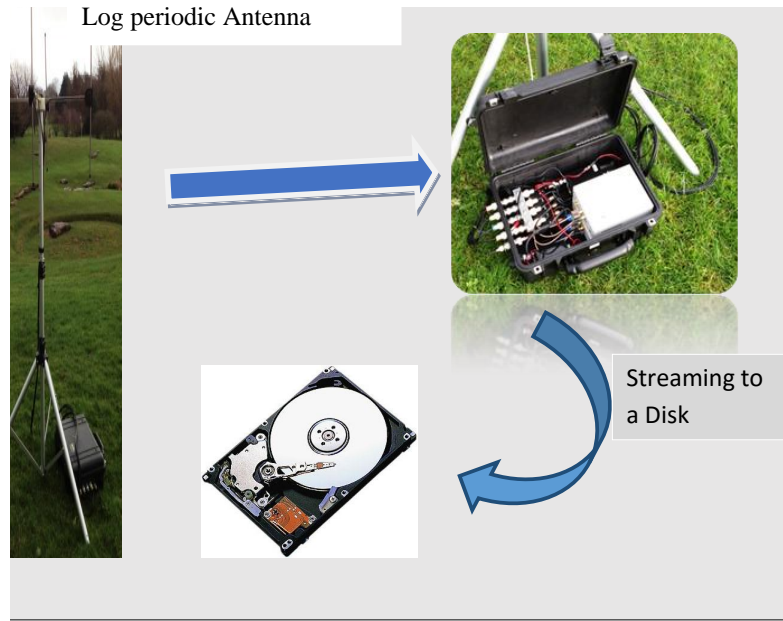


Figure 3-3: *Illustration of the experimental set-up for sampling and processing of DAB signal.*

3.5 Methodology and Algorithms Used to Retrieve Refractivity

The estimation of propagation phase delay was done using three different algorithm namely, Single-site autocorrelation, Synchronisation/Pilot symbol tracking and Multiple-site cross correlation. In the following subsection we will go into detail about each of the methods mentioned above.

3.5.1 Single Site Autocorrelation/Multiple Site Cross-correlation

In Single difference method change in phase along the path with time can be determined assuming that the phase of the transmitter is sufficiently stable. Double differencing technique is used for the case when the phase of the transmitter is inadequately/insufficiently stable. The difference in this method is obtained between a pair of transmission paths. The path determination is based on the unique difference in distance. The major advantage of using this method is the simple computation to track the phase with simple low powered platform.

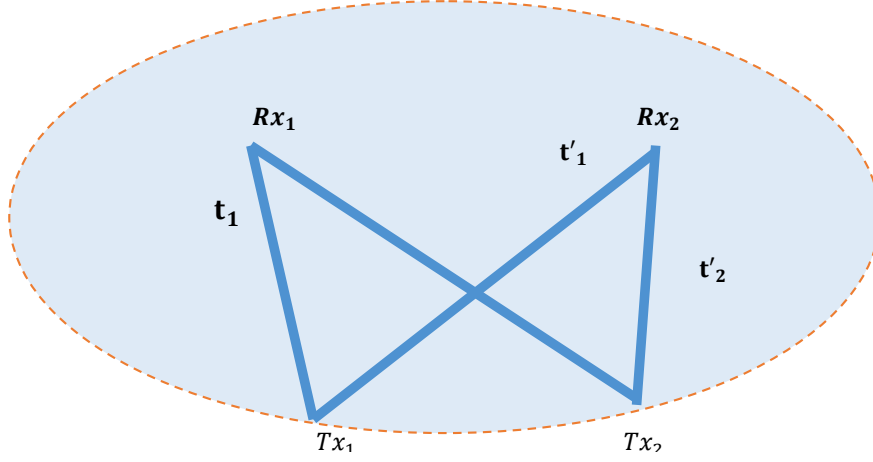


Figure 3-4: A typical example showing the illustration of multi-site correlation wherein there are more than one transmitter (Tx_1 and Tx_2) lying on the foci of the ellipse, and a pair of receivers (Rx_1 and Rx_2) to receive the signals from the transmitters.

Multi-site cross-correlation Double difference is a technique, where, the change in phase with time along the path is determined between two receiver sites. The transmitter phase error is eliminated in this methodology. Also, since DAB & DVB-T work on a single frequency network (SFN), where all the transmitters transmit identical data at the same time. This SFN feature means signals from different transmitters at different distances can be separated in the time domain. At any time, there should be only one transmitter on ellipse foci which is formed by any pair of receivers to uniquely find paths. Hence, it requires only one transmitter lies on the ellipse foci, this is explained using Figure 3-4 and the Equations (3.1) and (3.2) shown below illustrating the concept and reasoning behind why only one transmitter should lie on the foci of an ellipse.

For example, from Figure 3-4, At Rx_1 we have,

$$t_1 + t_2 = \text{const1} \quad (3.1)$$

Similarly, at Rx_2 we have,

$$t'_1 + t'_2 = \text{const2} = t_1 + t_2 \quad (3.2)$$

Which is in turn equal to ‘const1’. This situation therefore makes it difficult to demodulate separately the signals from individual transmitters at the receivers.

3.5.2 Pilot Symbol Tracking

Digital Audio Broadcasting (DAB) uses pilot based symbol base on a constant amplitude zero-autocorrelation(CAZAC) symbol. Due to it’s good resilience to interference, this technique is considered to be one of the most reliable techniques. This technique makes use of the synchronization symbol (1m) which is available in every DAB signal data frame (96 ms). Hence, to determine the phase change,

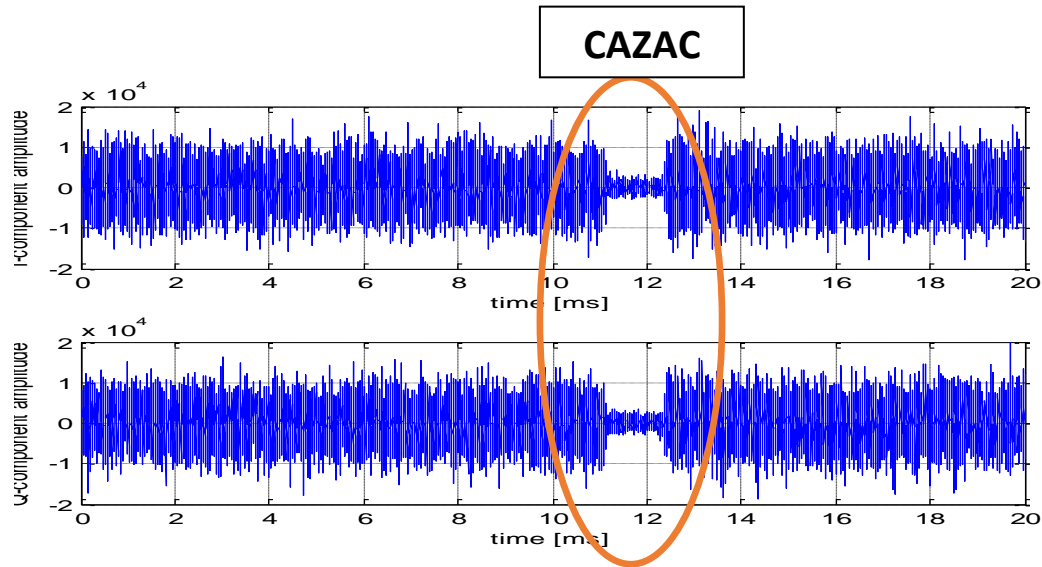


Figure 3-5: Illustration of the DAB signal data from showing the pattern of CAZAC synchronization symbol.

we need to recover that pilot (synchronization) symbol through demodulation of the signal.

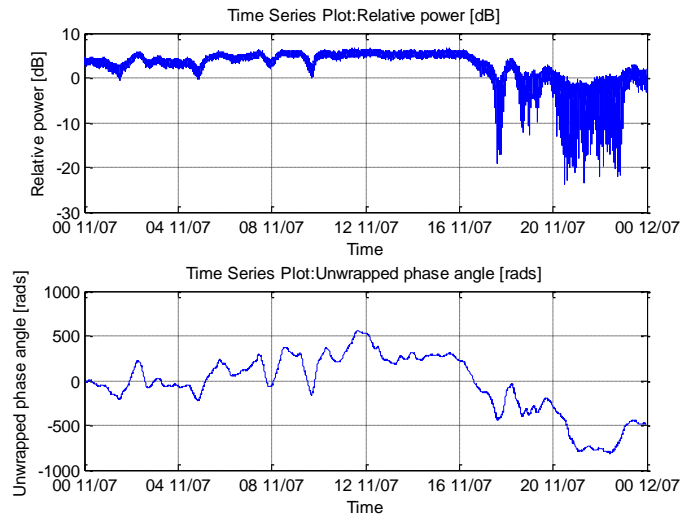
This method still requires transmitter phase stability. The issues of individual transmitters and transmission paths faced using the auto & cross correlation method was resolved in this method.

The advantage of using the pilot symbol tracking methodology is that it can estimate the direct path between a pair of transmitter and receiver. One major disadvantage in this method is the expensive computation costs in comparison to the other phase estimations methods.

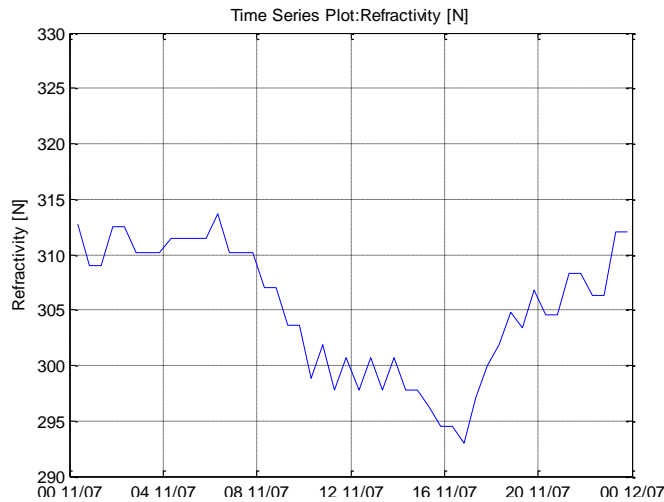
Figure 3.6 shown is an illustration of magnitude and phase against time obtained using the DAB/DVB data. Shown in Figure 3.6 is an illustration of magnitude and phase data obtained using single site autocorrelation(SSA) methodology. The data shown in figure was collected on 8th July 2012 using the receiver located at University of Bath from the nearest transmitter location at Mendip. The top part(a) of Figure 3.6 shown is a plot of relative power (magnitude) in (dB) against time(days) and part(b) shows the variation in phase angle in radians against time. Using the information obtained from the phase data we can calculate the excess delay. Part(c) of the Figure 3.6 shown is the variation in refractivity(N) against time.

The data used in part(c) for this comparison analysis was from the UK meteorological office station data located at Bristol airport. The choice of refractivity data from Bristol airport was mainly due to it being the closest available station data. Figure 3.7 clearly demonstrates that there is a correlation in the propagation path showing the changes in the phase of DAB/DVB data, due to the variation in refractivity, thereby showing the effects of refractivity.

Further, shown in Figure 3.7 is another example showing the effects of refractivity along the propagation path and the data for this analysis was recorded on the 9th July 2012.

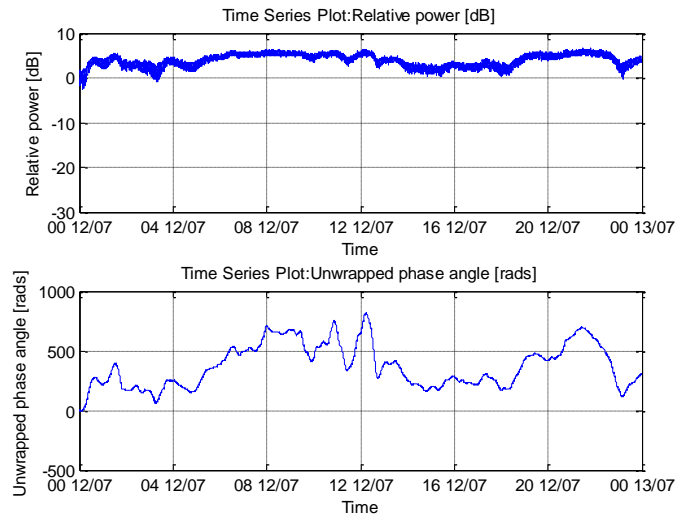


(a) Single-Site autocorrelation of 222.064MHz DAB signal recorded at University of Bath - top: magnitude and bottom: phase

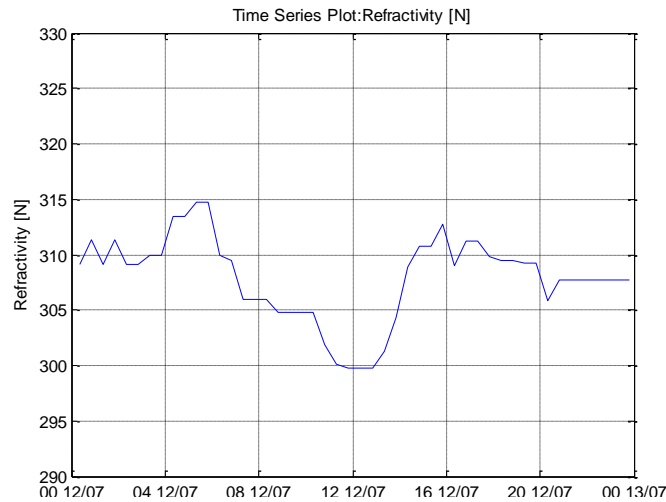


(b) Meteorological Station data recorded at Bristol Airport.

Figure 3-6: Figure(a) represents magnitude and phase of the data recorded at University of Bath from nearest transmitter site Mendip using Single-site autocorrelation of 222.064MHz DAB signal. Part(b) shows the variability of refractivity against time(days) using the data from UK meteorological station data collected at Bristol Airport - 11th July 2012



(a) Single-Site autocorrelation of 222.064MHz DAB signal recorded at University of Bath - top: magnitude and bottom: phase



(b) Meteorological Station data recorded at Bristol Airport.

Figure 3-7: Figure(a) represents magnitude and phase of the data recorded at University of Bath from nearest transmitter site Mendip using Single-site autocorrelation of 222.064MHz DAB signal. Part(b) shows the variability of refractivity against time(days) using the data from UK meteorological station data collected at Bristol Airport - 12th July 2012

3.6 Summary

The focus of this chapter was to give an understanding and overview of using the DAB and DVB as a remote sensing instrument. Here we have explained the procedure and set-up used to measure the DAB and DVB signals. Also, we have discussed about the different features and also the availability of DAB and DVB signals in UK. In the latter section of this chapter, we have given details about the various retrieval algorithm used in the initial phase of this study to estimate refractivity. The results obtained using the various retrieval methodologies has been shown.

Initial experiments which have been demonstrated at the University of Bath using a receiver has given a positive representation of phase changes but it requires furthermore analysis and also needs to be validated. Hence, further analysis is required to understand the phase delay and to show if we can use the DAB/DVB signals as an alternative to existing remote sensing instruments. In the next chapter, we will look into ways to estimate the atmospheric delay using the ray tracing technique.

CHAPTER 4

RAY TRACING

This Chapter will introduce the process of ray tracing and the methodology to extract ray traced path delay. This chapter describes the step by step process of ray tracing from the refractivity calculations of the atmospheric constituents parameters using data-sets to the estimation of path delay. This chapter begins by giving an overview of the ray tracing. Further we show the different ray tracing types available and their working methodology.

This chapter also shows the implementation of the ray tracing modelling, which is used to obtain the path delay. We also show the process of the ray tracing system of equation using Eikonal equation. Finally, this chapter explains the interpolation process used in the preprocessing of the data used for ray tracing system modelling.

4.1 Ray Tracing - A Review

Predicting the ray/signal path propagation between the transmitter and receiver with refractivity changes is one of the most common problems in tropospheric radio signal propagation. Determination and calculations of propagation path of the radio waves using a graphical or mathematical approximation technique by complying with laws of reflection and refraction is known as “Ray tracing” [60]. Ray tracing is considered to be the very accurate and comprehensive way to calculate atmospheric delay/phase delay.

Since the beginning of 1966, although ray tracing has particularly gained special attention over the last decade, it has been the generally used technique for propagation of radio signal through the atmosphere and many other applications by geophysics [26]. The basic principle of ray tracing in Radio science is to find the shortest and all the possible ray paths between the transmitter and the receiver. It takes into account the effects of various phenomenons such as tropospheric refractivity, reflection and scattering. In the case of this research we have considered only the refractivity variability effects on the signals.

In the past ray tracing has been used in a wide range of mapping functions for calibration. Most commonly ray tracing were processed using the Radiosonde data profiles [27] and [28], climatologist and NWM by [29].

The computation process to estimate delay along the signal path is based on a theory of geometrics applied over a layers of the earth such as spherical and concentric. The layers are assumed to have constant refractivity or variable refractivity based on the desired application. Ray path and refractivity changes along the boundary between layers are calculated using continuous application of Snell's law. For a homogeneous atmosphere, the path would simply be a straight line, whereas propagation of ray through a heterogeneous atmosphere such as troposphere. The refractivity may vary resulting in a point to point ray bending thereby providing useful information about the atmospheric parameters and its effects on the variability in the troposphere.

In order to achieve accurate results, the most significant effect is based on the accuracy and resolution of the data sources. The data sources are usually obtained from NWM models, Radiosonde data, and DAB/DVB data in the case of this research. Refractivity measurements along the propagation path are calculated based on the knowledge of atmospheric parameters such as pressure, water vapour and temperature[12][26][30].

Over the past few years, the growing need to find a computationally fast way to predict the dominant ray paths in a complex 2-D and 3-D environment has made the way for a number of ray tracing methods. These are as explained in detail in the following section.

4.2 Ray Tracing Schemes

There are different schemes for solving ray tracing in “2-Dimension” and “3-Dimension” for determining the ray path between the transmitter and the receiver in a varying heterogeneous or constant medium. The two methods which are more commonly used in ray tracing are categorized based on initial value problem and boundary value problem as shooting and bending method. These two methods traverse along the path based on exploitation of the equations of ray tracing. Shown in the Figure 4-1 is an Illustration of the refractivity profile using the radiosonde data, showing the variation of the refractivity against height(km).

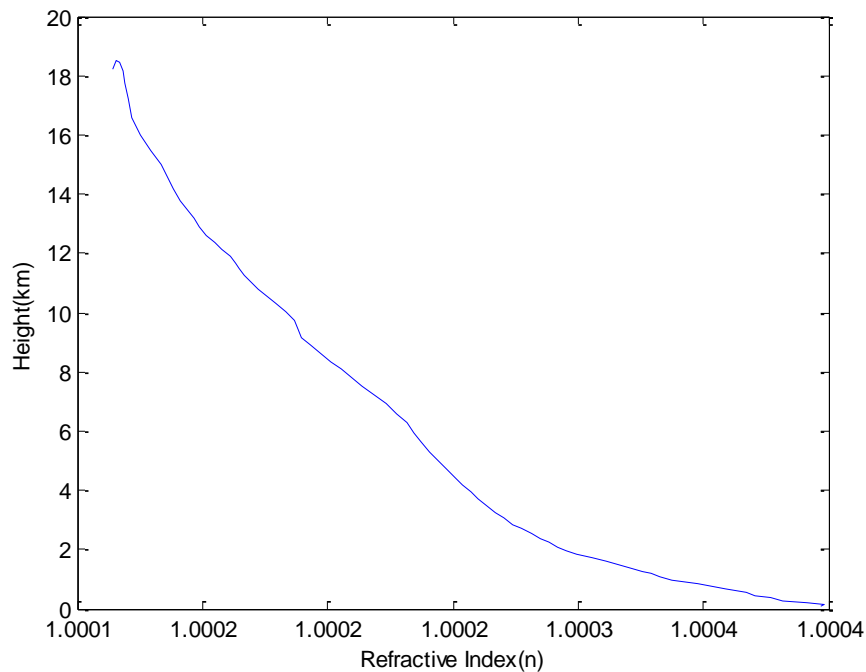


Figure 4-1: A typical vertical refractivity profile showing variation of refractivity against height.

4.2.1 Ray Shooting Method

The first approach is the ray shooting method. One of the methods of ray tracing is wherein the initial direction and origin of the ray is estimated and this process of initial value problem is continuously repeated until a required estimate of the initial condition is obtained. This method uses a brute force method to calculate

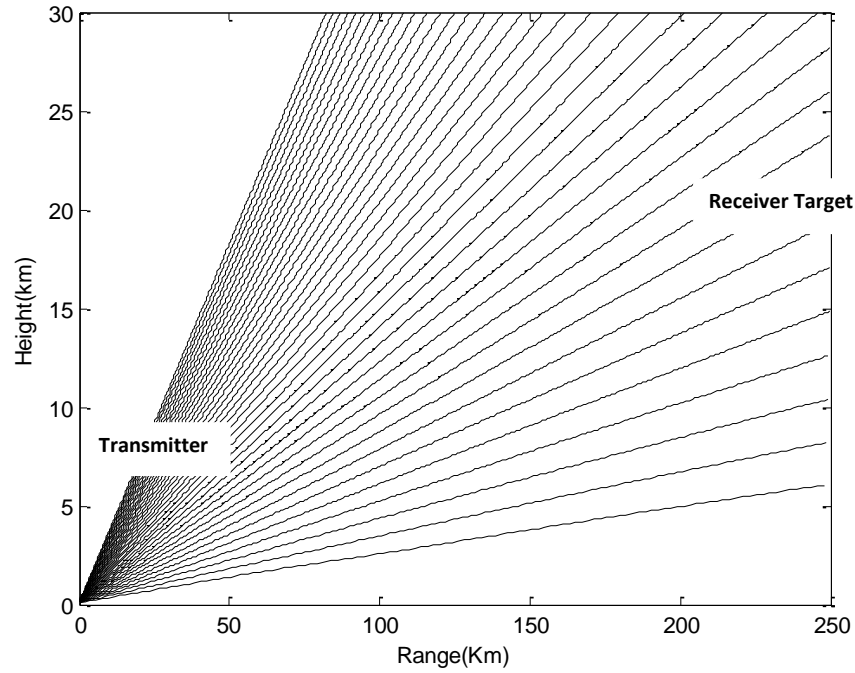


Figure 4-2: A typical example of a ray shooting method showing a fan of rays from the transmitter and some rays shown reaching the receiver.

the ray path by shooting a fan of rays from the transmitter in a 2-D or 3-D space. Propagation of each of the rays is traced individually in step size until they reach the receiver. Based on the time of arrival and its direction, useful information can be computed. Figure 4-2 shows the typical example of a ray shooting method where the rays are continuously launched until the ray/signal reaches the desired receiver target[31]. Shown above in the Figure 4-1 is the typical atmospheric refractivity profile used to create the ray tracing environment for the example shown in Figure 4-2.

4.2.2 Ray Bending Methods(Relaxation Method)

Bending method is an alternative ray tracing method to trace a ray path, which is based on an initial estimation. This method, is also known as a relaxation or variation approach. The Bending method is solved forming a set of differential

ray tracing equations to derive a boundary value condition which is then solved iteratively using numerical methods.

The progress of the ray is accomplished by the iterative perturbations of the initial arbitrary path that joins the source and receiver with the ends fixed, until a true or the optimum path is obtained. A true path obtained via iterative adjustment must satisfy the Fermat's principle or finite difference methods[31]. Figure 4-3 is an illustration of the principle of bending method ray tracing by perturbing the initial two point path until it satisfies Fermat's principle. There are many algorithm that have been developed over the years, for example those developed in [42][43][44][45]. The most common technique used was the finite difference technique to solve a set of first order differential equations. Different options for ray tracing using bending method used over the years is clearly explained in [31].

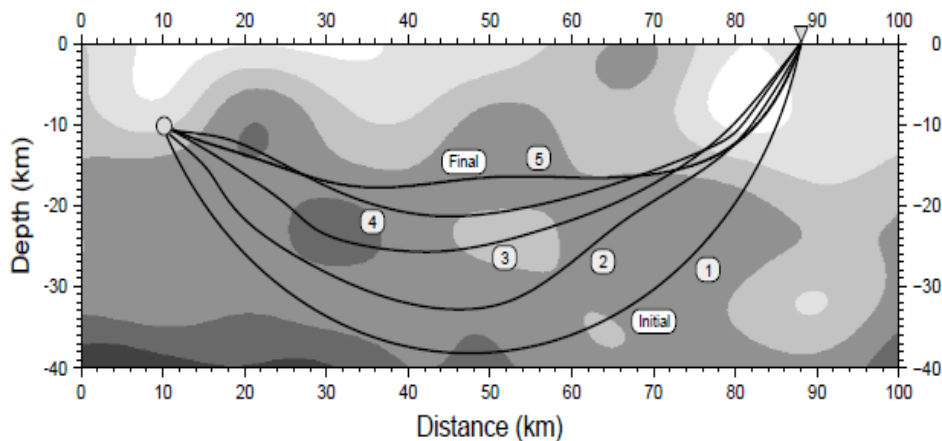


Figure 4-3: Example Illustrating the ray tracing using bending method by perturbation of the initial two point path until it satisfies Fermat's principle[31].

In general, the major difference between the shooting and bending method is that there always exists a ray path(true path) in shooting method, whereas in bending method a ray path is never a true path until it converges. Here at all the stages of iteration, the ray is a mere path which is non-existent between a source and a receiver and not the actual true ray path. Figure 4-3 shown above is a typical example of bending method. Here an initial ray path assumed is numbered

as (1) and the ray path is adjusted according to the different conditions (for e.g. refractivity) and satisfying the ray tracing equations [31] are numbered (2), (3), (4) as shown in the Figure 4-3.

4.3 Refractivity Calculation From Atmospheric Parameters

As described in literature section of Chapter 2, “Atmospheric refractivity ‘N’ is often used to focus on the small difference of the index of refraction with respect to vacuum” [65]. The sum of the indices of refraction due to dry and wet components of the troposphere is known as the index of refraction ‘n’. The relationship between the index of refraction and refractivity was given by Equation 2.1 and it is as below[33].

$$N = (n - 1) \times 10^6 \quad (4.1)$$

The basic measurement principle is that of change in signal phase associated with change in the effective refractive index along the propagation path[33][55]. The refractivity of the atmosphere in N-units can be written as:

$$N = 77.6 \frac{P}{T} + 3.73 \times 10^5 \frac{e}{T^2} (Nunits) \quad (4.2)$$

Where ‘P’ is atmospheric pressure(hPa), ‘T’ is temperature(K) and ‘e’ is the partial pressure of water vapour(hPa). Further, the relationship between water vapour pressure ‘e’ and relative humidity ‘RH’ is given by:

$$e = \frac{H.e_s}{100} \quad (4.3)$$

Where, ‘H’ is the relative humidity and ‘e_s’ is the saturation water vapour pressure.

4.4 Ray Tracing Approach

There are different ray tracing methods to determine the ray path, based on Snell’s law or the Eikonal equation. A simple and elegant approach is ray racing through the medium using the Snell’s law in Cartesian coordinates. Initially for simplicity we start the ray tracing problem in a simple two dimensional medium.

Here the signal is traced from its initial position through the troposphere where the delay and the path are adjusted accordingly as the signal encounters different refractivity conditions with varying height. Hence we developed a ray tracer based on the ray shooting technique using Matlab.

The ray-tracer modelled here is on the lines of the work that was implemented in [33], and has been adopted by this author with several modifications. With reference to Figure 4-4, this package requires user specified maximum range ('zlast' in km), initial angle, height ('xlast' in km), the step size ' Δx_{step} ' and also the origin of the source point 'xsource'. The ray tracer shoots the fan of rays at an angle specified by the user, and thereby allowing the ray to propagate through the propagation path characterised by variation of refractivity 'N' with height 'h'.

Here the medium/propagation path is divided into a series of thin layers with varying refractivity conditions. The step increment size for each layer is user specified. The progress of ray along the path is achieved through successive applications of Snell's law at the boundary between two layers.

The refractivity value 'N' is calculated from the atmospheric parameters pressure 'P', temperature 'T', and humidity 'H', which varies with respect to the height. The refractivity formulation described in Chapter 2, is used to calculate the refractivity from these atmospheric data parameters. The atmosphere data sets which provide the parameters are obtained through the Radiosonde data source. Initially to test the model, we consider the data from the Radiosonde data source for refractivity calculations, which closely matches the DAB/DVB data for tropospheric conditions.

4.5 Ray Tracing Algorithm

In this section we will give a detailed explanation of the stages of a ray tracing approach we have used. The algorithm described below follows Figure 4-4 for the notations and assumptions.

1. In this approach, the transmission of signal path from the transmitter to the receiver is considered as "Ray".
2. The point 'P' is the intersection between two connecting layers.

3. The height of the atmosphere is modelled for up to a range of 30 Km and the horizontal range is considered to be 100 km.
4. The step size, which is also the height of each layer is represented by the symbol ' Δz '. The subscript 'i' corresponds to the current layer of the ray and it starts from 0 to the end. The refractive index in each layer of height ' Δs ' is assumed to be constant throughout that layer.
5. The refractive index ' n ' is calculated from Radiosonde weather data using the different equations as explained in the Chapter 2.
6. The distance between the two adjoining layers from the intersecting points is the ray path length ' S_i ' or ' Δs '.

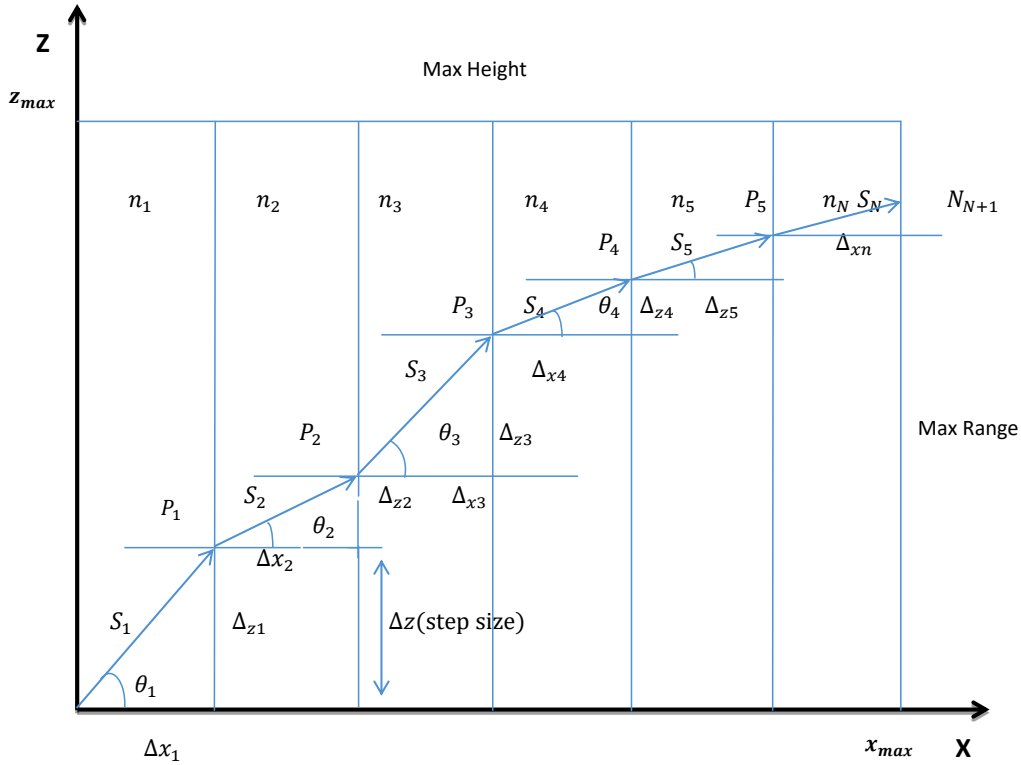


Figure 4-4: Geometrical representation of a ray tracing algorithm.

Initially, at the source the parameters such as initial angle, final angle, maximum range, height and the step size ' Δz ' are all initialized pertaining to that layer.

The components ‘ x ’ and ‘ z ’ are initialized to 0. The source height initialization forms the basis of the initial layer. The ray tracing model shoots a fan of rays continuously from the source. The first ray propagates through the initial layer and hits the next point, the ray angle and the outgoing (refracted) ray angle at this point is obtained through the Snell’s law as,

$$n_i \sin(\theta_i) = n_{i+1} \sin(\theta_{i+1}) \quad (4.4)$$

Until the ray reaches the maximum height, it continues to propagate through the layers. The range distance ‘ x ’, the next ray angle ‘ (θ_{i+1}) ’ where ‘ i ’ is the index and the total ray path ‘ s ’ are calculated using the equations as shown below.

$$\Delta x_{i+1} \text{ or } x = |\Delta z_i| \tan \theta_{i+1} \quad (4.5)$$

The path length ‘ Δs ’ or ‘ s ’ is obtained using the relation:

$$\Delta s_{i+1} \text{ or } s = \sqrt{\Delta z^2 + \Delta x_{i+1}^2} \quad (4.6)$$

Once the path length is calculate, the coordinates ‘ x ’ and ‘ z ’ of the next point is obtained using the formula,

$$x_{i+1} = x_i + \Delta x_{i+1} \quad (4.7)$$

$$z_{i+1} = z_i + \Delta z \quad (4.8)$$

Here ‘ Δz ’ is the step size of the layers. From rearranging Equation 4.4, we get the Equation 4.9 shown below to calculate the next layer outgoing ray angle at the interface, and is given by:

$$\theta_{i+1} = \frac{n_i \times \sin \theta_i}{n_{i+1}} \quad (4.9)$$

Finally, in order to determine the tropospheric delay, we need to find the ray path length ‘ S_i ’ at every layer as the ray moves from the ‘ i^{th} ’ layer to the end. And then to obtain the delay induced in that layer, the ray path length is then multiplied by the refractivity ‘ N ’ in that layer. This process is then continued for every layer along the ray path length.

The total tropospheric delay is thus calculated by summation of delay in-

duced in every layer along the path from the transmitter to the receiver.

$$Totalpath = \sum_{i=1}^K S_i \text{ or } \Delta S_i \quad (4.10)$$

Where, ‘ i ’ denotes index of refraction of the ray and ‘ K ’ is the number of ray segments along the ray path length [32]. Therefore, the delay in the ray propagation path can be obtained from the difference between the total path and the geometric path length (as explained in Chapter 2), and is given by:

$$\Delta S = \int_{Tx}^{Rx} n(s)ds - \int_{Tx}^{Rx} ds = \int_{Tx}^{Rx} (n(s) - 1)ds \quad (4.11)$$

where ‘ $n(s)$ ’ is the refractive index as a function of position ‘ s ’, and the first integral is the propagation path with varying refractive index and the second one is the straight line path length between the transmitter and receiver[55].

4.6 Ray tracing Using Eikonal Equation

The propagation of a ray along the rays path is defined by the fundamental equation of ray optics is the Eikonal equation [34], and is given as:

$$\frac{d}{dl}\left(n\frac{dr}{dl}\right) = \nabla n \quad (4.12)$$

Where, ‘ ∇n ’ is the gradient vector field of refractivity, ‘ r ’ is the ray position vector along the ray path and ‘ dl ’ is the differential displacement along the ray path. It can be seen from the Equation 4.12 is the significant dependency of ‘ r ’ on the index of refraction ‘ n ’ and the gradient ‘ Δn ’. Ray propagation through the medium and its positions at any given distance depends on the two methods (initial and boundary conditions) both of which have different sets of conditions, similar to that of ray tracing using Snell’s law as described in the previous section.

In initial value ray tracing, the final position is determined with the help of Equation 4.12 where the initial conditions are the initial position and the initial direction [35]. Similarly in boundary value problem, the initial direction or the initial angle is determined through the Equation 4.12 based on initial and final positions.

The differential equations shown in (4.12) can be solved in a number of methods such as Runge-Kutta [36], perturbation method [35] or the shooting method [29]. The ray tracing procedure employing shooting method (initial value problem) is discussed below. The equation for ray tracing derived here is based on the lines of work developed by [41].

The tangent vector based on the position ‘ r ’ which is a unit vector is given by:

$$dl = ||dr||, \quad (4.13)$$

which is the normal of vector ‘ dr ’. Equation (4.12) can be expanded as:

$$\frac{dn}{dl} \frac{dr}{dl} + n \frac{d^2r}{dl^2} = \nabla n \quad (4.14)$$

The gradient of refractivity can be obtained numerically from the partial derivatives involved in the Eikonal equation. The equation for ‘ ∇n ’ can be written in Cartesian coordinates as:

$$\nabla n = \frac{\partial n}{\partial X} \hat{i} + \frac{\partial n}{\partial Y} \hat{j} + \frac{\partial n}{\partial Z} \hat{z} \quad (4.15)$$

The Equation (4.12) and (4.13) can be reduced to a set of first order ordinary differential equations for simplicity and stability, hence:

$$\frac{dr}{dl} = \hat{I} \quad (4.16)$$

And,

$$\frac{d(n\hat{I})}{dl} = \nabla n \quad (4.17)$$

Where, ‘ \hat{I} ’ is a unit vector tangent to the ray path. We know that the refractive index ‘ n ’ as explained in the Chapter 2, is given by:

$$n = (1 + 10^{-6}) N \quad (4.18)$$

Where, ‘ N ’ is the refractivity which depends on the pressure, humidity and height. Refractivity is expressed in terms of N-units.

The Equation(4.14) can be written using Equation(4.15) as:

$$\frac{dr}{dl} = \frac{[\nabla N - I(\nabla N \cdot I)]}{(N + 10^6)} \quad (4.19)$$

The non-linear term and the higher magnitude order in the denominator can be replaced by substituting ' $\frac{dI}{dl}$ ' with another equation which defines the radius of curvature at the path ' ρ ' such that:

$$\frac{d\hat{I}}{dl} = \frac{\hat{U}}{\rho}(e) \quad (4.20)$$

Where, ' \hat{U} ' is the normal to the ray path trajectory and perpendicular to ' \hat{I} ', and ' $\hat{U} = 1$ '. Hence to determine ' ρ ', we take the scalar product of both sides of ' d ' with ' \hat{U} ' and thereby also using Equation(4.17).

$$\frac{1}{\rho} = (u \cdot \nabla N) \times \frac{1}{(N + 10^{-6})} \quad (4.21)$$

On substituting (4.18) in (4.17), we have:

$$\frac{dr}{dl} = \hat{I} \quad (4.22)$$

$$\frac{dI}{dl} = \frac{U}{\rho} = U \left[\frac{U \cdot \nabla N}{N + 10^6} \right] \quad (4.23)$$

Since the above set of equations involves ' U ' along with ' r ' and ' I ', this system of equation is not a closed system.

The above system can be made a closed system in a two dimensional case by using ' \hat{U} ' and ' \hat{I} ' orthogonality which is given by: $\hat{U} = \hat{x} \times \hat{I}$. Here ' \hat{U} ' and ' \hat{I} ' are in the same plane as transmitter and the receiver and ' \hat{x} ' is the unit vector in the direction of ' x ', hence the system can now be solved using numerical methods like Runge-Kutta.

On the other hand while considering the three dimensional case, the whole system (f) can be solved directly. In explicit method of integration the system breaks down. To ensure $||I\hat{I}|| = 1$, the step size used for integration needs to be very small which eventually stops the integration process. And this is known as stiffness which can be cured using implicit integration method. In this system there is a coupling of the present and past values. Again this method can be solved numerically using Runge-Kutta method.

4.7 Interpolation of Raw Radiosonde Data

For the refractivity field profile, we need to calculate the refractivity along the propagation path. The atmospheric data parameters obtained from the Radiosonde data source was used to provide data at every instant along the transmission path. Due to the process and the way radiosonde data is collected, the data source usually ends up with the missing data or “*NAN's*” in the atmosphere parameters (‘Temperature’, ‘Pressure’, and ‘Relative Humidity’) at certain points in the height range. To fill this gap in the data sets we use nearest neighbour interpolation, so as to get the data at respective heights as the ray propagates through the medium.

For computation efficiency, we pre-compute refractivity from the atmospheric parameters, rather than computing (iterating) the refractivity using the atmospheric parameters at every stages of the ray propagation through the medium. The data source used was radiosonde data and this was obtained from the BADC(British Atmospheric Data centre).

4.8 Summary

This chapter introduced the process of the ray tracing systems. Types of the ray tracing and their methodology was also shown here. This chapter also introduces how ray tracing algorithm is used to extract the path delay through the varying tropospheric environment. The ray tracing simulation results are analysed and explained in Chapter 4. In the next Chapter 5, we perform the analysis of path delays obtained from the ray tracing algorithm. We also show path delay analysis over different conditions.

CHAPTER 5

PATH DELAY VARIATIONAL ANALYSIS

In Chapter 4, we discussed the implementation and the process of ray tracing to determine delay. For a given refractivity profile of the troposphere, solving the equations and following the steps of algorithm as shown in Chapter 4, ray traced atmospheric propagation delay can be obtained. The process of calculating the ray traced delay from atmospheric constituents is clearly explained in Chapter 2 and Chapter 4. In this chapter, we will analyse the ray tracing results for different conditions and scenarios. We will also look into the different data types used to obtain atmospheric refractivity profile for the process of ray tracing. We further show the analysis of the results under different conditions such as refractivity profile, variations in transmitter and receiver height and the range. Here, we aim to show and estimate, how much the radio signal is affected by refractive medium in the signal propagation path and also look into any other factors affecting the propagation path, thereby also calculating the delay.

In the second part of this Chapter, we carry out the statistical estimation of the delay obtained from the ray tracing. We further perform different statistical analysis techniques such as mean, standard deviation and moving average variability over different times of the year. Relativity analysis on the variation of delay depending on different parameters such as season, time of the day, comparison of summer month variation against winter variations, range and height respectively are also shown.

5.1 Delay Variability and It's Effects on Signals

In Chapter 2, we went into details of different aspects of atmospheric delays - it's definition, types and the signal propagation effects. In Chapter 4, we went through the process of modelling the radiosonde data/remote sensing measurement data to obtain the delay. This delay was obtained through the process of ray tracing (Ray Shooting method). The methodology and the formulation used is explained in Chapter 4. On obtaining the path delay from ray tracing modelling, the next stage is to validate and analyse the delay. To analyse, if the ray traced delay obtained is dependent on any atmospheric refractivity and if the delay is large enough to make any significant effect on the signal propagation in the lower boundary, we perform different analysis study.

5.2 Ray Tracing Simulation and Analysis

5.2.1 Simulation Results Using Tri-linear Synthetic Refractivity Profile Data

The ray tracing algorithm described in Chapter 4 was implemented to measure the total path delay. The ray tracing simulation to obtain troposphere propagation path delay differences between the two fixed transmitter and receiver locations was performed using Radiosonde data-set, simulated refractivity model data. Furthermore, here we use this ray tracing model to determine the propagation delay along the path for different factors and combinations which will be discussed later in this Chapter. Initially, we have used different range of profiles to differentiate propagation and delay occurrence between different atmospheric profiles. Later on we will go into further analysis and results to show the path variation effect based on parameters such as propagation range, step size range movement along the path, time of the year and seasons.

To begin with here, firstly we have considered a refractive profile with no variability at all, which is typically a uniform refractive environment. The uniform refractivity profile of the atmosphere is as shown in Figure 5-1. The ray propagation through the uniform refractivity medium should be equivalent to a straight line propagation path. The ray propagation through this environment is as shown in Figure 5-3. Here we can clearly see that all the rays take a straight

line propagation path with no bending or variation in the ray propagation path. The ray tracing profile used for the simulation environment in obtaining Figure 5-3 is from the profile shown in Figure 5-1.

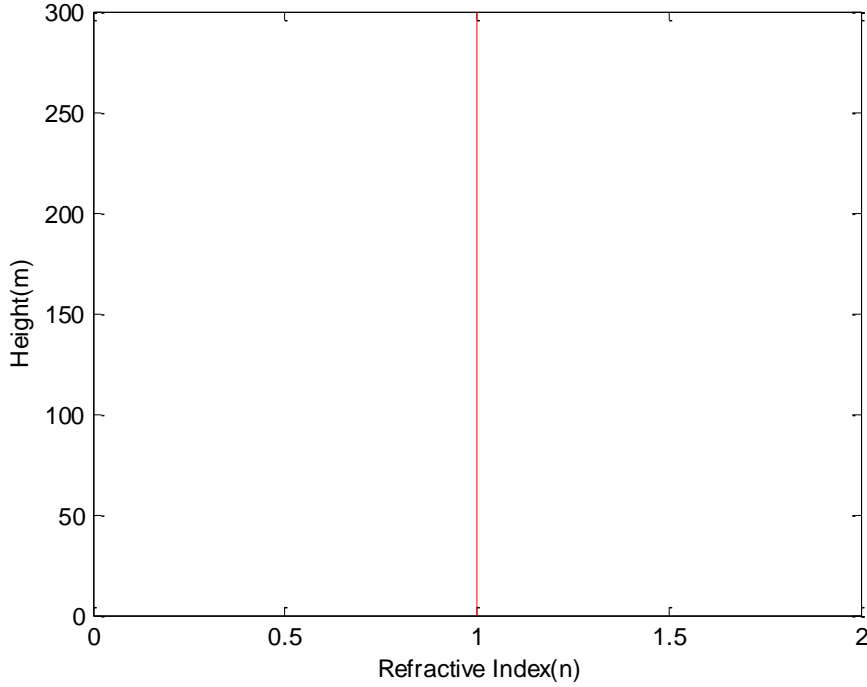


Figure 5-1: *A vertical refractivity profile for constant refractivity.*

Figure 5-3 gives a characteristic example of a ray propagating through an environment with constant refractivity across the propagating path. Here the rays are shown shooting through a medium where the refractivity (n_1 and $n_2 = \text{constant}$, from Equation 4.1), and the rays are shown taking a straight line propagation path. In this example, the rays are shown shooting from the source with an initial angle of 60 degree and the final ray with an angle of 90 degree. Therefore, total 30 rays is evolving from the source and this is done with an incremental step angle of 1 degree between two rays. The initial transmitter source considered is at a height of 50m, total range and total height was considered to be at 25 km and 3000m, respectively. The step size increment is 0.2m between layers. As can be clearly observed from Figure 5-2, the fan of rays continuously propagating through the medium with constant refractivity until it reaches the maximum range and height.

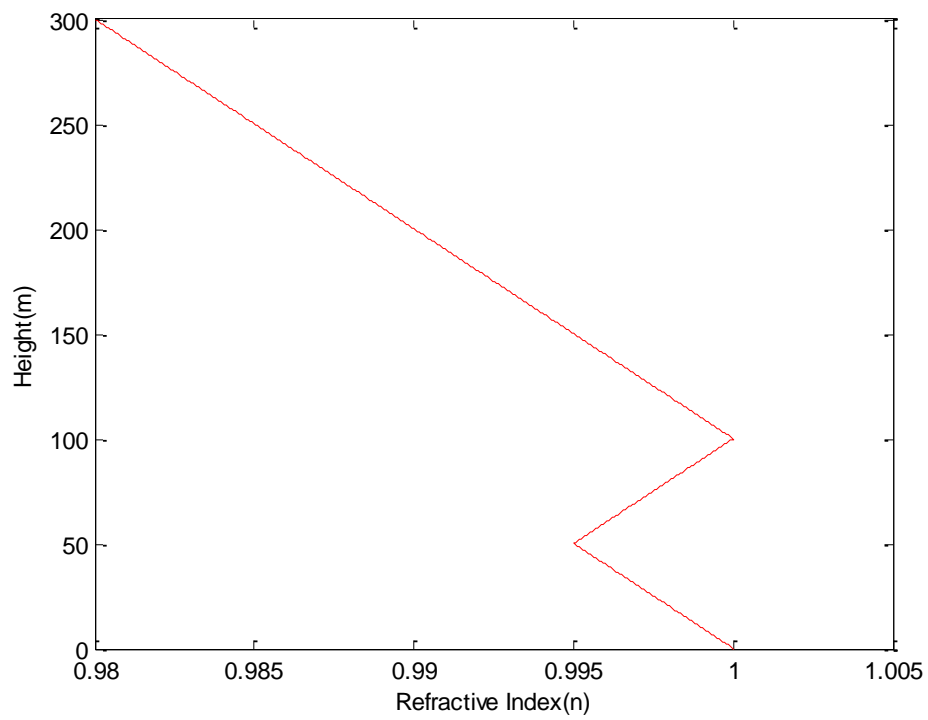


Figure 5-2: *A plot showing a vertical refractivity profile for the variation of refractivity with height.*

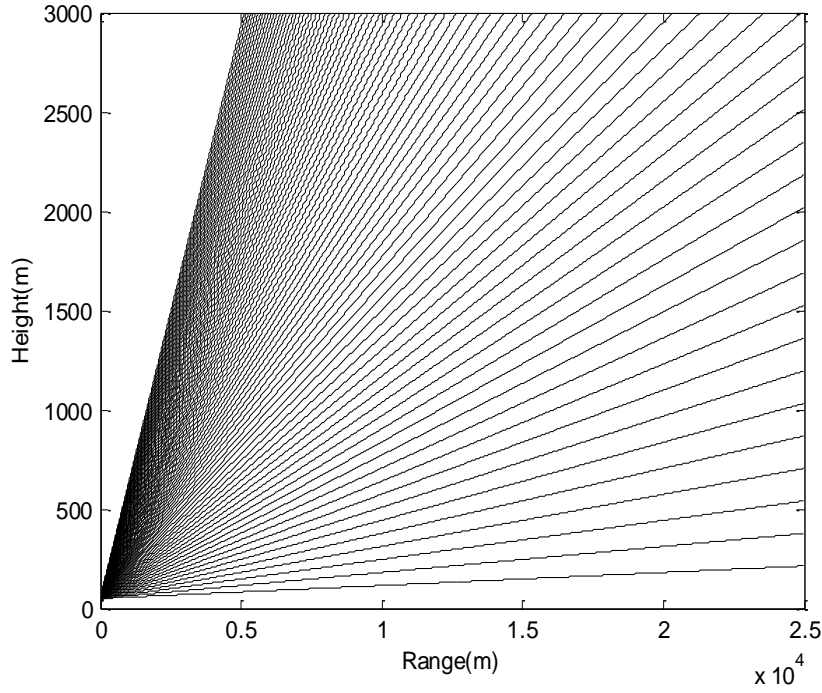


Figure 5-3: Ray tracing in a constant refractivity with predefined initial conditions.

In Figure 5-2, we have a refractivity profile which is varying with height in comparison to the uniform refractivity profile shown in Figure 5-3. A synthetic profile was used and was obtained using the Equation (5.1). Figure 5-4 shows another example of ray tracing through the medium. It can be seen that there is variation of ray path with height along the propagation path. In this case, a propagating medium is of varying refractivity at every point along the ray path (i.e. a non-homogeneous environment) as compared to Figure 5-3. The refractivity environment profile is obtained using the tri-linear refractivity formula as shown in Equation [5.1].

$$n(x) = \begin{cases} 1 - a_0x, & x < X_{D1} \\ 1 - a_0(2X_{D1} - x), & X_{D1} < x < X_{D2} \\ 1 - 2a_0(X_{D1} - X_{D2}) + a_0x, & X_{D2} < x \end{cases} \quad (5.1)$$

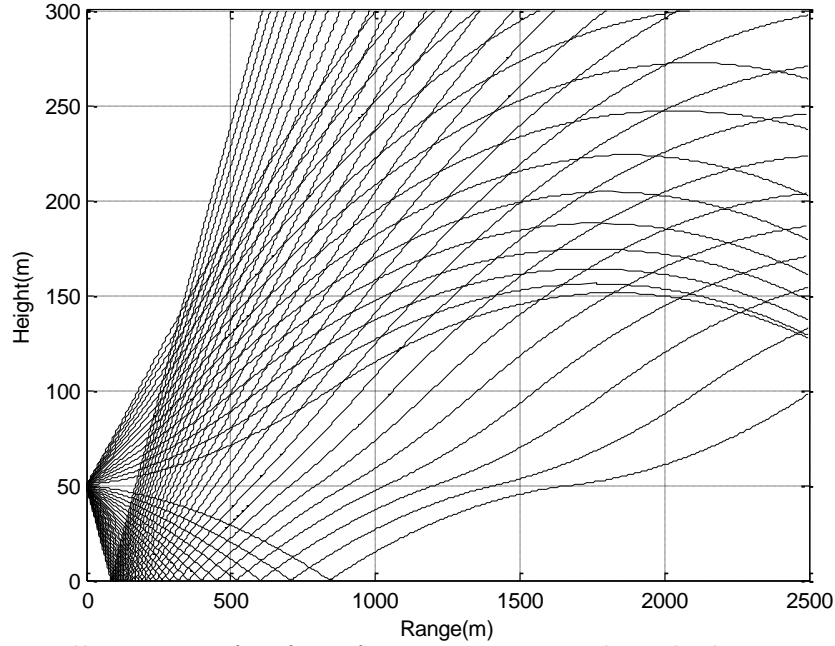


Figure 5-4: Illustration of a fan of ray propagating through the atmosphere with varying refractivity conditions - source height = 50m, total range = 2500, maximum height = 300 m, initial angle = 75 degrees, final angle = 120 degrees, angle increment = 1 degrees, step size = 1 and finally the slope of the refractivity was set to 0.001 km. The ducting and the anti-ducting conditions were at 50m and 100m.

For the analysis shown above in Figure 5-4, the atmospheric refractive profile simulation environment used here is as shown in the Figure 5-2. The initial fixed source point was randomly chosen to be 50m, the total range for the signal propagation was fixed at 2500m and the maximum height a ray/signal can travel was fixed at 300m. We also need to choose the initial and the final angle with an increment angle in order to make sure one of the ray/signal hits the desired fixed target. These were chosen to be 75 degrees, 120 degrees and 1 degree respectively. Refractivity equations shown in Equation 5.1, was used to create the refractivity profile for the simulation medium, we also need to choose appropriate values for slope of the refractivity, ducting and anti-ducting (X_{D1} and X_{D2}). The values for these parameters were fixed respectively at 0.001 km, 50m, and 100m.

Figure 5-4, shown is a fan of rays shooting between the initial and final angle with an increment angle of 1 degree. The rays are continuously in shooting mode till one of the ray reaches the receiver. The difference that can be noticed between the Figure 5-3 & Figure 5-4 is the change in the propagation path the signal takes with or without the refractivity.

In the later examples, we will give a detailed explanation and analysis about how the ray reception or the ray angle of arrival is calculated and estimated. We will also see how much bending and delay occurs along the propagation path on using the remote sensing data set which will be the Radiosonde data-set in our analysis. The use of radiosonde data-set was again mainly considered due to the consistent, large and easy availability of current and historical data.

5.2.2 Ray Caustics and Reflections

Another case of ray tracing simulation is the phenomenon of Ray Reflection from the boundaries. Although, here in this research we have ignored ray caustics and reflections from the surface, we have still covered this here, so as to give an example and overview to show the occurrence of reflections and ray caustics. This process was beyond the scope of this research at this stage and we are currently focussed only on the point to point delays with no reflections and caustics.

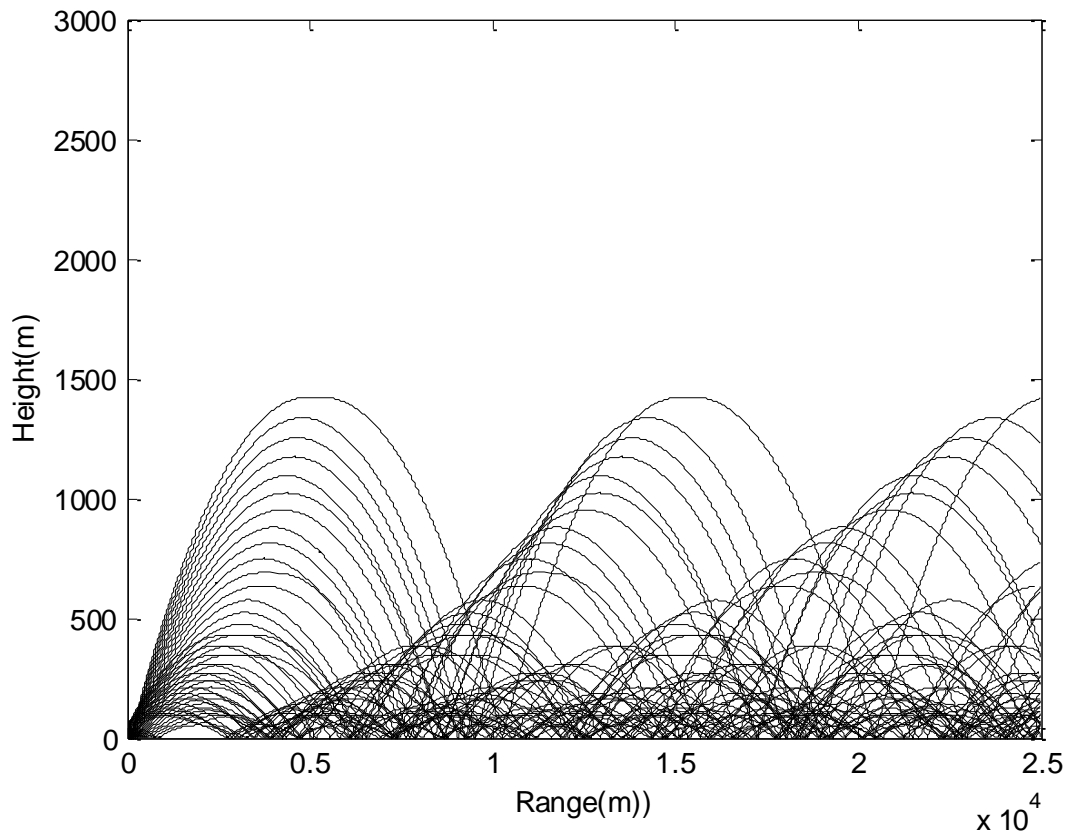


Figure 5-5: *Typical example of ray tracing showing a fan of rays through an environment with varying refractivity conditions showing ray caustics and reflections from the surface.*

This process of ray caustics and reflections was solved by bending the ray in the upward direction with the same angle in the opposite direction as when the ray hits the boundaries [32]. Figure 5-5 gives a characteristic example for

ray propagating through a medium with varying refractive index and thereby showing the occurrence of bending, refraction and reflections from the bottom surface. Also shown in the Figure 5-5 are the reflections from the bottom surface and the cases for ray caustics.

The condition when the rays reach almost 90 degrees is known as the “Ray Caustics”. This was solved in a way very similar to ray reflection. In this case the rays with ray angle of greater or nearing 90 degree are bent downwards for the ray propagating upward and vice versa. Similarly for ray angles reaching 270 degrees the same procedure is applied [32].

As shown in Figure 5-5, the rays are propagating through the environment with heights of ducting ‘xd1’ and anti-ducting conditions ‘xd2’ at 45 and 120 degrees, respectively. Whilst the other parameters and conditions chosen here are: height of the source = 50m, total range = 2500m, height= 300m step size=1 and ray increment, initial and final angles were 1 degree, 75 degree and 120 degree respectively.

Another special case in Figure 5-4 and Figure 5-5, from the application of tri-linear refractivity profile is the occurrence of ducting and anti-ducting conditions. Take the example in case of Figure 5-5, here surface ducting occurs from the bottom surface to the height of 50m. There can be also be an possible occurrence of rays getting trapped to the surface and the elevated duct.

5.2.3 Ray Tracing Using Radiosonde Data-set Profile Data

In the previous section, we have seen how the ray propagates in a medium of synthetically modelled atmospheric profile. The atmospheric refractivity profiles used for ray tracing was from the synthetic profile from Equation 5.1. In the following section, we will be looking into the results and analysis using the Radiosonde data-sets for atmospheric refractivity profiling.

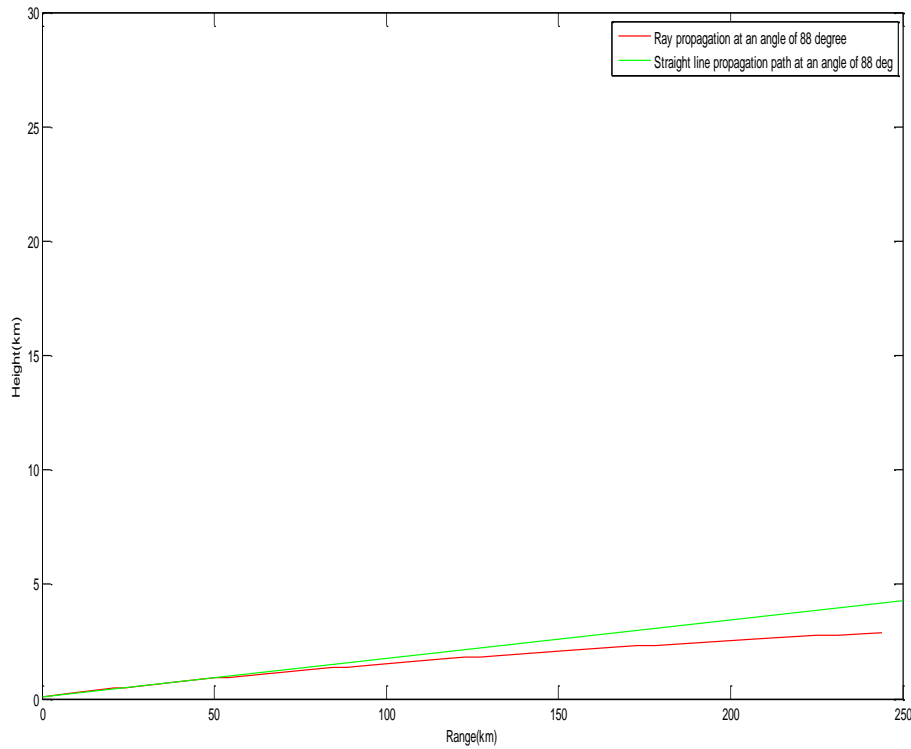


Figure 5-6: Ray path comparison with a straight line path for a ray shot at an angle of 88 degree, as it propagates through the medium. (Source height: 0.1 km, Total range = 250 km, Max height = 30 km, Initial angle = 88 deg, final angle = 88 deg, step size = 0.05).

Figure 5-7 gives a typical example of the profile obtained from Radiosonde data-set for the location Aberporth, UK. We can see from Figure 5-6, the difference in the variation between the ray traced path(red) and the ray path with no refractive medium(green). Figure 5-6 shows the comparison of a single ray propagation in environment with and without refractivity variation. The following parameters were used to obtain the results shown in Figure 5-6. The ray was shot at an angle of 88 degree. The height of the receiver = 0.1 km, maximum height of ray path = 30 km , maximum range = 250 km and the step size was fixed = 0.05 km.

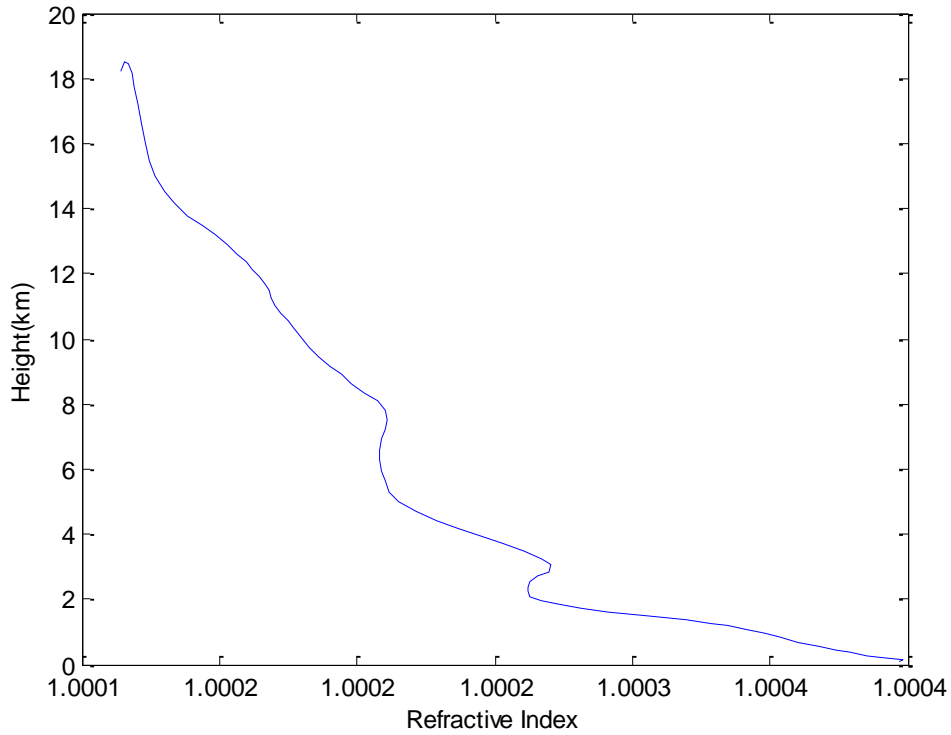


Figure 5-7: A plot showing a vertical refractivity profile using the UK BADC Radiosonde data-set(Variation of refractive index(n) with height(m)).

Figure 5-8, shows the two rays traverse through the medium with varying refractivity conditions. The variations of refractivity ‘ N ’ against height ‘ m ’, that is the refractivity environment is obtained from the Radiosonde data. The conditions for the results show in Figure 5-8 were set as follows: source height: 0.1

km, total range = 250 km, max height = 30 km, initial angle = 78.5 deg, final angle = 79 deg, step size = 0.05m and the increment angle were set at 0.5 degree. Figure 5-9, gives an illustration for the fan of multiple rays propagating through

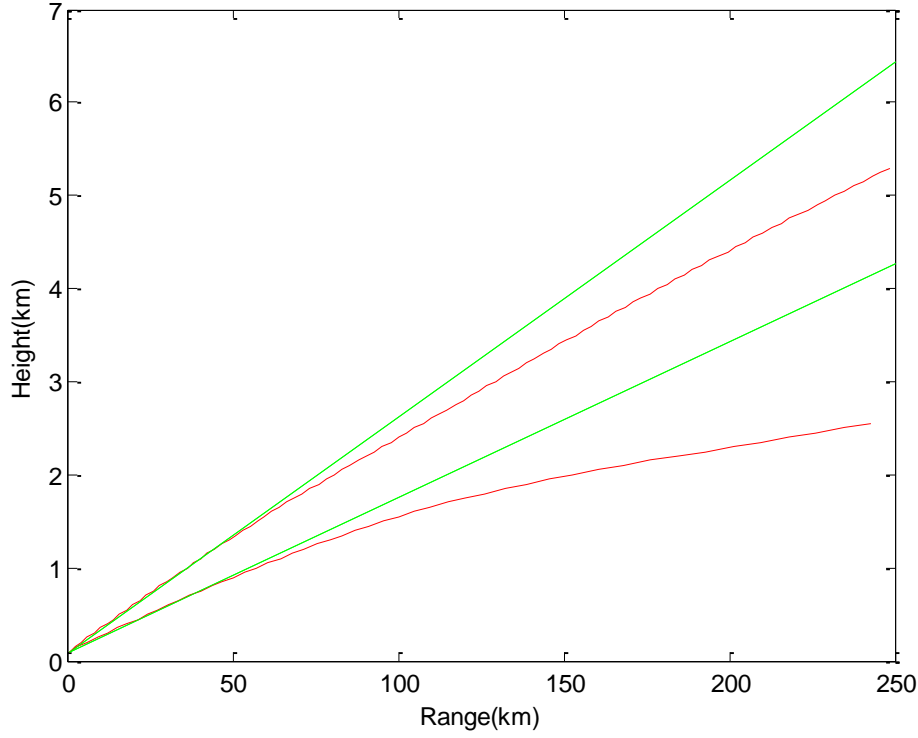


Figure 5-8: *Another example of a two ray traced signals using the radiosonde data set through an environment with varying refractivity, where green line represents straight line propagation with no refractivity and red line represents shows bending due to refractivity*

the atmosphere with an initial angle of 70 degree to the final angle of 88.5 degree. As explained and mentioned in Chapter 4, we have employed the method of ray shooting brute force method for all the simulations and results shown. Here in this technique, we shoot a fan of rays from a fixed transmitter source point as shown in the Figure 5-5, till the ray reaches the desired fixed receiver target. In the following examples, we will discuss and show the results of ray/signal reaching the receiver target. Also we will be looking to find at what angle did the ray reach or hits the receiver target specified at a certain height and determine the path delay over the ray traced path.

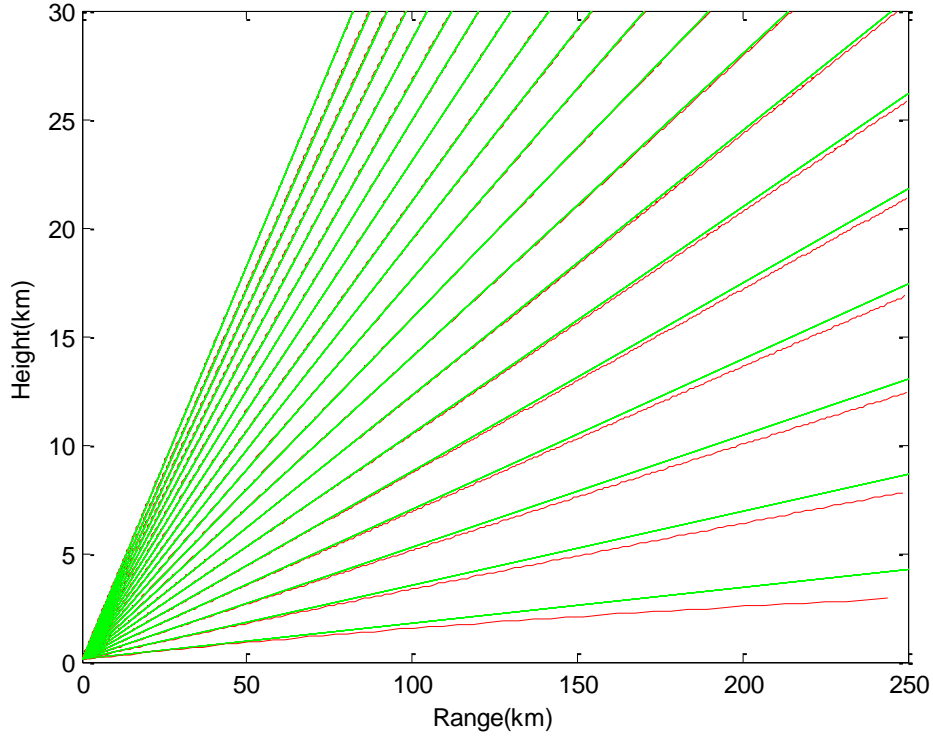


Figure 5-9: A fan of rays propagating through the environment with varying refractivity conditions, where the green line indicates a straight line path and red line indicates ray traced path.

In the following section, we will get into the analysis and results obtained by incorporating the terrain data using Shuttle Radar Topography Mission (SRTM) into the ray tracing system. The idea behind the introduction of SRTM data into the ray tracing model was to understand its effect on the variation in the refractive profile along a certain path with variation in terrain height. The SRTM data here was incorporated along with the refractive profile obtained from the Radiosonde data. This was done by shifting/incrementing the profile with the chosen ray tracing step size, which means for example, each of the field points was incremented based on the terrain height at that point. This process will in turn introduce an increased variation in the refractivity changes in the profile and thereby also the delay. In the following results, we will look into ray tracing simulation results obtained using SRTM data for different sets of fixed transmitter and receiver locations.

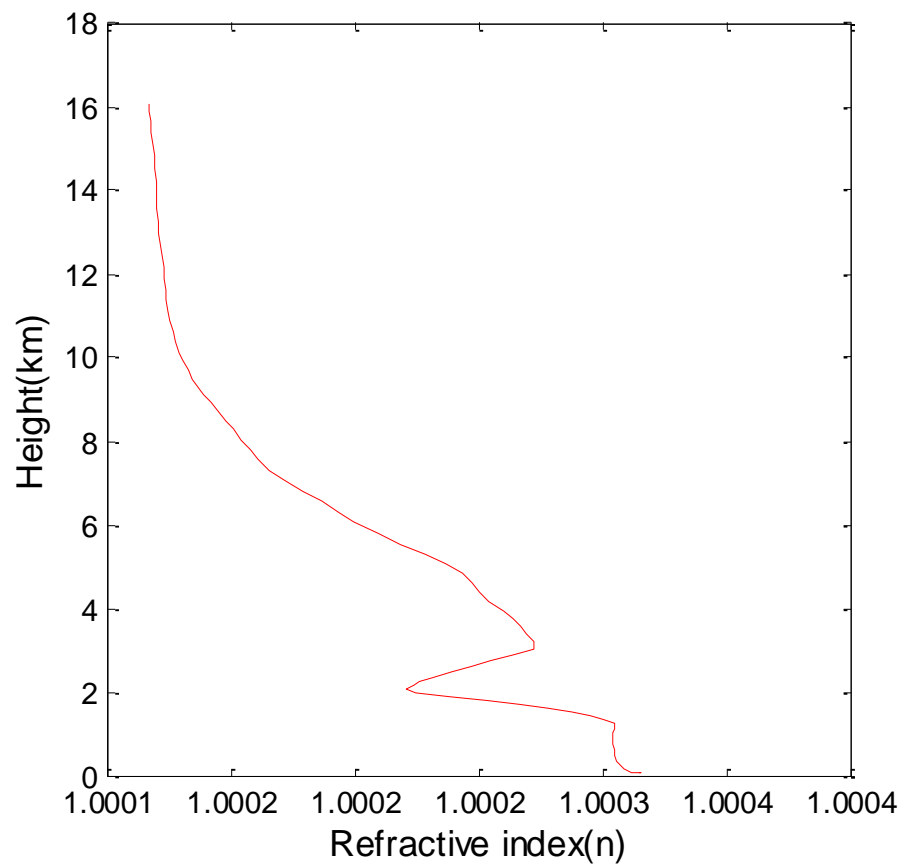


Figure 5-10: *Illustration of the refractive index profile for the simulation results shown in the following figure and refractivity profile was created using the radiosonde data.*

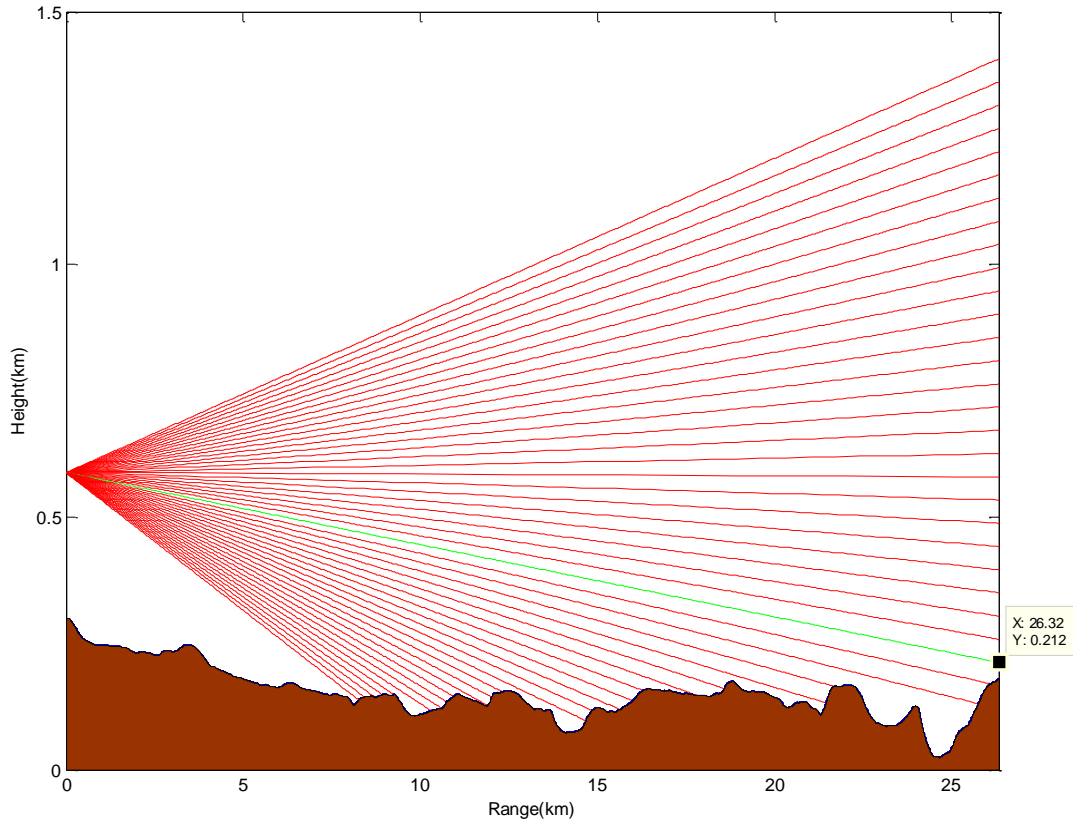


Figure 5-11: *An Illustration of a fan of signals ray traced for a specific location from Bath to Mendip through the model of an atmosphere with refractivity conditions obtained using the radiosonde data set.*

Figure 5-11, shows a typical example of a fan of ray propagating through an environment of refractivity profile variation along with SRTM terrain data. The refractive profile propagating medium used for this simulation is as shown in the Figure 5-10. The SRTM data path and ray tracing simulations for this example was chosen between Bath and Mendip. As can be seen from Figure 5-11, a fan of rays is shot from the fixed transmitter source (Bath) in the direction of the fixed receiver target (Mendip). The following parameters were used to obtained Figure 5-11, height of the transmitter = 588m, receiver height = 185m, maximum height = 5 km, max range = 26.32 km, initial angle = 89 degrees, final angle =

91 degrees, and the ray increment step size = 10cm. The red line/rays shown in the Figure 5-11 are the ones that missed the receiver target.

The green line indicates the ray reaching the desired target point which was the fixed receiver target at 185m. The final ray shooting angle obtained for the ray reaching the target was at 90.675 degree. The excess delay was then calculated as detailed in Chapter 4, from using Equation 4.11.

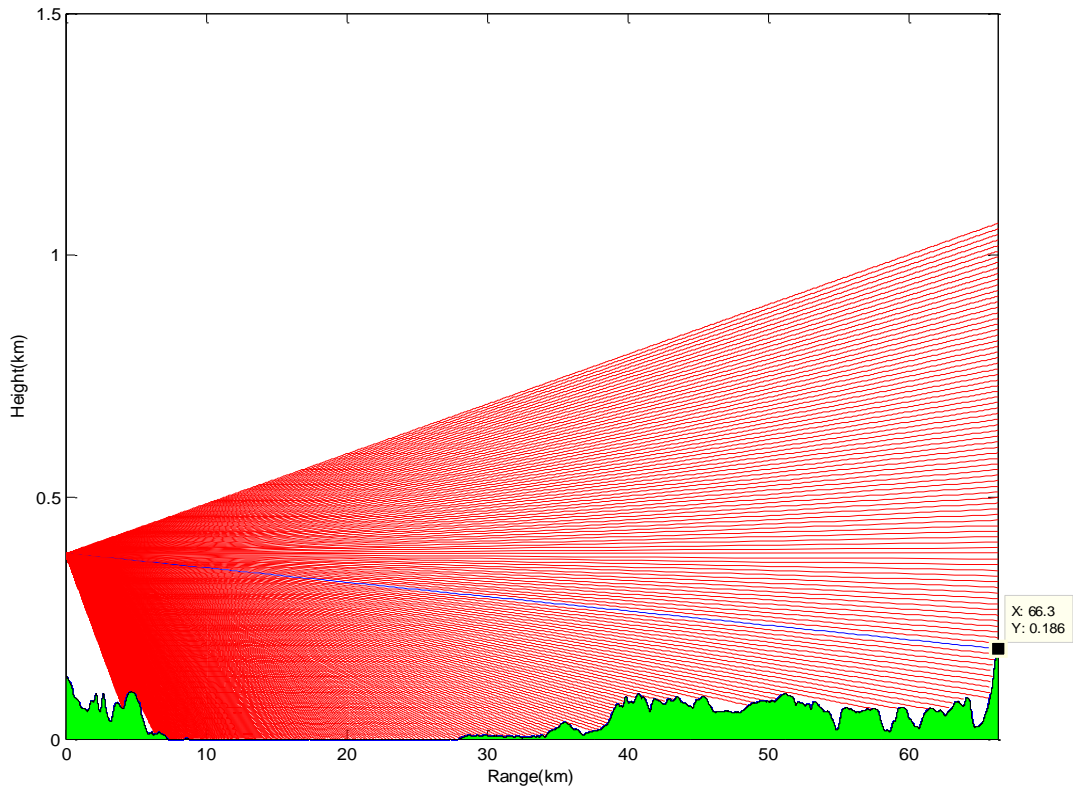


Figure 5-12: *An Illustration of a fan of signals ray traced for a specific location from Bath to Wenvoe through the model of an atmosphere with refractivity conditions obtained using the radiosonde data set.*

Figure 5-12 is another example showing the ray propagation path through a refractive environment. The refractive profile used for this example is as shown in Figure 5-10. The propagation path chosen here was taken between Bath and Wenvoe. The maximum range of the propagation path and the maximum height was set at 66.3 km and 5 km respectively. The height of the transmitter and the receiver was set at 188m and 383m, respectively. The step size was set at 10 cm. As can be clearly seen from the figure below, the ray(blue) hits the receiver target and the other rays(red) don't reach the desired receiver target. The ray shooting angle for the ray (blue) line was at 90.29 degree. The excess delay was calculated and was found to be $\delta(S) = 21.767\text{m}$ using the Equation 4.11 as detailed in Chapter 4.

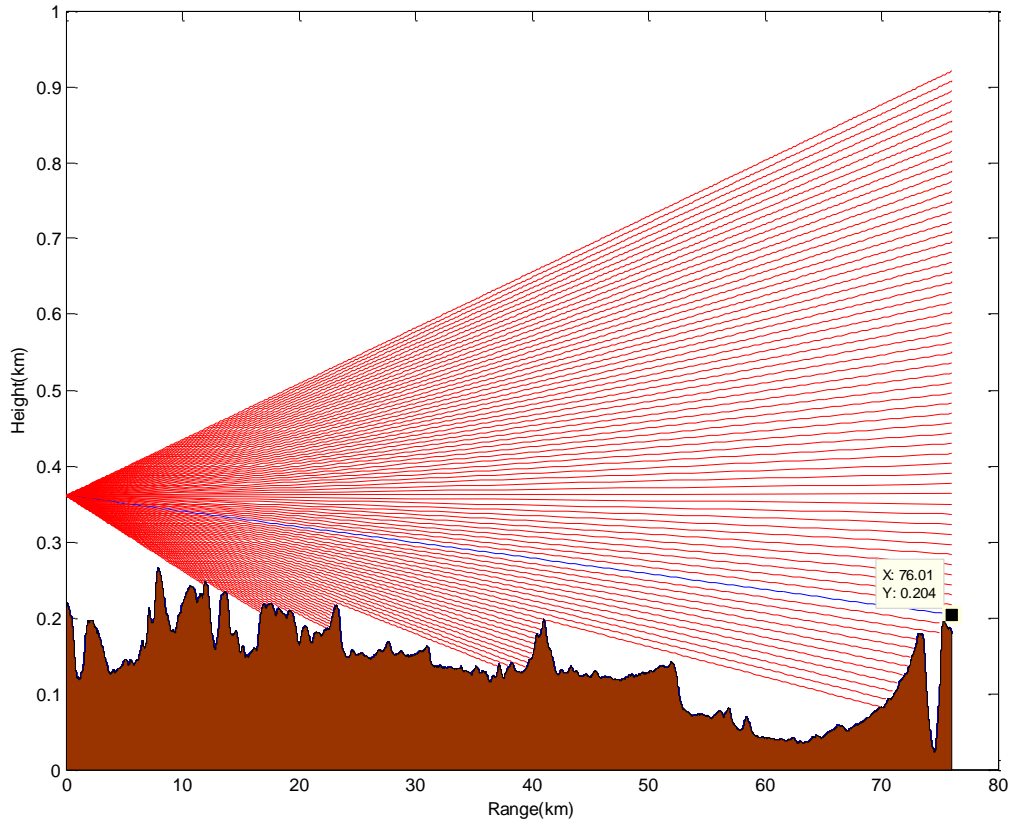


Figure 5-13: *An Illustration of a fan of signals ray traced for a specific location from Bath to Hannington/Ray propagation path from Bath to Hannington.*

Here shown in Figure 5-13, is another example of the ray propagation between the locations of Bath and Hannington. The refractive profile used in this example is similar to the Figure 5-10. The parameters chosen for the ray tracing simulations are as follows: transmitter height = 361m, receiver height = 188m, Maximum total range for propagation $\delta(S)$ = 76.01 km, maximum height = 2 km, step size = 10cm. The excess delay obtained from the ray tracing simulations was = 24.98 and the ray angle was 90.988 degree. The blue line in the Figure 5-13 indicates the ray reaching the desired target and the all other red lines indicate the ray not reaching the desired receiver target.

A case arises when we have no ray/signal reaching the receiver target. This might be due to a ray missing the target by a few cm to mm depending on the step size. In such cases we may not have a solution at all and hence no delay can be obtained. Having fewer rays at larger step angles, the probability of the ray missing the target is very likely and hence we have a situation where we might not have a solution after ray tracing. This was overcome by choosing a smaller step change of 0.0001 km degree and smaller ray step size of 0.001 km.

The drawback of using smaller step size and smaller step angle is the increased computation time. Another way of overcoming this problem was to use approximation/averaging method between the high and low of the rays closest to the desired target. This would mean if you shoot even at a higher step size there is always a solution at expense of a negligible error. Although having a solution doesn't necessarily mean better and accurate results. Provided a reasonable step angle, reasonable ray step size and approximation/averaging it is possible to get a result with almost no change/negligible change in the excess delay obtained. This will be explained in detail in the following par using the Table 5.1. Hence, here we have a trade off between choosing the right step size and the step-angle to get a desired result.

Table 5.1 shows the ray tracing results obtained based on the different combination of the ray step size, ray angle and the ray receiver height. From Table 5.1, we look into understanding the variation of the ray/signal path propagation using different factors/parameters such as ray step size and the ray angle on the final receiver target of the ray/signal. The aim here is to understand and analyse the ray tracing outcomes using different combinations of step size and ray

angle to see how close or far away is the ray from the actual fixed receiver target.

S.I no	Ray Angle (Degrees)	Step size(km)	Ray Range(Km)	Ray Receiver Height (Km)
1.	89.0940	0.1	70	0.5110
2.	89.0940	0.01	70	0.4210
3.	89.0940	0.001	70	0.4160
4.	89.0940	0.0001	70	0.4151
5.	89.0940	0.00001	70	0.4151

(a)

S.I no	Ray Angle (Degrees)	Step size(km)	Ray Range(Km)	Ray Receiver Height (Km)
1.	89.0662	0.1	70	0.5110
2.	89.0662	0.01	70	0.4210
3.	89.0662	0.001	70	0.4160
4.	89.0662	0.0001	70	0.4151
5.	89.0662	0.00001	70	0.4151

(b)

S.I no	Ray Angle (Degrees)	Step size(km)	Ray Range(Km)	Ray Receiver Height (Km)
1.	89.0212	0.1	70	0.6000
2.	89.0212	0.01	70	0.6000
3.	89.0212	0.001	70	0.5950
4.	89.0212	0.0001	70	0.5941
5.	89.0212	0.00001	70	0.5941

(c)

Table 5.1: Analysis and comparison between the different combination of ray angle, range and the step size.

This analysis will help us to determine and find the right combination of step size and ray step angle for the ray tracing simulation to get to the desired output(target). Since, having smaller and smaller step size with smaller step angles with significantly increase the process of computation time thereby slowing down the whole simulation process. Shown in Table(a),(b)and (c), we have a chosen an example of a ray angle, for instance in Table 5.1(a), the ray angle is fixed at 89.0662 and the step size is varied along with a results of the ray reaching the ray receiver height(target) for different step sizes. The receiver were fixed for

Table 5.1(a) at 0.415 km, Table 5.1(b) at 0.415 km and Table 5.1(c) at 0.594 km respectively.

It can be seen from the Table 5.1, the ray's reaching the receiver target with the step size at 0.001 km and for the ray step size above 0.001 is negligible and almost no change with the ray's distance from the final target. The ray receiver height targets with the step sizes 0.001 km, 0.0001 km and 0.00001 km does not vary significantly from the final targets as mentioned above. This can be seen for all the tables (a),(b) & (c) in Table 5.1. Hence for most of most of the simulations in the this chapter we have chosen to use the step size for the ray propagation as 0.001 km as the limit.

5.3 Statistical Analysis of the Ray-traced Delay

Understanding the variability of the tropospheric refractivity is critical to the prediction of the radio wave or signal through the atmosphere. Here, in the following section, we perform the statistical analysis of the refractivity and therefore also estimate the delay. The statistical analysis of the variability in the atmospheric refractivity will further give an insight into effects of refractivity on signal propagation through this environment. The aim of the statistical analysis of the refractivity and ray traced delay is to understand and investigate whether there is relationship between the refractivity and ray traced signal delay. We also look into analysis of the ray traced delays based on the different factors such as the season, time of the day and the height.

Figure 5-14 is an illustration of the statistical analysis of the refractivity variations over a year (2008) at Aberporth. The radiosonde data profiles was used for the analysis due to the consistent availability of data over the years and over different locations. As can be seen from Figure 5-14 it consists of three different plots. The topmost subplot(1) shown in Figure 5-14 is the number of profile available on a monthly basis which was used in this analysis. The subplot(2) shown in the middle in Figure 5-14 gives the variation of mean averaged refractivity versus the height. And finally the bottom subplot(3) is the standard deviation plot of the mean averaged refractivity. As can be seen from the subplot(2), the mean refractivity varies accordingly with the different times of the year. For example, the highest refractivity observed from the Figure 5-14 was in the month of Au-

gust. We also notice that the refractivity varies with height significantly during the summer months in comparison to the rest of the year. During the months of winter the refractivity variations with height is very low. For the remainder of the months, variation in refractivity exist but very low in comparison with the summer time variations.

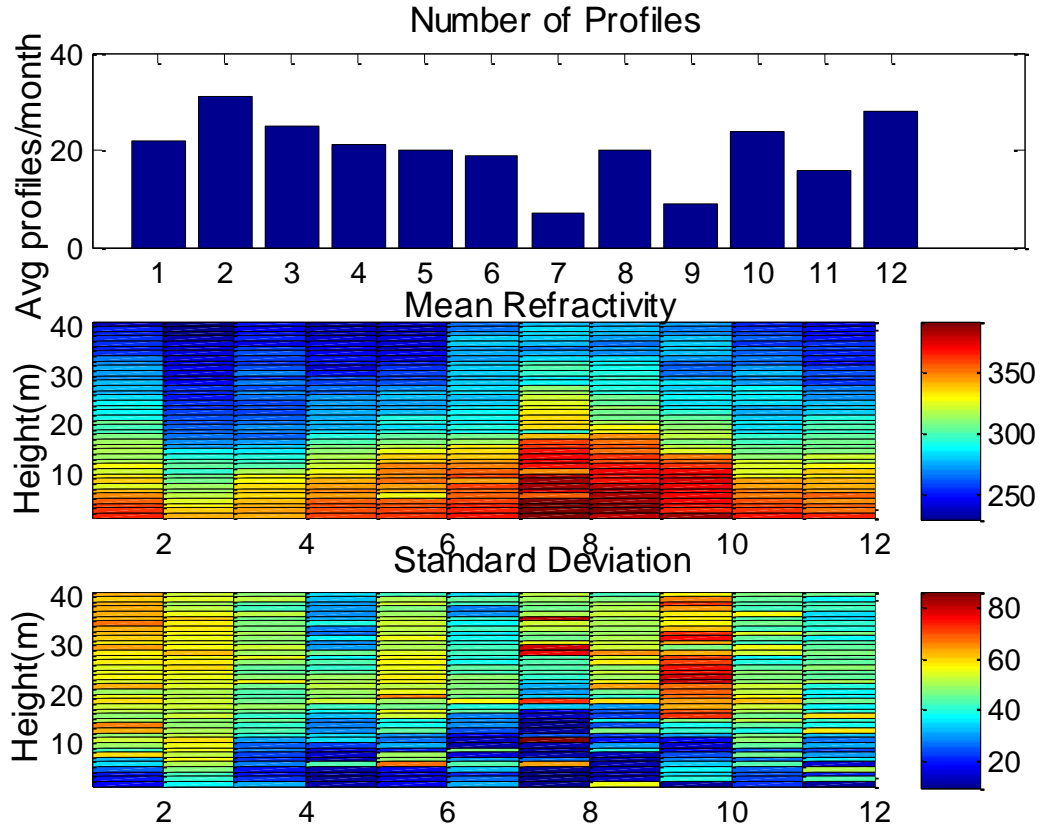


Figure 5-14: Statistical analysis of the atmospheric refractivity at Aberporth over the months for year 2008.

5.4 Delay as a Function of Season

One of the aims of performing the statistical analysis was to understand the relationship between atmospheric refractivity and the path delays. Shown in Figure 5-15 is the mean averaged path delay variations on a monthly basis shown over different years. The radiosonde dataset from Aberporth was used for this analysis. The path delay was obtained from the ray tracing simulations.

We can see from the Figure 5-15 that the path delays seems to have major peaks during the summer months. This is very much similar to what we obtained in Figure 5-14, where the refractivity was higher during the summer months from July to September. The path delay across all the year seems to show a consistent rise in path delay during summer months. During the winter months the path delays seems to be very low. The path delay have highest value of delay during the months of July and August. Hence we can say that the path delay is directly related to the seasonal variation of the refractivity.

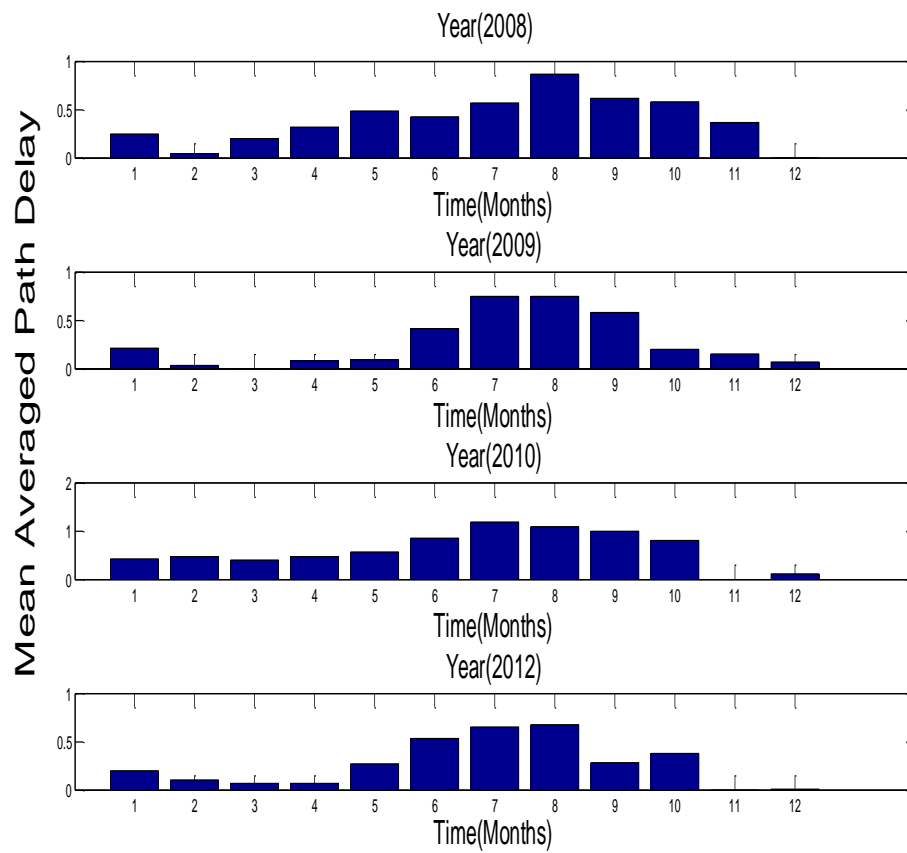


Figure 5-15: Variation of monthly path delay over different years at Aberporth.

5.5 Delay as a Function of Distance

Figure 5-16, shows how the path delay varies with different range over the year 2012. The x-axis represents the months and y-axis represents normalised averaged delay. The path delay variation over different does not show any significant increase in the delay. The change or increase in the range of signal propagation does not give significant delays. In other words, the signal delay variations comparison between the top two subplots(i.e. signal propagation range with 20 km and 15 km) as shown in the Figure 5-16, apart from the path delay changes that can be seen due to the difference in the propagation range. The path delay change for some months are also visible with difference in the peak spikes.

In case of monthly peak comparison, during the month of January for 20 km range, the peak observed is higher in comparison to the 10 km & 15 km range. This in turn could be due to larger variation the signal encounters over larger distances and in the excess few kilometres. This can be seen again in the months of August, September and October, where the signal with larger propagation distance encounters larger refractivity variations and thereby contributing to excess signal propagation path. To further understand the variation and relationship between the signal path delay and the atmospheric refractivity, we perform statistical moving average analysis in the following results/plots.

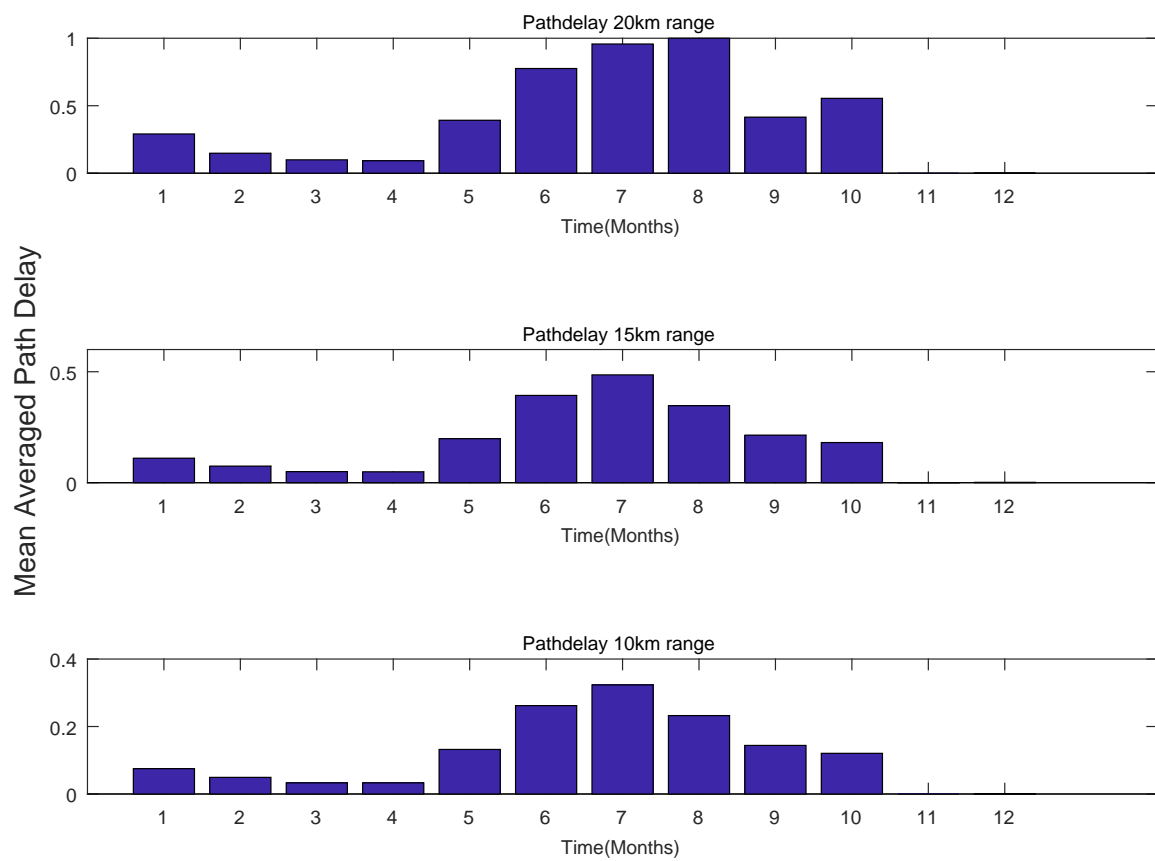


Figure 5-16: Comparison of monthly mean averaged path delay against time(Months) using different ranges(10 km, 15 km & 20 km) for the year 2012 at Aberporth.

5.6 Path Delay Analysis using Moving Average

5.6.1 Delay as a Function of the Day

In the Figure 5-16, the results obtained showed varied spikes on monthly analysis of the path delay on different ranges. Shown in Figure 5-17 is an Illustration of the moving average path delay analysis over a number of different ranges. The idea behind using moving average was to remove/average out the noise and to obtain a smoother results to observe clear sharp variations. Shown at the top subplot(1) of Figure 5-17 is the mean averaged refractivity variation with height over a number of days. The rest of the subplots shown in Figure 5-17, gives the results of the moving average analysis of the path delay versus the number of days for different ranges. The ranges chosen were 5 km , 10 km , 15 km & 20 Km respectively.

Figure 5-17 shows the path delay changes due to variation in the refractivity. In Figure 5-17, at approximately around the 50th day, which is mean averaged over 9 days, there is not much refractivity changes and hence sharp decrease in the path delay and this can be observed from Figure 5-17. In this analysis, we also find that in the subplot(4) and subplot(5), we have a small decrease(dip) in the path delay curve at roughly around the days from 125 to 130 approximately which can be observed from the Figure 5-17. These variation in the path delay are also visible in subplots (2) and (3) of the Figure 5-17, but they are much smaller in comparison to the results obtained for range 5 km and 10 km.

To summarize, here for the shorter/smaller range averaged path delay is very much relative to the mean averaged refractivity. The smaller range path delay tends to show smaller variations very well. Whilst, the path delays obtained from larger distance coverages seems to show variations on certain days, but it does not show smaller refractivity variations at lower refractivity cases. This can be seen between the days 100 and 150 on all the results shown in Figure 5-17. In particular, we can clearly see the differences between the results obtained from 5 km and 10 km range moving average path delay versus the 20 km and 15 km range moving average path delay over the days between 100 and 150.

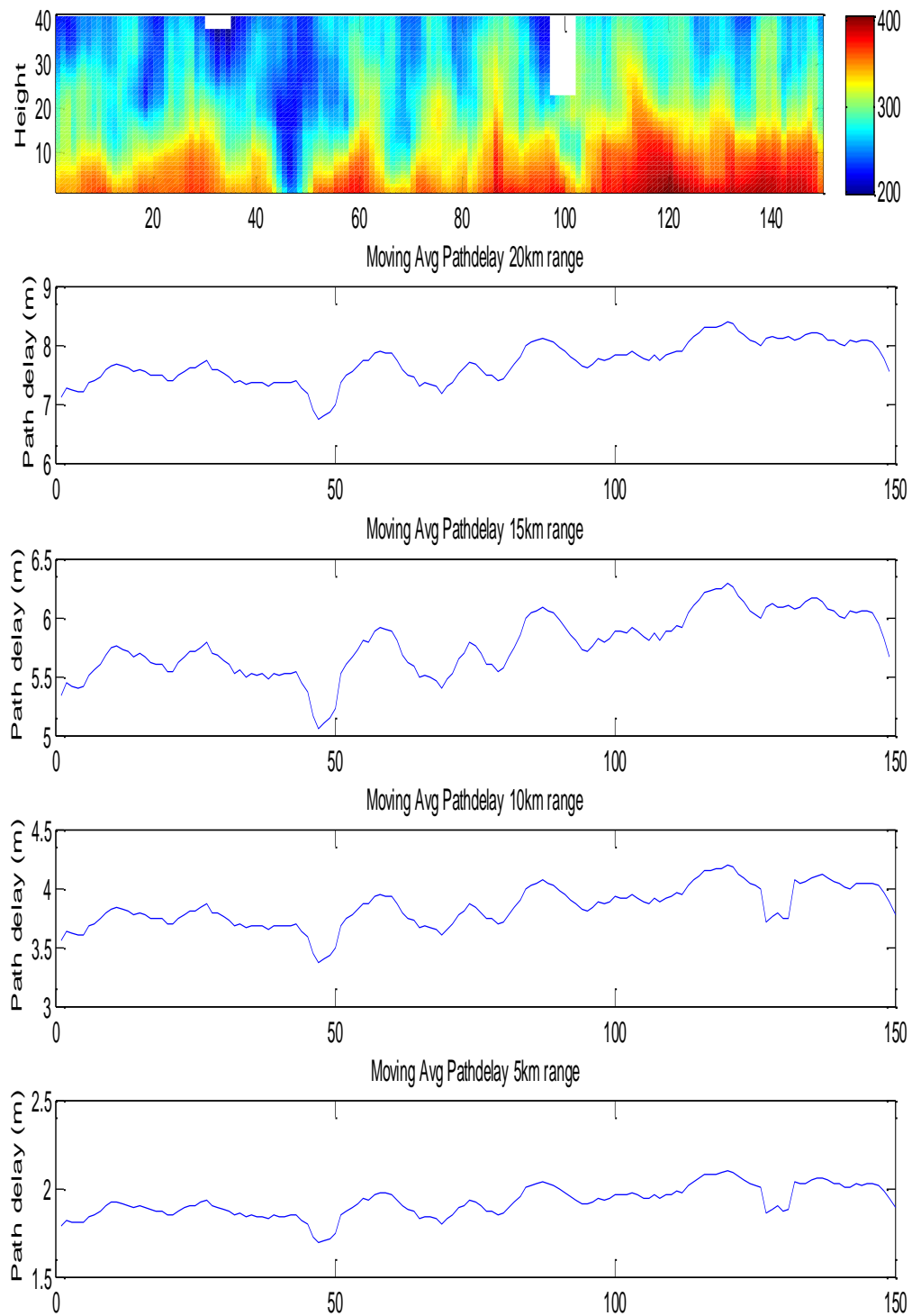


Figure 5-17: Variation of path delay analysis with respect to the mean refractivity for the year 2010 at Aberporth, over different ranges based on number of days.

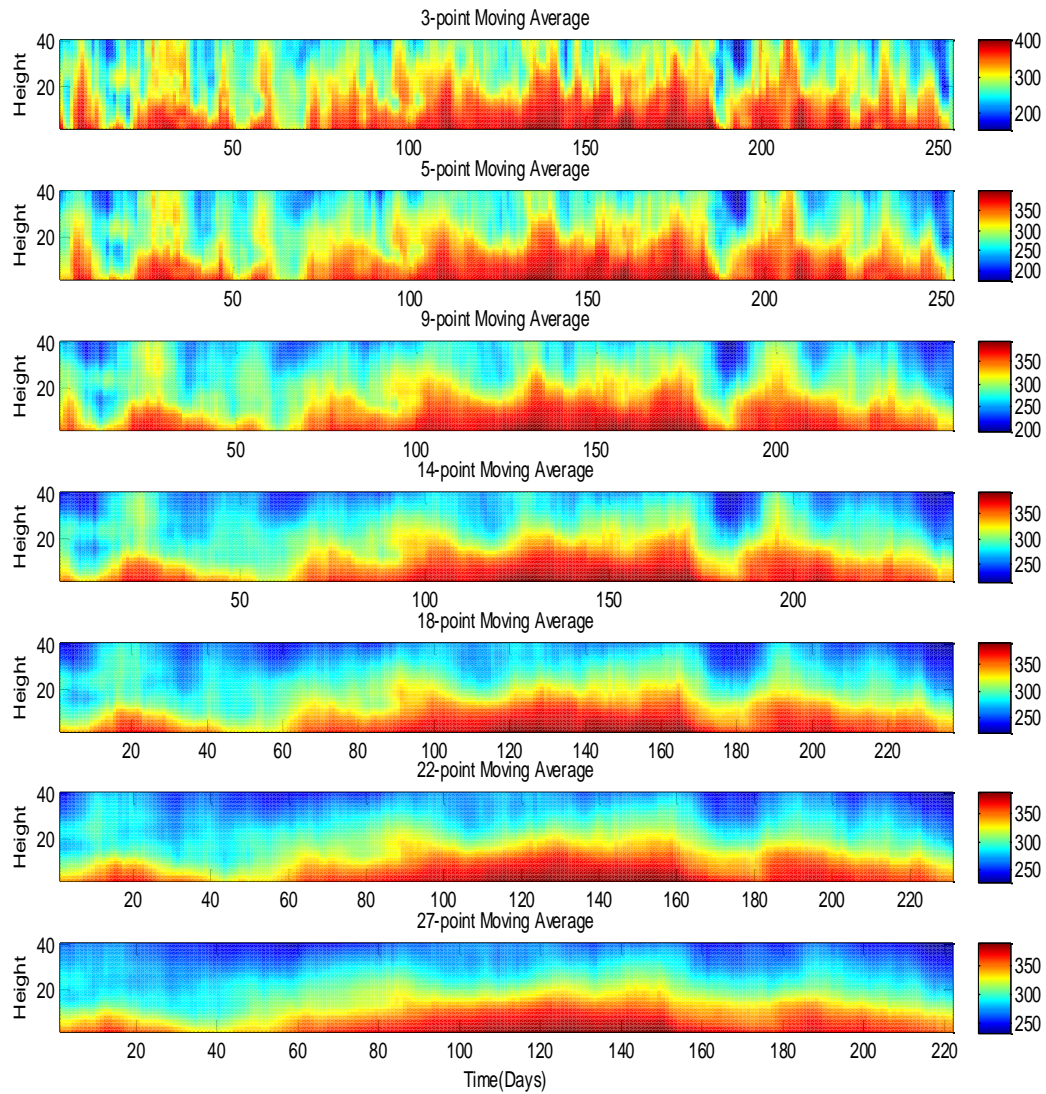


Figure 5-18: Illustration of mean averaged daily refractivity through the use of moving averages.

Here we have another example of using moving average to show the variability of refractivity on different schemes/point of moving average. Here we show the moving average refractivity plot for averaged/point/number of days against the height. For instance the top plot shown in Figure 5-18 was averaged over 3 days blocks of data for the whole year. This was done to overcome and remove noise from the data and to smooth the results obtained. We can observe from Figure 5-18 that the refractivity variability is higher over the summer months on all the plots. As we move from '3-point' to '9 point' or '14 point', the sharp peaks disappear clearly showing a higher variability during the summer.

5.7 Summary

In summary, this chapter we show and analyse the delay effects of the signal propagation through the troposphere. Ray tracing simulation delays obtained from modelling are analysed and shown for different conditions. Results of the statistical analysis of ray traced delays are also shown in this chapter. Furthermore, a detailed results and analysis of the variation of delay over different times of the year, distance, season was done. Further analysis of the delay variation was performed using the moving averaged data analysis. In the following chapter, we move into the next phase of this research study. Here we will be applying tomographic approaches for validating and analysing the delay obtained from ray tracing modelling.

CHAPTER 6

TOMOGRAPHY INVERSION

This chapter aims to use the path delay obtained from the ray tracing modelling in Chapter 4 to retrieve the original refractivity field. This task was done by using the inversion tomography technique.

This chapter begins with the introduction and background to the tomography approach. We look into the refractivity profile generator model for the refractivity profile to be used in this study. This Chapter then introduces the process of obtaining the basis function along with principal component analysis methodology which is required for the tomography reconstruction process.

Further, we go through the details of the tomography reconstruction algorithm used in this research study. Finally we analyse the results obtained using the inversion technique. Further we show the results of error analysis to demonstrate how closely the reconstructed refractivity field closely matches the original refractivity field.

6.1 Introduction to Tomographic Approach

In Chapter 2 we presented the literature work and several approaches current used for the estimation of atmospheric refractivity using different remote sensing instruments. In this Chapter, we will discuss a novel approach for the extraction of refractivity fields using the radio-wave signals/path length links.

The approach here uses a large number of links over an area to estimate the refractivity field. Here we use a tomography inversion modelling technique for the retrieval the refractivity fields. The path averaged link delays are used in the analysis. The ray traced delays were obtained using the method explained in Chapter 4. The principle behind using the inverse approach is to determine the unknown parameter from the measured quantities. The principle behind using tomography inversion is to find a meaningful solution and therefore validate the measured data based on the information available and the model.

The inversion methodology has been used previously such as in [40]. The study used microwave terrestrial links for the estimation of the rainfall fields [40]. There have been similar work performed in the past using the links to estimate rainfall rate. The first work on the use of a large array of links for rainfall estimation was conducted by [46] [47]. Figure 6-1 shows a simple illustration of an inversion problem methodology.

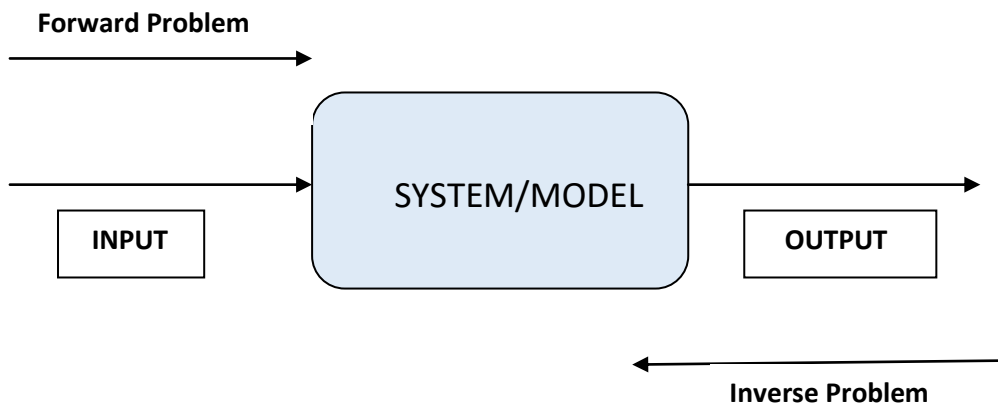


Figure 6-1: *A simple representation of the Inversion process.*

Tomography has been extensively used for many engineering, scientific tasks and medical imaging application. Tomographic technique has also been used in the past for retrieval of troposphere parameters. Previously, tomographic methodology has been used to retrieve atmospheric meteorological parameter for atmospheric profiling through using a GPS network [52]. Similar other works

have made use of the tomographic technique using GPS systems as in [53]. Variability on the temporal and spatial scales in the troposphere requires a need for the use of the application of tomographic methodology [51]. The application of tomography on Tropospheric studies using GPS was first done by [51].

6.2 Background and Procedure

The aim here is the reconstruction of the refractivity field using the ray traced link path delay. We have implemented this reconstruction by using the tomographic inversion reconstruction technique. Figure 6-2 shows the outline of the whole process from the refractivity profile to the modelled path delay and back to the refractivity profile using tomographic inversion. The first step in this process is the refractivity profile data. The data used for the process of this simulation is the five parameter model refractivity data. This refractivity data model is explained in detail in the next section.

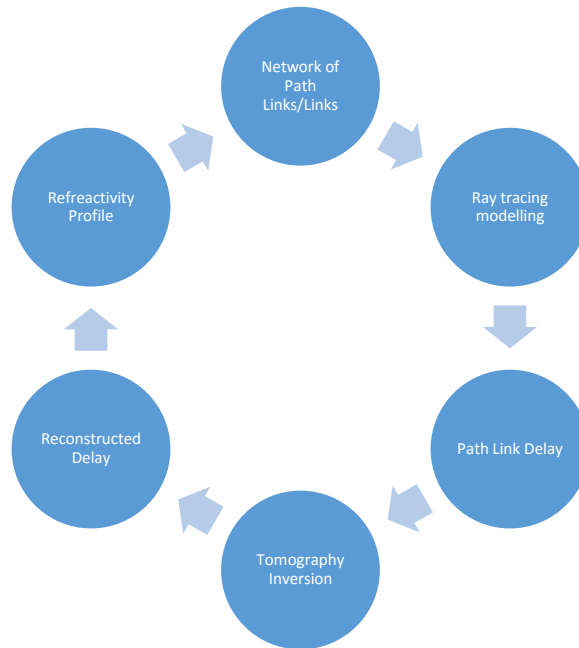


Figure 6-2: *The Process Of Tomography Inversion.*

The next step is to create a dense network of links based on a transmitter and receiver pair in a refractive atmospheric environment. Then each of these

links is ray traced to estimate the path delay through the refractivity profile. The ray tracing modelling technique used to determine the path delay is explained in Chapter 4. Once we have the ray traced delay and the path link for every pair of the transmitter and receiver pair, we apply the Tomographic inversion technique. From the path delay and the links the reconstruction can be performed which should return the refractivity field from the delay.

6.3 Refractivity Profile Generator Model

The refractivity profiles used in the process of the forward modelling and ray tracing delay was obtained using the five parameter model. The model for generating refractivity profiles was adapted from [57]. The reason for choosing this model is due to the requirement of large number of profiles and the data was generated in a quick and timely manner. The idea behind the five parameter algorithm is very similar to the the ten-parameter refractivity model developed by the Naval force Physics Laboratory and is as shown in Equation 6.1:

$$m = (\delta, c_1, z_b, z_{thick}, M_d, zb_1, zb_2, zb_3, zb_4, zb_5)^T \quad (6.1)$$

Where, ‘ δ ’ is the evaporation duct height, ‘ c_1 ’ = slope of the mixed layer, ‘ z_b ’ = trapping layer base height , ‘ z_{thick} ’ = thickness of the inversion layer and ‘ zb_1 ’ - ‘ zb_5 ’ are the base height coefficients.

The horizontal and the vertical field of the profile can be obtained through the first and the last five parameters respectively from the equation shown above in [53]. Hence the model can be used for both the cases of horizontal and vertical refractive profile generation. For the purpose of this research we have used the five parameter from the equation shown above. The table shown below gives an example of the profile generation using five parameter refractivity profile model. The table shown below in Table 6.1 includes the range and values of all the parameters used for the refractivity profile generation.

The variation of the modified refractivity with height(z) obtained from the model

Variable	From	To	Step size/Intermediate Values
c_1	-0.7	0.4	-0.4, -0.1 and 0.2
M_d	0	100	20
z_b	140	500	20
z_{thick}	10	100	10

Table 6.1: Values of the parameters used for the refractivity profile generation

is as shown below from [53][54].

$$M(z) = \begin{cases} M_1 + c_0(z - \delta \log(\frac{z}{z_0})) & \text{for } z < z_d \\ c_1 z & \text{for } z_d < z < z_b \\ c_1 z_b - M_d \frac{z - z_b}{z_{thick}} & \text{for } z_b < z < z_t \\ c_1 z_b - M_d + c_2(z - z_t) & \text{for } z_t < z \end{cases} \quad (6.2)$$

where, $c_0 = 0.13$, $\delta = \text{duct height(m)}$, $c_1 = \text{mixed layer slope}$, $c_2 = 0.118 \text{ M units m}^{-1}$, $z_0 = 0.00015$, $z_b = \text{base height trapping layer}$, $z_{thick} = \text{inversion layer thickness(m)}$, $z_t = z_b + z_{thick}$, $M_0 = 330 \text{ M units}$, $M_1 = c_0 \delta \log(\frac{z_d}{z_0}) + z_d(c_1 - c_0)$, $M_d = \text{M}$, which is inversion layer deficit.

6.4 Path Integrated Refractivity Retrieval

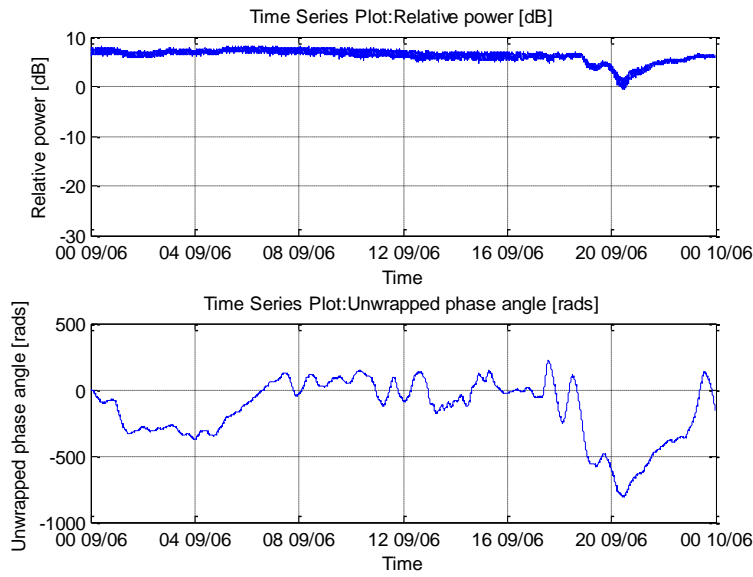
In chapter 3, we have explained about the use of broadcast signals for measuring atmospheric refractivity. The application of using DAB/DVB broadcasting signals has been previously used for atmospheric monitoring and measurements as proposed by [1]. The basic methodology used to estimate the water vapour variability between a pair of transmitter and receiver is similar to that used in

the current GPS refractivity measurement system.

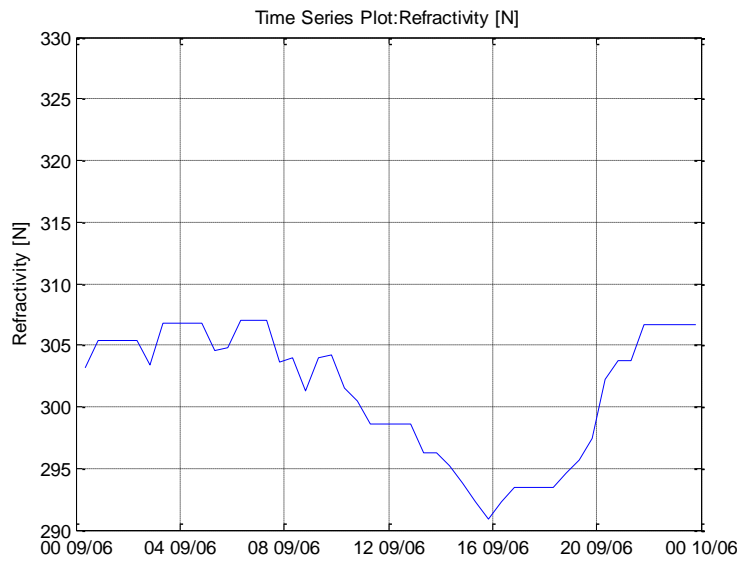
In the past there have been various methods of tomographic approaches used in the past to study the effects of refractivity [67][20] and [35]. Estimation of refractivity (water vapour density) using GPS is limited due to a number of reasons. One significant limitation is the requirement of dense network of GPS which is limited due to cost constraints to set-up a dense array of network. The other factor is the significant space-time averaging processing which makes the spatial information obtained from GPS network is fade and weak [56]. Various other types of sensor technologies are currently used to extract the water vapour density (refractivity) namely space-borne radiometers, water vapour radiometers, radiosondes and microwave radiometers. All of the current existing refractivity retrieval instruments significantly lack to measure the data on the spatial and temporal scale [56].

A number of algorithms were developed and using a very basic receiver, a link between changes atmospheric parameters and measurable path delay was established [69]. Figure 6-3 shows an example of the magnitude and phase data from the Single-site autocorrelation and the lower part shows the data recorded UK meteorological station data(Bristol airport). The phase information can be used to extract the excess delay. Using a dense network of receivers, the measured excess path delay can be used with an inverse method to retrieve refractivity fields.

In the absence of a dense network, we test the concept and tomography methodology using simulation framework. The reason for this is currently we only have DAB/DVB data collected for one path between Mendip and Bath transmitter receiver pair. The tomography technique requires a dense array of transmitter receiver network pair dataset. Further, we generate refractivity profiles using the refractivity profile generator model as explained in the previous section.



(a) Single-Site autocorrelation of 222.064MHz DAB signal recorded at University of Bath - top: magnitude and bottom: phase



(b) Meteorological Station data recorded at Bristol Airport.

Figure 6-3: *Magnitude and phase recorded at University of Bath from the nearest transmitter site Mendip using the Single-site autocorrelation of 222.064MHz DAB signal is shown in part(a). Lower part(b) shows the refractivity data from the UK meteorological station data at Bristol Airport*

6.5 Inversion Algorithm

In the absence of a deployed network of receivers we will adopt a simulation framework. For the forward model we assume a model refractivity field and use the ray-tracing approach [65] to derive delays corresponding to the integrated refractivity along the path [66]. For the actual inversion, we use a methodology adapted from [67]. Estimating the horizontal refractivity field is formalized as a problem of determining a set of orthogonal basis functions which span the refractivity field function.

The assumption being that any refractivity field can be realized from a linear combination of the basis function set. Adopting this approach only requires the determination of a smaller number of coefficients which are projections of the refractivity field onto the basis function set, rather than determination of every refractivity value associated with every volume element.

For a given network of paths, a matrix, L , can be constructed in which each element represents the path length of the i^{th} link through the j^{th} pixel. The product of the link lengths with the (unknown) refractivity values, N , yields the integrated refractivity values, γ , which are simply related via [65] to the (known) excess delays from the measurements. This can be written in matrix form as

$$LN^T = \gamma^T \quad (6.3)$$

The direct solution to this problem can be written as

$$N = [L^{-1}\gamma^T]^T \quad (6.4)$$

However, since L is sparse, the problem is very ill-conditioned. To solve this we can recast the problem. First, let us consider a set of orthogonal basis functions, F , chosen such that they span all possible refractive index fields. The problem is then reduced to finding a set of coefficients that describe the basis functions rather than one of determining refractivity in each pixel. An analogy is using a Fourier series to describe a waveform rather than sample-by-sample representation. Hence we can approximate the refractivity field N as;

$$N \approx [Fw]^T \quad (6.5)$$

The basis function weights can be obtained from the solution of $LFw \approx \gamma^T$ which can be solved as least-squares problem:

$$\min_w [||LFw - \gamma^T||_2] \quad (6.6)$$

Such a solution may be susceptible to measurement errors leading to non-physical results. Further regularisation of the inverse problem is required to filter out the influence of noise by imposing smoothness constraints on the solution. Various solutions to these problems have been proposed in the literature [71]. A well-known regularisation method is Tikhonov method modifies the minimisation to become:

$$\min_w [||LFw - \gamma^T||_2 + \lambda^2 ||w||_2^2] \quad (6.7)$$

The parameter λ controls how much weight is given to the minimisation of w relative to the minimisation of the residual norm. That is, the parameter λ strikes a balance between the reconstructed refractivity field fitting the measured link data versus the overall smoothness of the reconstructed refractivity field. Finally, having determined the weighting vector, the estimated refractivity field \hat{N} can be written as:

$$\hat{N} = [Fw]^T \quad (6.8)$$

6.6 Basis Function Using Principle Component Analysis(PCA)

The basis functions used in this reconstruction process is calculated by performing the principal component analysis (PCA) on a two-dimensional Gaussian based function. The orthogonality of the basis function greatly reduces the calculation of the weights vector(w) [40]. The term principal component is also referred to as the “Discrete Karthunen-Loeve Transform” or “The Hotelling Transform” [62].

PCA is defined as an orthogonal linear transformation that transforms a data-set to a new coordinate system such that the greatest variance by any projection of the data comes to lie on the first component, the second greatest variance on the second component and so on [61]. The data-set can be further reduced into a smaller (and orthogonal) data-set, this is be done by removing the higher order principal components. The orthogonal nature of the data-set is an important

feature which helps to achieve a unique solution to the tomographic inversion.

The reconstruction methodology is significantly dependent on the type and the number of basis function for the reconstruction of the refractivity fields. The number of basis function used significantly determines and defines the details within the reconstruction field. There have been different approaches used in the past to calculate basis function such as data derived approach and the analytical approach as discussed in [40].

6.6.1 Gaussian Basis Function

We have in our case used the analytical synthetic generated/Gaussian based basis function. The analytical function using Gaussian based function to estimate the basis function has previously been used to estimate rainfall fields [64]. A two-dimensional Gaussian function can be calculated from Equation shown below as:

$$G(x, y, \sigma) = \exp\left[\frac{-(x - x_0)^2 - (y - y_0)^2}{2\sigma^2}\right] \quad (6.9)$$

Where, ' x_0 ' and ' y_0 ' Represents the centre of the function and ' σ ' = width. For simplicity here in this case, the entire matrix will be represented by an array and used as $G'(x_0, y_0, \phi)$ to represent matrix ' G ' and this will be calculated from the values of ' x_0 ', ' y_0 ', and ' σ '.

$$\phi = \left\{ \sigma_1 = n; \sigma_{i+1} = \left[\frac{\sigma_i}{2}\right]; \sigma_{i+1} \geq \sigma_{min} \right\} \quad (6.10)$$

Where ' n ' = size of the reconstruction matrix and σ_{min} is the minimum size of the reconstruction matrix. ' X_0 ' and ' Y_0 ' for each value of ' ϕ ' is given by the equations shown below:

$$X_0 = \left\{ \begin{array}{l} x_0(i) = 0; \\ x_0(i + 1) = x_0(i) + \left[\frac{\sigma_i}{2}\right]; \\ x_0(i + 1) \leq n \end{array} \right\} \quad (6.11)$$

$$Y_0 = \left\{ \begin{array}{l} y_0(i) = 0; \\ y_0(i+1) = y_0(i) + [\frac{\sigma_i}{2}]; \\ y_0(i+1) \leq n \end{array} \right\} \quad (6.12)$$

From the above process, we aim to create a data set with a number of fields for reconstruction. The data set is created by a decreasing scale Gaussian function and this in turn is then scanned across the entire reconstruction region to create a number of fields. The matrix ' $G'(X_0, Y_0, \phi)$ ' is typically a multi-dimensional array ($d \times n \times n$) which is then reshaped to ($n^2 \times d$) This data created then further undergoes a PCA to provide the basis function 'K'.

From the process described above we obtain a sets of Gaussian based basis function of varying sizes(size of the reconstruction field ' n ' and width ' σ_{min} '). The size of the reconstruction matrix is controlled by ' n ' and ' σ_{min} ' controls the minimum(smallest) size of the Gaussian function in the reconstruction field. The eigenvectors and the covariance matrix are estimated using the Turk and Pentland method [66].

6.6.2 Calculation of PCA Methodology

The steps used to obtain the PCA components is as shown below and this method was employed from [40]. The eigenvectors and the covariance matrix are estimated using the Turk and Pentland method[66]. The steps used in PCA process are as shown below:

1. Firstly, we compute the mean of the data-set.
2. Next in the process we calculate the vector differences from the mean averaged vector.
3. Obtain the covariance matrix.
4. Compute the eigenvectors and eigenvalues of the above covariance matrix.
5. Sorting the vectors/values according to the size of the eigenvalue. In this step the two matrix are sorted from largest to smallest according to the eigenvalue matrix. The output of this step is the matrix containing the

sorted eigenvectors and the diagonal matrix containing the corresponding eigenvalues.

6. Extract the eigenvalues of the diagonal matrix and calculate the energy content for each eigenvector.
7. Normalize vectors to unit length and finally select a subset of the eigenvectors as basis function vectors. The basis function matrix is finally defined by the largest value ' f ' of the eigenvectors and is reduced to a form of $(n \times f)$.

We have used the square based reconstruction fields throughout the analysis for simplicity [40], e.g. 20×20 pixel matrix will have the length of the column vector $n = 400$.

6.7 Tomography Reconstruction Technique

The tomography reconstruction we have used here is based on a matrix based reconstruction approach. The technique which uses the inversion methodology aims to estimate the weights of the basis function rather than directly finding the refractivity field.

Let us consider an n number of links within a matrix which is represented by $[q \times q]$. This measurement is then stored in a variable represented by T which is represented and stored in matrix form as $[r \times 1]$.

Figure 6-5 shows the steps involved in the process of the entire reconstruction inversion technique. The next step in this process is to identify each of the link/ray intersection through the matrix pixel. To give an illustration of link coverage, we have shown an example by vector sum all the links. The quality coverage indication was shown by taking the sum through all the rays. This is as shown in the Figure 6-4 which is given below and also thereby shows the quality of the path link coverage. The next step in this process is to reshape each of the ray

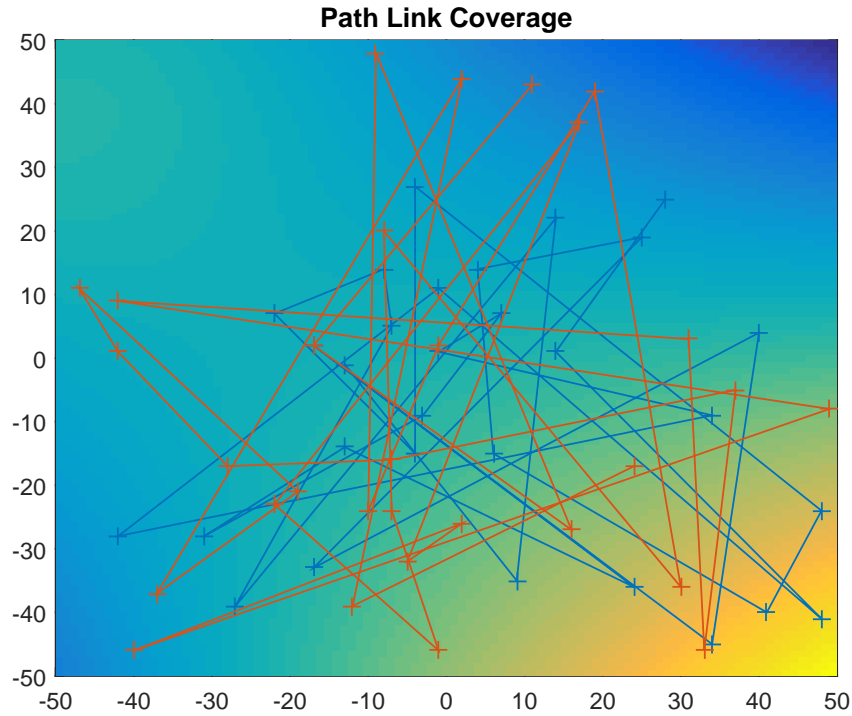


Figure 6-4: An Illustration showing the quality of the path link coverage over an area.

to the form which is represented by $[n \times q^2]$ and is denoted by R . We know introduce the basis function which is as explained in the section above and gives details about the method used to obtain the functions. A Gaussian based basis function has been used in this inversion reconstruction.

The basis function model is given by $[q^2 \times k]$. The term K here represents one basis function and is orthogonal and is stored in a matrix $[B]$. This matrix B hence contains $[q^2 \times K]$. A matrix M of the form $M = RP$ is created by placing each of the ray through each of the model vector. This matrix can be further represented to the form $n \times k$, where Path link delay, $T = MW$. Here, W represents a set of vector weights which is $[k \times 1]$ which are then applied to the model vectors and this is further solved for required measurements.

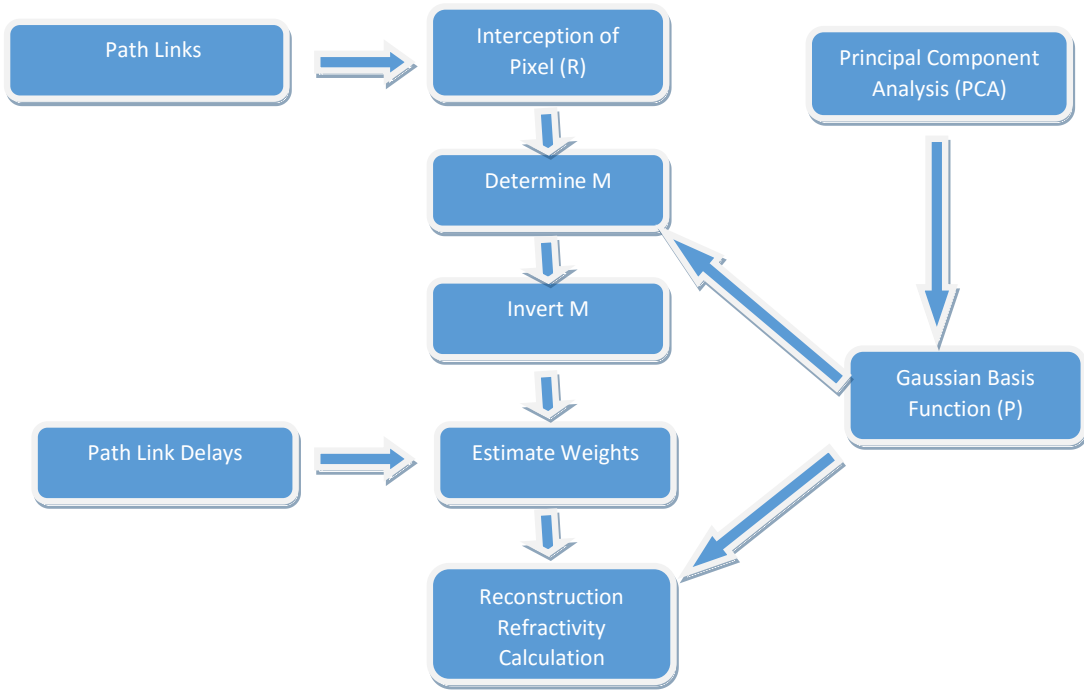


Figure 6-5: An Illustration of the steps for the overall process of the reconstruction inversion methodology.

From the above equation path link delay, $T = MW$, we can get $W = M^{-1} \times T$. Here we apply the Moore-Penrose pseudo-inverse, as M is sparse and non-square and the inverse of M cannot be obtained as it doesn't exist. The estimated matrix field, $S(q^2 \times 1)$ is further calculated and obtained by computing S which is given by $S = PW$. The reconstructed field and the original field is produced and compared and this is shown in the following figure.

The estimated matrix field, $S(q^2 \times 1)$ is further calculated and obtained from $S = PW$. The reconstructed field and the original field is produced and compared and this is as shown in Figure 6-6. Figure 6-6 also shows the linear comparison between the original and reconstructed field. The reconstruction matrix size for this case was 100×100 the number of links was 200.

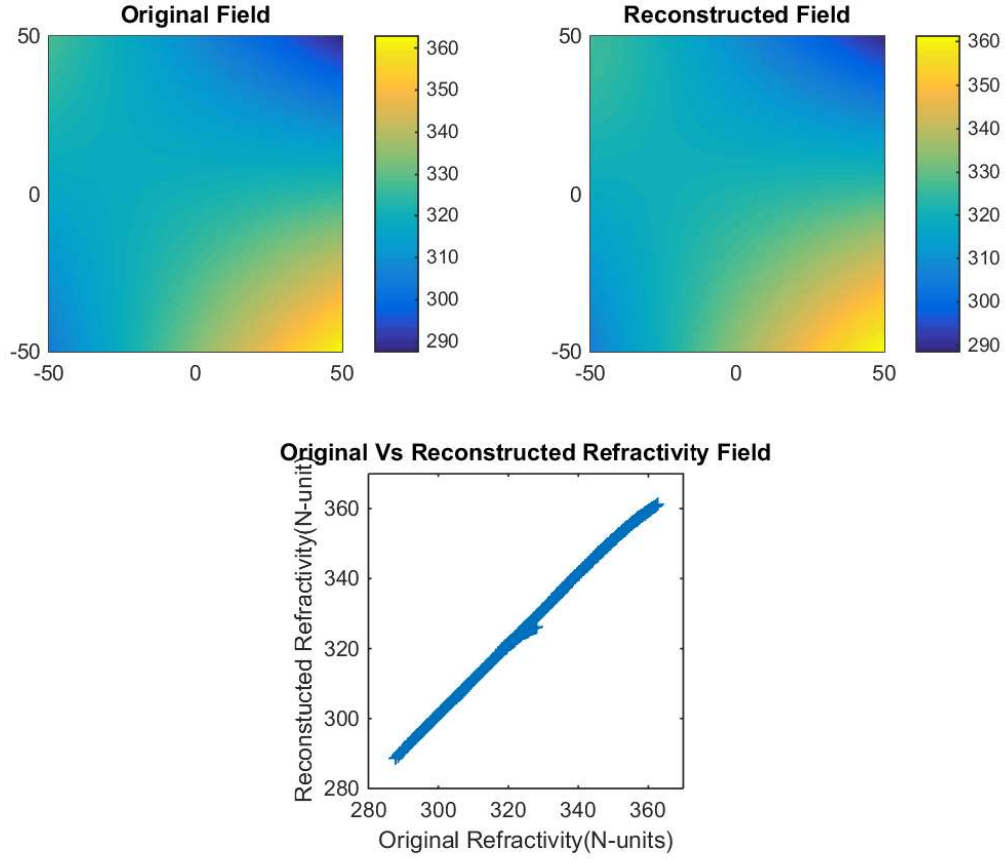


Figure 6-6: Comparison analysis between the original and the reconstructed refractivity field.

Figure 6-7 shows another example demonstrating the reconstruction of a 100×100 reconstruction area size. The number of the links used in this reconstruction illustration was fixed at 150 links. The basis function was obtained using the Gaussian based function which is shown in section above. The minimum size of the Gaussian function in the field was 20. Figure also shows the path link coverage over the reconstruction area.

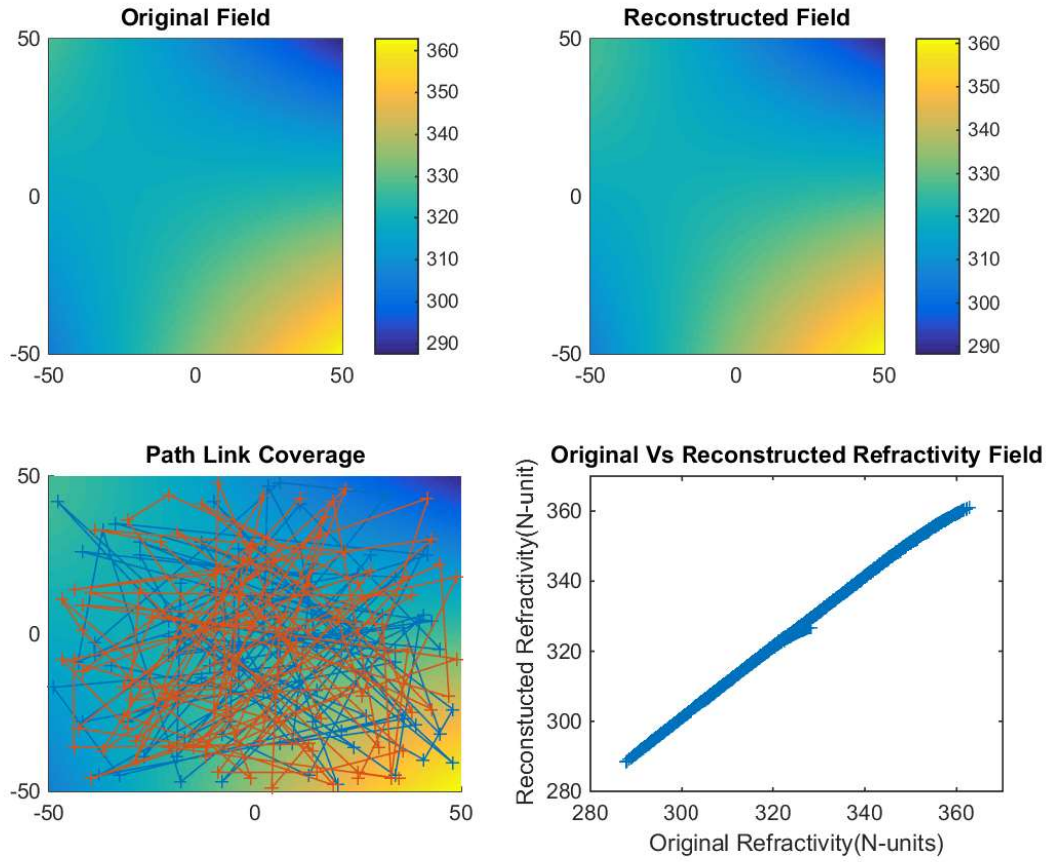


Figure 6-7: Illustration showing the comparison analysis between the original and the reconstructed refractivity field.

We will now look into the methodology with a detailed example to show different stages in the inversion process. For example, let us consider a 2×2 refractivity, with the pixel labelled as shown in the Figure 6-8. Pixels 1 and 3 in the Figure represents refractivity. There are 4 links running through this grid resulting in a measurement vector, T , and a pixel intersection matrix, R . Now we define 4 orthogonal basis functions, P such that our final field, S , is the basis

functions multiplied by a set of weights, given by $W : S = P \times W$.

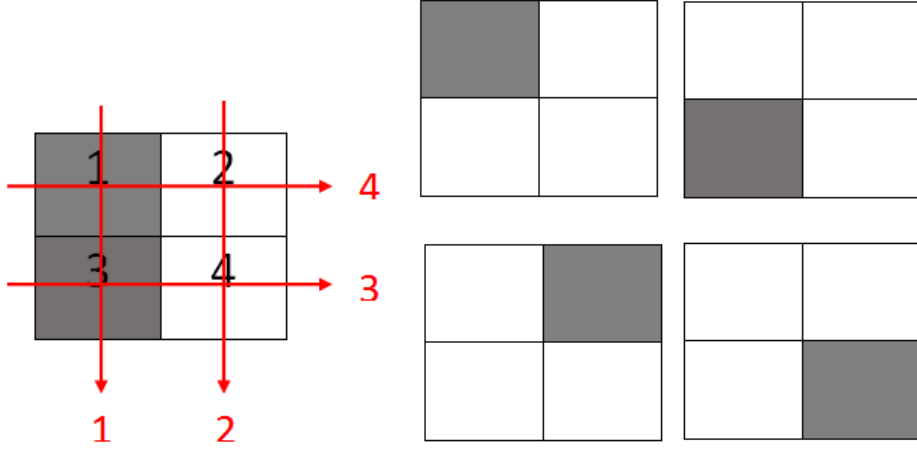


Figure 6-8: Illustration of the inversion methodology, here the left part of the Figure shows link and pixel intersection (R) & the right part of Figure represents the 4 orthogonal basis function(P)

$$T = \begin{bmatrix} 2 \\ 0 \\ 1 \\ 1 \end{bmatrix} R = \begin{bmatrix} 1 & 0 & 1 & 0 \\ 0 & 1 & 0 & 1 \\ 0 & 0 & 1 & 1 \\ 1 & 1 & 0 & 0 \end{bmatrix} P = \begin{bmatrix} 1 & 0 & 0 & 0 \\ 0 & 0 & 1 & 0 \\ 0 & 1 & 0 & 0 \\ 0 & 0 & 0 & 1 \end{bmatrix}$$

The next step is to build an array representing the link through each of the basis function, $M = R \times P$.

$$M = \begin{bmatrix} 1 & 0 & 1 & 0 \\ 0 & 1 & 0 & 1 \\ 0 & 0 & 1 & 1 \\ 1 & 1 & 0 & 0 \end{bmatrix} \times \begin{bmatrix} 1 & 0 & 0 & 0 \\ 0 & 0 & 1 & 0 \\ 0 & 1 & 0 & 0 \\ 0 & 0 & 0 & 1 \end{bmatrix} = \begin{bmatrix} 1 & 1 & 0 & 0 \\ 0 & 0 & 1 & 1 \\ 0 & 1 & 0 & 1 \\ 1 & 0 & 1 & 0 \end{bmatrix}$$

It is now apparent that our measurements $T = W \times M$ and hence $W = M^{-1} \times T$.

$$W = \begin{bmatrix} 0.375 & -0.125 & -0.125 & 0.375 \\ 0.375 & -0.125 & 0.375 & -0.125 \\ -0.125 & 0.375 & 0.125 & 0.375 \\ -0.125 & 0.375 & 0.375 & -0.125 \end{bmatrix} \times \begin{bmatrix} 2 \\ 0 \\ 1 \\ 1 \end{bmatrix} = \begin{bmatrix} 1 \\ 1 \\ 0 \\ 0 \end{bmatrix}$$

The reconstruction is then calculated, $S = P \times W$

$$S = \begin{bmatrix} 1 & 0 & 0 & 0 \\ 0 & 0 & 1 & 0 \\ 0 & 1 & 0 & 0 \\ 0 & 0 & 0 & 1 \end{bmatrix} \times \begin{bmatrix} 1 \\ 1 \\ 0 \\ 0 \end{bmatrix} = \begin{bmatrix} 1 \\ 0 \\ 1 \\ 0 \end{bmatrix}$$

6.8 Results And Error Analysis

6.8.1 Varying the Number of Basis Function

In this section we will look into the variability analysis of the reconstruction by using different size of Gaussian basis function. The different basis function which is as explained in subsection 6.4 shown, is controlled by the values ‘ n ’ and ‘ σ_{min} ’. Where, ‘ n ’ is the reconstruction matrix size and ‘ σ_{min} ’ is the smallest size Gaussian function in the field. In the following analysis, we will show the reconstruction results based on the different combination of links and by varying the size of the minimum scale of the basis functions.

Shown in the Figures 6-9 - 6-12 we can see different cases of the reconstruction results by varying the numbers of the basis function with a fixed number of links. For all Figures from 6-9 - 6-12, we have used a 100×100 pixel domain and the length of the grid was fixed at 1 km. We show here in the following Figures from 6-9 to 6-12, how by varying the right numbers of the basis function for a number of link we can obtain the reconstructed field.

As can be seen from Figures 6-9 to 6-12 by varying the number of minimum scale of the basis function(= 5, 7, 10 and 15) and with fixed number of links(=100), we aim to obtain a desired reconstruction field. Hence by using right combination of the link and number of basis function we extract the refractivity field.

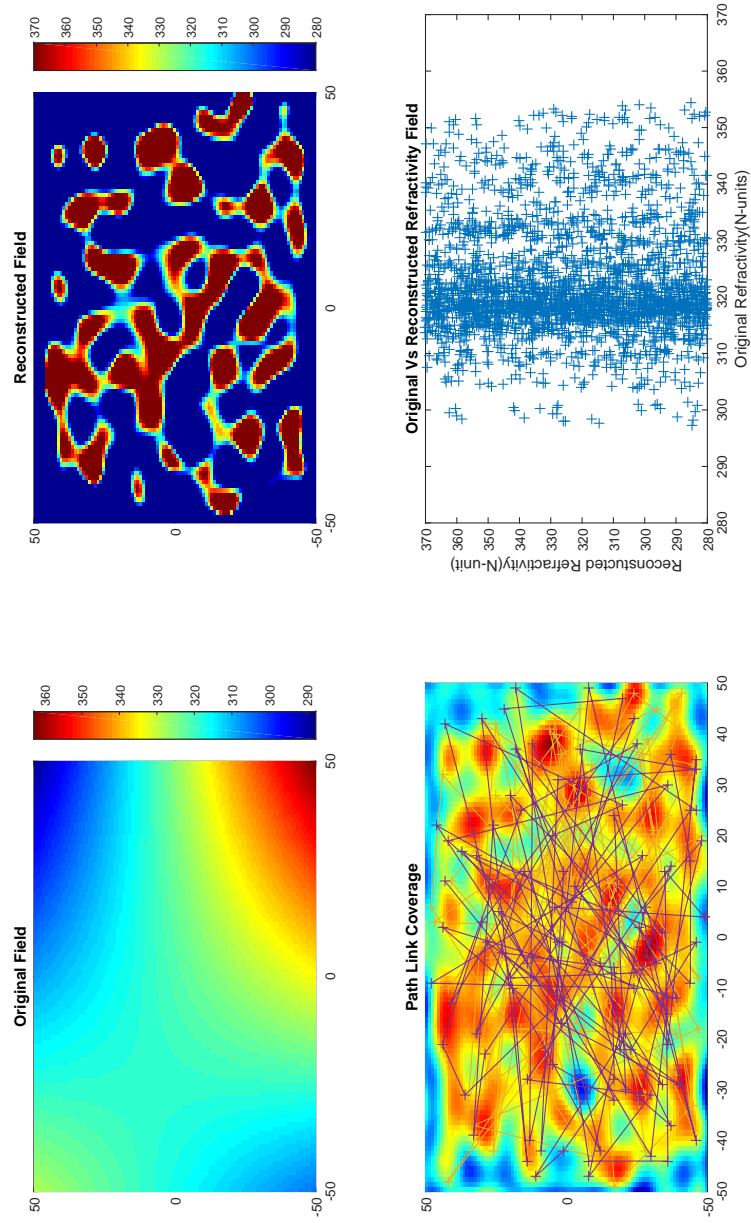


Figure 6-9: Case 1: Illustration of the reconstruction on a 100×100 scale with number of link = 100 and the min scale of the basis function = 5.

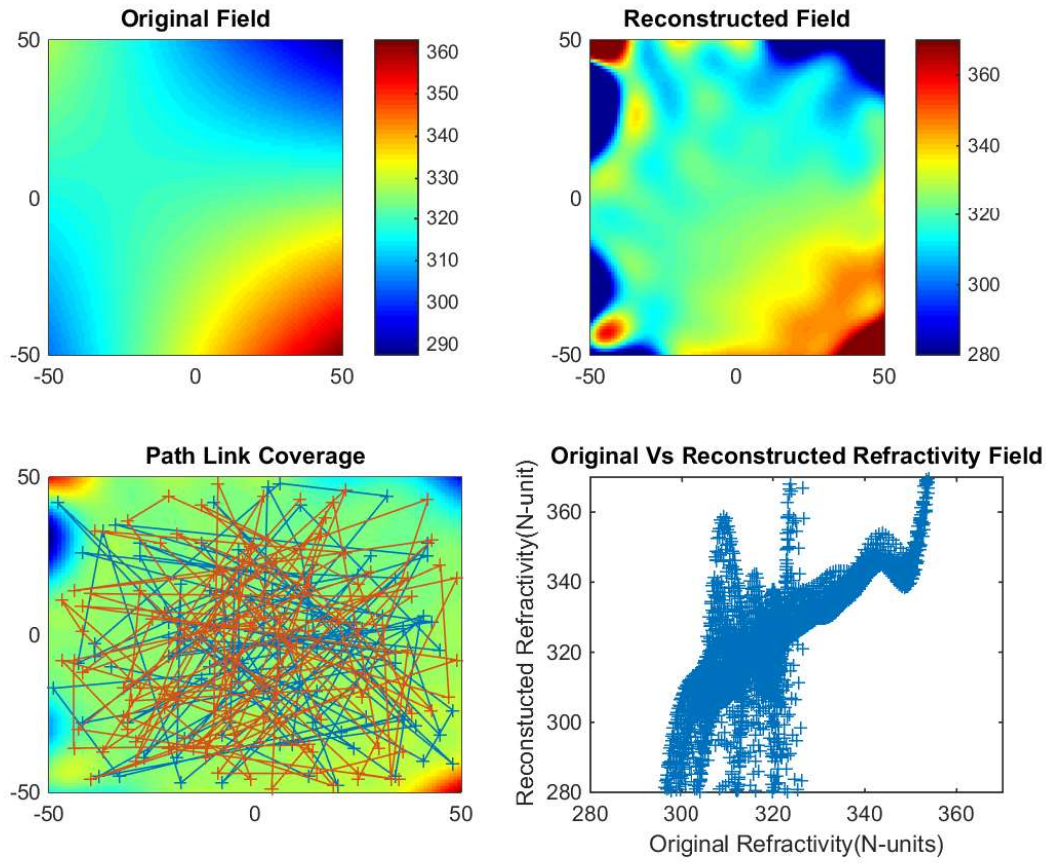


Figure 6-10: Case 2: Illustration of the comparison analysis of refractivity reconstruction from the original field on a 100×100 scale with number of link = 100 and the min scale of the basis function = 7.

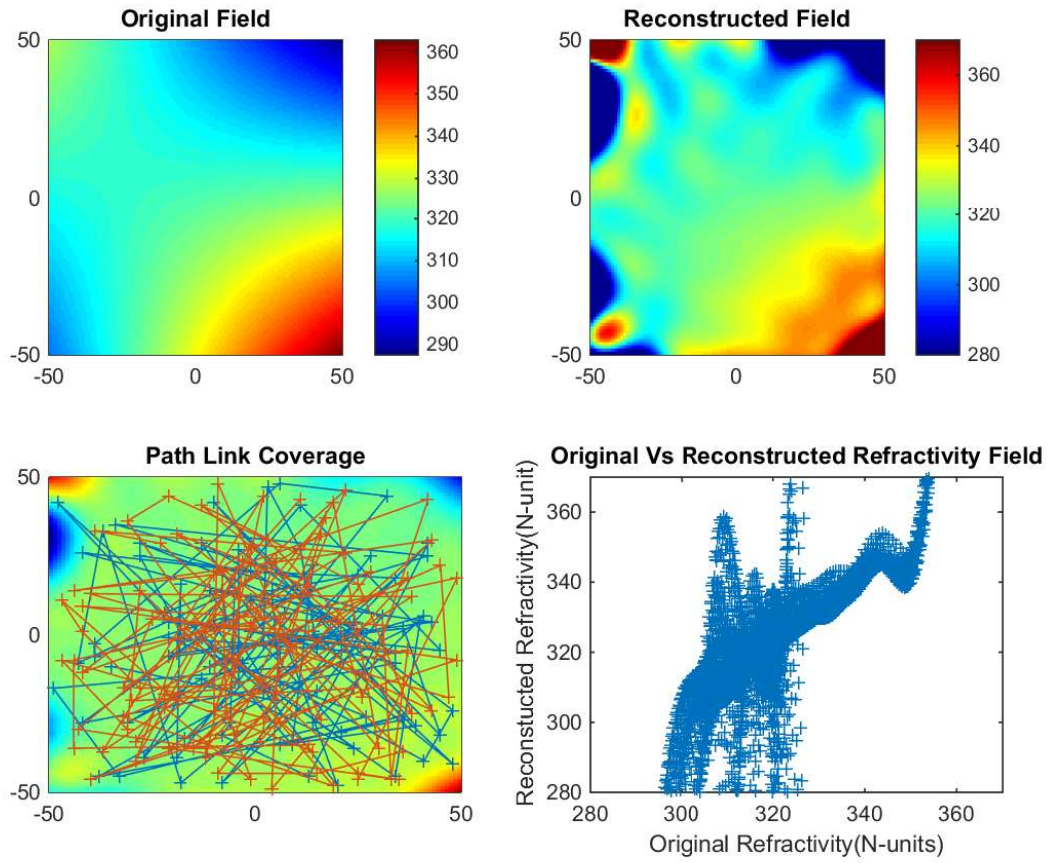


Figure 6-11: Case 3: Illustration of the comparison analysis of refractivity reconstruction from the original field on a 100×100 scale with number of link = 100 and the min scale of the basis function = 10.

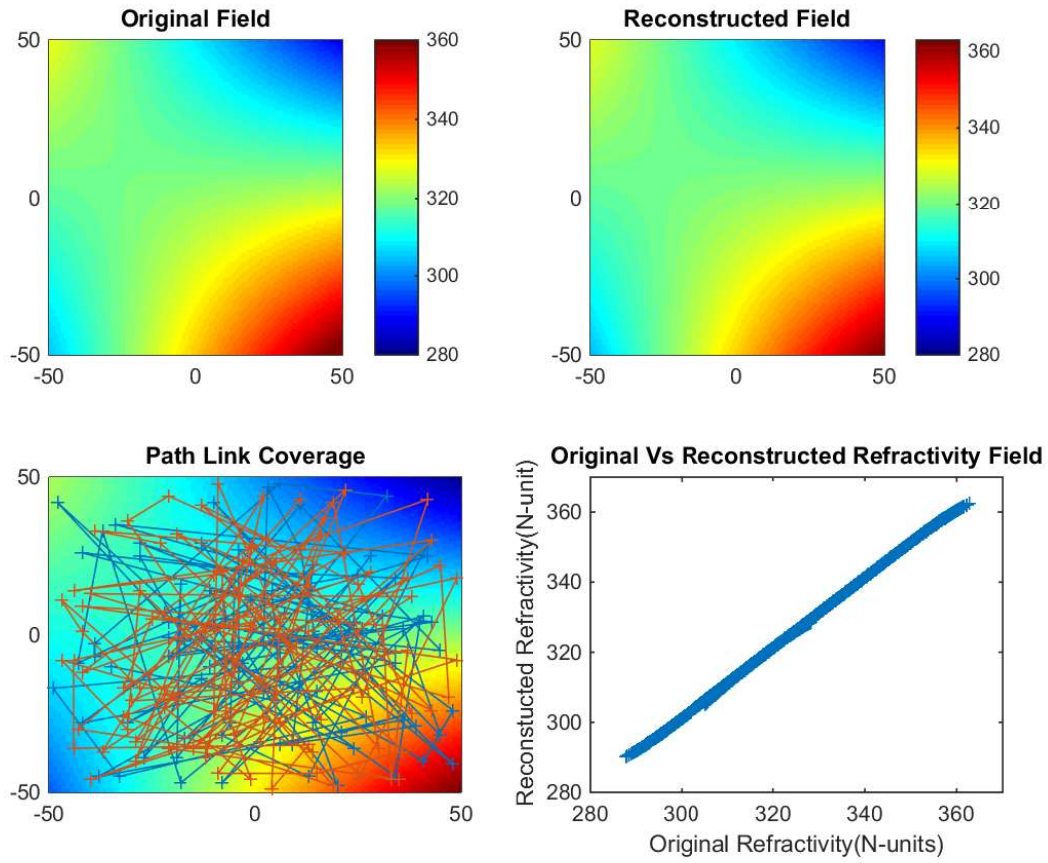


Figure 6-12: Case 4: Illustration of the comparison analysis of refractivity reconstruction from the original field on a 100×100 scale with number of link = 100 and the min scale of the basis function = 15.

RMS reconstruction error defines the RMS error between the reconstructed field and the original field. The refractivity value at every pixel of the reconstructed field was compared with the original refractivity field at that pixel. Figure 6-13 shown below represents the variation of the estimated mean RMS error reconstructed refractivity field (N-unit) with the varying number of the basis function. Each colour link represent a different number of links.

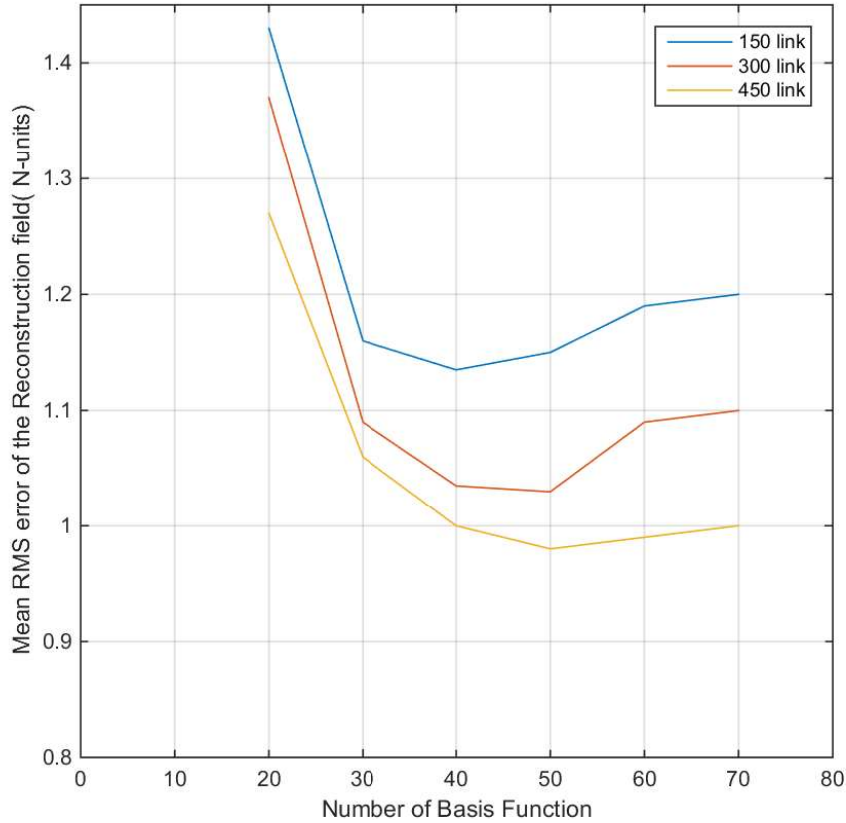


Figure 6-13: *RMS error analysis of the reconstruction field with the basis function for a 100×100 region.*

6.8.2 Varying the Number of Links

Here in this case we analyse to find the right value for the reconstruction variable. In comparison to the above section where we vary the basis function, here in this case we vary the number of links with constant basis function. Shown below in Figures 6-14 and 6-15 are some examples of the reconstructed refractivity fields obtained by varying the number of links. Figure 6-14 was reconstructed with a minimum scale of the basis function = 7 and the number of link = 200. From the comparison analysis between the Figure 6-14 and Figure 6-10, we see that by increasing the number of the links we have retrieved the original refractivity field with minimum error.

Figure 6-15 is another example showing the reconstruction with min scale of the basis function = 5, but with an increased number of links we can reconstruct the original refractivity field. For comparison analysis we see both the Figures 6-15 and 6-9, shows the difference and their dependency on the links and the basis function.

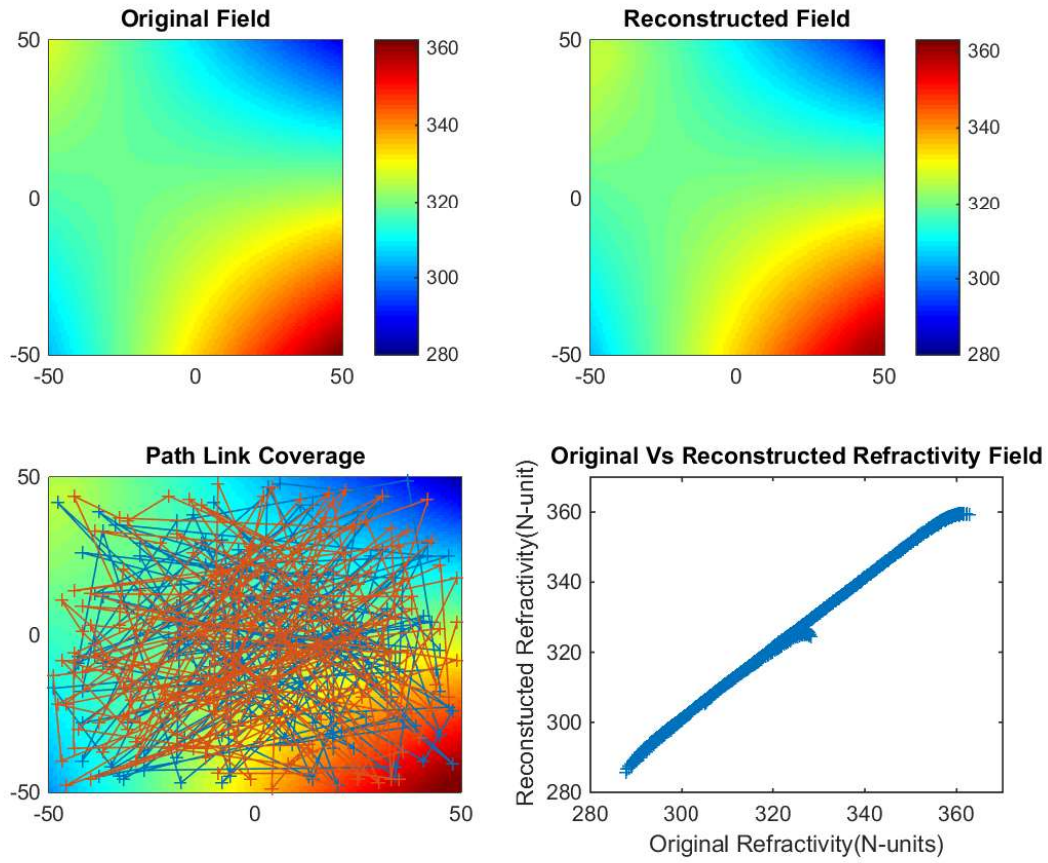


Figure 6-14: *Illustration of the analysis of refractivity reconstruction from the original field on a 100×100 scale with number of link = 200 and the min scale of the basis function = 7.*

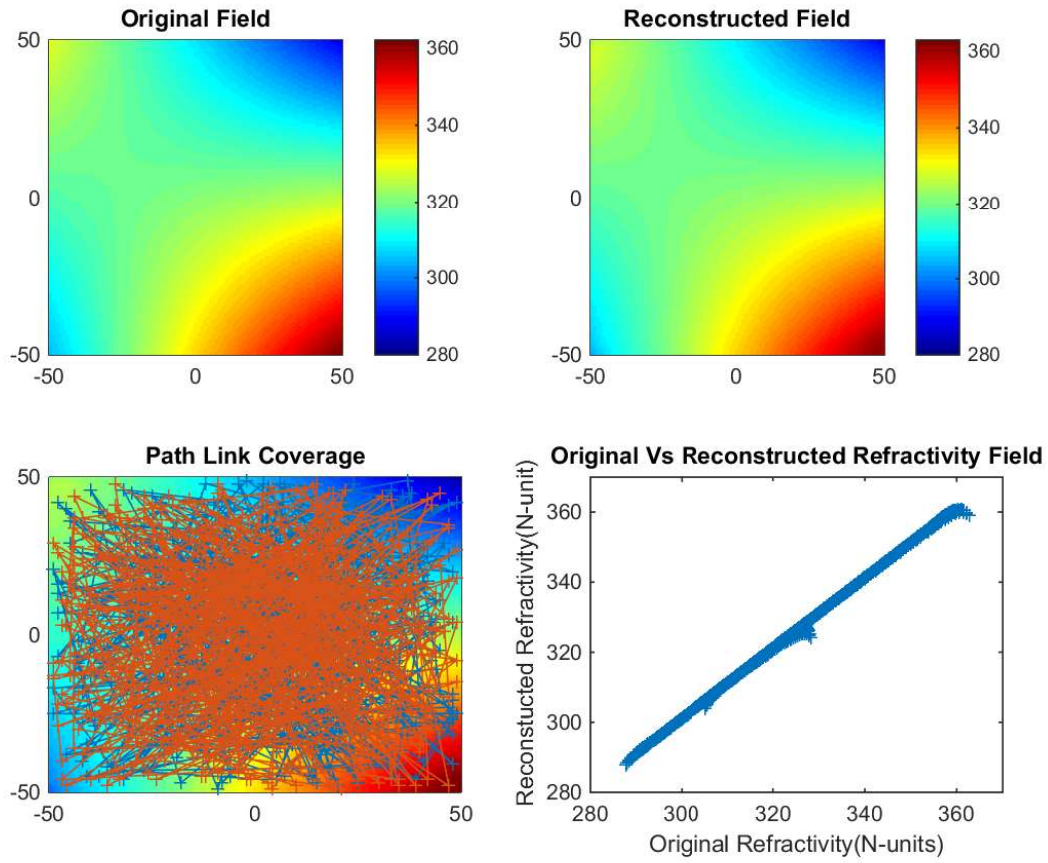


Figure 6-15: *Illustration of the analysis of refractivity reconstruction from the original field on a 100×100 scale with number of link = 450 and the min scale of the basis function = 5.*

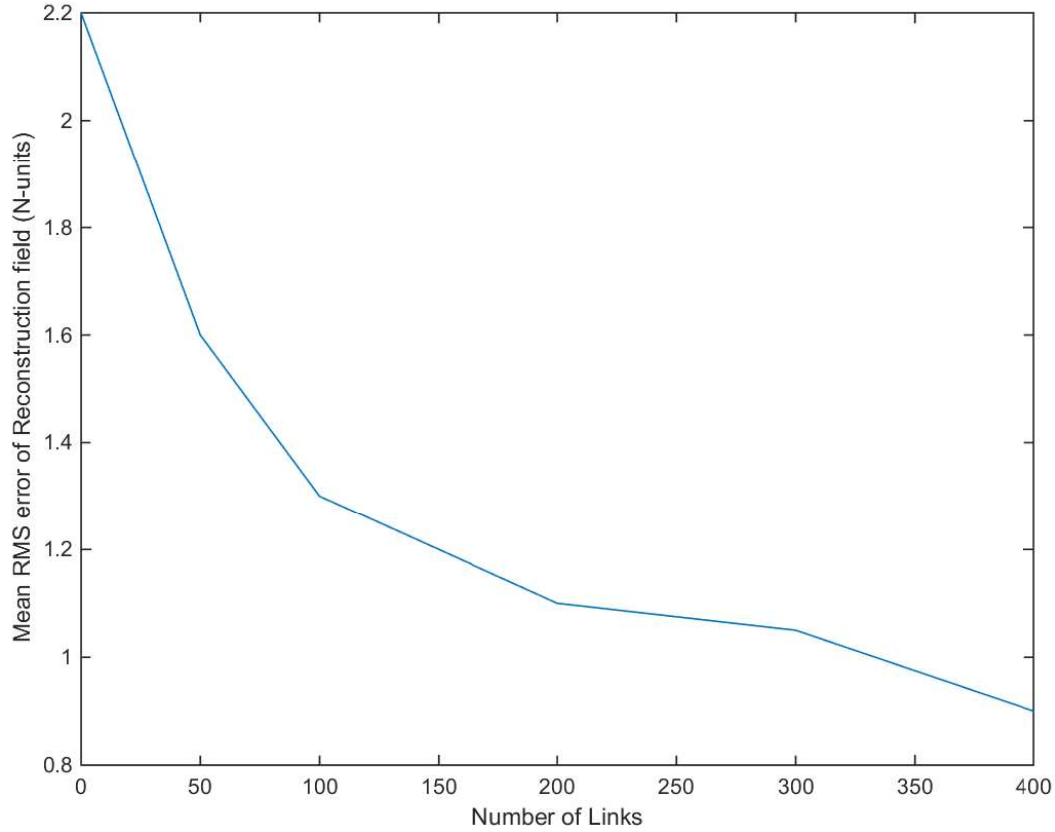


Figure 6-16: Variation of the mean averaged RMS error of the reconstructed field against the number of links.

Figure 6-16 is an Illustration showing the variation of the the rms reconstructed error against the number of links. We can notice from the figure, where as we increase the number of links, the mean reconstructed rms error of the reconstruction field also decreases. These results and analysis also show how both these variables are interdependent on each other to produce a desired reconstruction field.

6.9 Summary

In this chapter, we have shown an approach to extract the refractivity from the path link delay using the tomography inversion reconstruction technique. The description process of the inversion technique has been explained. The method-

ology for the PCA and the Gaussian basis function has been shown in detail. We have also shown the analysis of the results along with the rms reconstruction error analysis. In the next chapter we discuss about the conclusions and any further work of this research.

CHAPTER 7

CONCLUSIONS & FURTHER WORK

This chapter provides an overview of the key conclusions of this thesis and as well give a brief discussion into the possible further work for this research.

This thesis in Chapter 2 has examined the theory behind the propagation effects on the signal travelling through troposphere. The main topics which were included in this examination were the refractivity, delay terminologies and its characteristics and also the different existing water vapour/refractivity measurement instruments. This Chapter also focused on the requirement and needs for a better/improved, cost efficient remote sensing measuring technique. We have discussed the various remote sensing instruments such as radiosonde, GPS water vapour technique and radiometer for measuring the atmospheric refractivity. Also discussed in this chapter are the pros and cons of each of the existing instruments. These instruments are then compared with the DAB/DVB which is as shown in Table 2.1. The use of the DAB/DVB signals for the measurement of atmospheric refractivity was shown in Chapter 3. This chapter also showed the process of various steps involved in the tropospheric delay modelling.

Chapter 2 showed the need for a cheap, reliable and efficient based on the drawbacks of the existing remote sensing refractivity measurement technique. In Chapter 3, we have shown a novel approach in using the DAB/DVB for the measurement of tropospheric refractivity[1]. Chapter 3 described the entire process of using the DAB/DVB to measure atmospheric phase delay. The theory and background behind the DAB and DVB signals have been introduced. This Chapter

continued showing the DAB and DVB availability in the UK. Further in this study we have described in detail the experimental set-up and the equipments used for this experiment.

In chapter 3, we have also shown the different retrieval algorithm for phase delay estimation along with the advantages and drawbacks of each method. The different retrieval methods discussed in this study are namely single site autocorrelation, multi-site cross-correlation and the pilot symbol tracking[1]. The single site autocorrelation gives a simple low powered technique but requires the phase of the transmitter to be stable whereas the multi-site method doesn't require the phase of the transmitter to be stable.

In the later method, when there are two transmitter lying on the ellipse as shown in Figure 3.4, demodulation of signals is complex and difficult. Hence, we have seen that it requires only one transmitter to be lying on the foci of ellipse. Another method discussed was the pilot symbol tracking which uses a CAZAC symbol. This method still requires phase stability but can estimate the direct path between the transmitter and the receiver. The disadvantage of this method is high computation costs. Hence, the need for a forward modelling approach to study the accuracy and validation of using the DAB/DVB data as a sensor technology. This was then further validated using the process of Ray tracing modelling which was shown in Chapter 4.

In Chapter 4, we presented a tropospheric phase delay retrieval algorithm through the use of the ray tracing concept. We have discussed about the theory and background into ray tracing. Different ray tracing technique have been described. The most commonly used method are the ray shooting and the ray bending method. The ray tracing used in this study is a 2-dimensional method. Further we show the steps involved in the ray tracing algorithm to extract the path delay for the signal transmitted from the transmitter to the receiver. The ray tracing technique used during this was the ray brute force ray shooting method. Data for this ray tracing path delay estimation was used from the BADC radiosonde data. The ray tracing estimation process and its implementation using Eikonal equations has been shown in this chapter. The results and analysis of the ray tracing algorithm under different varying refractivity conditions was shown Chapter 5.

In Chapter 5, we have shown the analysis and simulation results for a wide range of varying atmospheric refractivity environment profile. Statistical analysis of the ray traced path delay was also shown and analysed. Comparison and relativity analysis of the ray traced delays were shown for different seasons was analysed and presented.

The ray traced path delay results obtained from the ray tracing algorithm showed existence of the path delay. This was obtained by taking the difference between the normal straight line path and the ray traced path. Ray tracing path delay between the Bath and Mendip showed an excess path delay of 8.5829m for the signal propagation in a varying refractive atmosphere. The normal propagation distance was around 26.32km. Another case of the analysis of the ray tracing of the signal propagation between Bath and Wenvoe for a distance of 66.3km resulted in an excess path delay of 21.67m. The step size chosen for both the analysis above was fixed at 10cm. The analysis of the ray tracing results using different combination of step size was also presented. From the analysis it was found that, increasing step size above 0.001km doesn't necessarily provide reduced path delay. As smaller and smaller step size would increase the computation time and with only a small negligible change in the excess delay which was as shown in the analysis in Chapter 5.

The chapter 5 we showed and examined the path delay variability to further gain an understanding of the delay variability. The statistical analysis of the ray traced delay was performed against the refractivity. The yearly refractivity analysis showed the higher variability of the mean refractivity during the months of the summer. During the winter months the refractivity variability was found to be low. The analysis of the mean averaged path delay over the year also showed an increase in the ray propagation path delay during the summer months. This analysis thereby illustrates relation between the delay and the season for refractivity variability. An analysis of the delay as a function of distance and the delay as a function of days was also presented in this chapter.

The main aim of determining the signal path delay of the ray propagation between the transmitter and the receiver is to use it in the process of tomographic inversion modelling technique. In Chapter 6, we have shown the approach of using the network of the path link delay to extract the refractivity for the field. The algorithm for the tomographic inversion reconstruction process has been shown and also covers the theory and the background of the inversion methodology. The calculation process of the principal component analysis(PCA) and the Gaussian basis function has also been shown in this chapter. The results from this methodology showed the reconstruction of the original refractivity using the path link delay. This was obtained by using the right combination of the basis function and also the right amount of the links. Different combination of this case of varying the basis function and by varying the number of the links has been demonstrated.

In the case of the analysis shown in Chapter 6, for a min scale of basis function =15 and the number of links = 100, the rms error obtained was 1.4 N-units. Although this results can also be obtained with an increase in the number of links to 200 and basis function min scale = 7. This analysis produces an rms error of approx 1.1 N-units. Hence we found that there is relation between the number of the basis function and the number of links. The analysis also shows the rms reconstruction error analysis between the reconstructed and the original field along the basis function and the number of links.

Opportunities exists to improve the inversion modelling further. Firstly, we can perform a field experiment by creating a network of link over an area of bath to perform inversion tomography. As this research covers the inversion using the Pseudo-inverse method, there is a further opportunity to perform analysis using various other inversion process such as the wavelet, Tikhnov regularization method to name a few. Further development of the ray tracing algorithm. Ray tracing modelling of the path delay can be further extended to the 3-dimensional. Due to the time constraint and since the focus of this project being on inversion we have considered the ray tracing using only the 2-dimensional space.

REFERENCES

- [1] R. J. WATSON, C. J. COLEMAN, “*The Use of Signals of Opportunity for the Measurement of Atmospheric Refractivity*”, Fourth European Conference on Antennas and Propagation, (EuCAP) 2010, pp. 1-6.
- [2] K. SHIMOSE, “*Two-dimensional Variational Analysis of Near-Surface Moisture from Simulated Radar Refractivity-Related Phase Change Observations*”, 13th Conference on IOAS-AOLS) AMS Meetings, 2009.
- [3] C. J. COLEMAN, R. J. WATSON AND H. J. YARDLEY, “*A Practical Bi-static Passive Radar System for Using With DAB and DRM Illuminators*”, IEEE Radar Conference, May, 2008.
- [4] F. K. BRUMMER AND W. M WELSCH (1993), , “*Effect of the Troposphere on GPS Measurements*”, GPS World, January 1993, pp. 42-51.
- [5] D. D. MCCARTHY, G. PETIT (2004), *IERS Conventions (2003) (IERS Technical Note 32)*, Frankfurt am Main: Verlag des Bundesamts für Kartographie und Geodesie, 2004. 127 pp.
- [6] V. B. MENDES , “*Modelling the Neutral-Atmosphere Propagation Delay in Radiometric Space Techniques*”, Ph.D. dissertation, Department of Geodesy and Geomatics Engineering Technical Report No. 199, University of New Brunswick, Fredericton, New Brunswick, Canada, 1999, 353 pp.
- [7] M. J. RUGGER, “*Refractive Index Formulae for Radio Waves*”, 12th International Congress, Washington, DC, April 19-26, 2002.

-
- [8] M. P. HALL, “*Effects of the Troposphere on Radio Communication*”, Peter Peregrinus LTD on behalf of the Institution of Electrical Engineers, 1979.
- [9] P. DEBYE (1929), “*Polar Molecules Dover*”, New York, 1929.
- [10] H. JAMES, R. LANGLEY, S. NEWBY (1991), “*Analysis of Tropospheric Delay Prediction Models: Comparisons with Ray-tracing and Implications for GPS Relative Positioning*”, Bulletin Geodesique, Vol. 65, No. 3, pp. 151-161.
- [11] Y. E. BARSERVER, P. M. KROGER, J. A. BORJESSON, “*Estimating Horizontal Gradients of Tropospheric Path Delay with a Single GPS Receiver*”, Journal of Geophysical Research, vol 103, No. B3: 5019-5035, 1998.
- [12] M. BEVIS, S. BUSINGER, T. A. HERRING, C. ROCKEN, R. A. ANTHES, R. H. WARE, “*GPS Meteorology: Remote Sensing of Atmospheric Water Vapor Using the Global Positioning System*”, Journal of Geophysical Research, Vol. 97, No. D14, October 20, pp. 15, 787-15,801, 1992.
- [13] L. YUAN, R. ANTHES, R. WARE, C. ROCKEN, W. BONNER, M. BEVIS, S. BUSINGER, “*Sensing Climate Change using the Global Positioning System*”, Journal of Geophysical Research, 98, 14, 925-14, 937, 1993.
- [14] W. F. DABBERDT, “*Meteorological Research Needs for Improved Air Quality Forecasting*”, Report of the 11th Prospectus Development Team of the U.S. Weather Research Program, Bull. Amer. Meteorology. Soc., 85, 563, 2004.
- [15] COSTER, A. A. NIELL, F. SOLHEIM, V. MENDES, P. TOOR, R. LANGLEY, C. RUGGLES, “*The Westford Water Vapor Experiment: Use of GPS to Determine Total Precipitable Water Vapor*”, Proceedings of the Institute of Navigation 52nd Annual Meeting, Cambridge, MA, USA, 529-538, 19-21 June 1996.
- [16] R. GHODDOUSI-FARD, P. DARE, “*A Climatic Based Asymmetric Mapping Function Using a Dual Radiosonde Ray Tracing Approach*”, Proceedings of the 20th International Technical Meeting of the Satellite Division of the Institute of Navigation-ION GNSS 2007, The Institute of Navigation, Fort Worth, Tex., September 25-28, pp. 2870-2879, 2007.
- [17] R. WARE, C. ROCKEN, F. SOLHEIM, T. VAN HOVE, C. ALBER, AND J. JOHNSON, “*Pointed Water Vapour Radiometer Corrections for Accurate*
-

-
- Global Positioning System Surveying*", Journal of Geophysical Research, 20, 2635-2638, 1993.
- [18] D. HOGG, F. GUIRAUD, AND M. DECKER , "*Measurement of Excess Radio Transmission Length on Earth-Space Paths*", Astron. Astrophys., 95, 304-307, 1981.
- [19] C. ROCKEN, R. WARE, T. VAN HOVE, F. SOLHEIM, C. ALBER, J. JOHNSON, "*Sensing Atmospheric Water Vapour with the Global Positioning System*", Geophys. Res. Lett., 20, 2631-2634, 1993.
- [20] A. NIELL , "*Global Mapping Functions for the Atmosphere Delay at Radio Wavelengths*", Journal of Geophysical Research, 101, 3227-3246, 1996.
- [21] S. BUSINGER, S. CHISWELL, M. BEVIS, J. DUAN, R. ANTHES, C. ROCKEN, R. WARE, T. VAN HOVE, F. SOLHEIM, "*The Promise of GPS in Atmospheric Monitoring*", Bull. Am. Meteorol. Soc., 77, 5-18, 1996.
- [22] S. SAHOO , "*Increasing Vertical Resolution of three-Dimensional Atmosphere Water Vapour Retrievals Using a network of Scanning Compact Microwave Radiometers*", Colorado State University Fort Collins, Colorado Spring, 2011.
- [23] F. ITURBIDE-SANCHEZ, S. C. REISING AND S. PADMANABHAN, "*A Miniaturized Spectrometer Radiometer Based on MMIC Technology for Tropospheric Water Vapour Profiling*", IEEE Trans. Geoscience. Remote Sensing, vol. 44, no. 7, pp. 2181-2193, Jul. 2007.
- [24] AGNES LIGETI, "*Frequency Network Planning, Radio Communication Laboratory, the Royal Institute of Technology*", The Royal Institute of Technology, Department of Signals Sensors and Systems, 1999.
- [25] B. BEAN, E. DUTTON, "*Radio Meteorology*", National Bureau of Standards Monograph 92, Washington, DC, 1966.
- [26] J. W. MARINI, "*Correction of Satellite Tracking Data for an Arbitrary Tropospheric Profile*", Radio Sci., 7, 223-231, 1972.
- [27] H. YAN, J. PING, "*The Generator Function Method of the Tropospheric Refraction Corrections*", Astron J 110(2):934-993, 1995.
-

-
- [28] J. BOEHM, B. WERL, H. SCHUH , “*Troposphere Mapping Functions for GPS and Very Long Baseline Interferometry from European Centre for Medium-Range Weather Forecasts Operational Analysis Data*”, Journal of Geophysical Research, 111:B02406, 2006.
- [29] J. L. DAVIS, T. A. HERRING, I. I. SHAPIRO, A. E. ROGERS, G. ELGERED , “*Geodesy by Radio Interferometry Effects of Atmospheric Modelling Errors on Estimates of Baseline Length*”, Radio Sci., 20, 1593-1607, 1985.
- [30] R. N. THESSIN, “*Atmospheric Signal Delay Affecting GPS Measurements Made by Space Vehicles During Launch, Orbit and Re-entry*”, Master’s Thesis, Massachusetts Institute of Technology, Department of Aeronautics and Astronautics, Cambridge, Mass., 182 pp, 2005.
- [31] N. RAWLINSON, J. HAUSER, M. SAMBRIDGE , “*Seismic Ray Tracing and Wavefront Tracking in Laterally Heterogeneous Media*”, In Advances in Geophysics, ed. R. Dmowska, Vol. 49, Academic Press/Elsevier, Amsterdam, ISBN 9780123742315, pp. 203-267, doi: 10.1016/S0065-2687(07)49003-3, 2008.
- [32] L. SEVGI, “*A Ray Shooting Visualization Matlab Package for 2-D Ground-wave Propagation Simulations*”, IEEE Antennas and Propagation Magazine, Vol. 46, No 4, pp.140-145, Aug 2004.
- [33] M. BORN, E. WOLF, “*Principles of Optics: Electromagnetic Theory of Propagation, Interference and Diffraction of Light*”, 7th ed., 986 pp., Cambridge University Press, Cambridge, U.K., ISBN 0521642221, doi: 10.2277/0521642221, 1999.
- [34] F. G. NEIVINSKI(2009), “*Ray-tracing Options to Mitigate the Neutral Atmosphere Delay in GPS*”, M.Sc. thesis, University of New Brunswick, Dept. of Geodesy and Geomatics Engineering, Fredericton, N.B., Canada, May, 232 pp., Technical Report 262, 2009.
- [35] T. HOBIGER, R. ICHIKAWA, Y. KOYAMA, T. KONDO (2008A), “*Fast and Accurate Ray-tracing Algorithms for Real-time Space Geodetic Applications Using Numerical Weather Models*”, Journal of Geophysical Research, Vol. 113, No. D20, doi: 10.1029/2008JD010503, 2008.
-

-
- [36] T. HOBIGER, R. ICHIKAWA, T. TAKASU, Y. KOYAMA, T. KONDO (2008B), “*Ray-traced Troposphere Slant Delays for Precise Point Positioning*”, *Earth, Planets and Space*, Vol. 60, No. 5, pp. e1-e4, <http://www.terrapub.co.jp/journals/EPS/pdf/2008e/6005e001.pdf>
- [37] T. A. HERRING, “*Modelling Atmospheric Delays in the Analysis of Space Geodetic Data*”, *Proceedings of the Symposium Refraction of Trans-atmospheric Signals in Geodesy*, eds. J. C. deMunck, and T. A. TH. Spoelstra, No. 36, Netherlands Geodetic Commission, The Hague, The Netherlands, May 19-22, ISBN 9789061322436, pp. 157-164. <http://www.ncg.knaw.nl/eng/publications/Geodesy36DeMunck.html>, 1992.
- [38] T. PANY, P. PESEC, G. STANGL (2001). , “*Elimination of Tropospheric Path Delays in GPS Observations With the ECMWF Numerical Weather Model*”, *Physics and Chemistry of the Earth, Part A: Solid Earth and Geodesy*, Vol. 26, No. 6-8, pp. 487-492, doi:10.1016/S1464-1895(01)00089-8, 2001.
- [39] A. LIGETI , “*Single Frequency Network Planning, Radio Communication Laboratory*”, The Royal Institute of Technology, Department of Signals Sensors and systems, 1999.
- [40] R. WATSON, D. HODGES, “*Estimation of Rainfall Rate from Terrestrial Microwave Link Measurements*”, *Geoscience and Remote Sensing Symposium: IEEE International: IGARSS 2009. Vol.3. IEEE*, III26-III266. (International Geoscience and Remote Sensing Symposium (IGARSS)),2009.
- [41] C. TANNOUS, J. NIGRIN, “*Ray-Tracing Studies in a Perturbed Atmosphere: I- The Initial Value Problem*”, 2001.
- [42] M. S. SAMBRIDGE, B. L. N. KENNET (1990), “*Boundary Value Ray Tracing in a Heterogeneous Medium: A Simple and Versatile Algorithm*”, *Geophys. J. Int.* 101, 157-168, 1990.
- [43] V. PEREYRA, W. H. K. LEE, H. B. KELLER(1980), “*Solving Two-point Seismic-ray Tracing Problems in a Heterogeneous Medium*”, *Bull. Seismic. Soc. Am.* 70, 79-99, 1980.
- [44] B. R. JULIAN, D. GRUBBINS, “*Three-Dimensional Seismic Ray Tracing*”, *Journal of Geophysical Research.* 43,95-113, 1977.
-

-
- [45] V. CERVENY , “*Seismic Ray Theory*”,Cambridge University Press, Cambridge, 2001.
- [46] D. GIULI, A. TOCCAFONDI, G. BIFFI GENTILI, A FRENI, “*Tomographic Reconstruction of Rainfall Fields Through Microwave Attenuation Measurements*”,J. Appl. Meteorology., vol. 30, pp.1323-1340, September 1991.
- [47] D. GIULI, L. FACHERIS, S TANELLI, “*Microwave Tomographic Inversion Technique Based on Stochastic Approach for Rainfall Fields Monitoring*”,IEEE Transactions on Geoscience and Remote Sensing, vol. 37, no. 5, pp. 2536-2555, September 1999.
- [48] H. MESSER, A. ZINEVICH, P. ALPERT, “*Environmental Monitoring by Wireless Communication Networks*”,Science, vol. 312,pp.713, May 2006.
- [49] A. ZINEVICH, P. ALPERT, H. MESSER, “*Estimation of Rainfall Fields using Commercial Microwave Communication networks of variable link density*, *Advances in Water Resources*, vol.31, pp. 1470-1480, November 2008.
- [50] S. ZHENG, F. HAN-XIAN , “*Inversion for Atmosphere Duct Parameters using Real Radar Sea Clutter*”,Chin. Phys. B Vol. 21, No.2, 2012.
- [51] A. FLORES, G. RUFFINI, A. RIUS, , “*4D Tropospheric Tomography using GPS Slant Wet Delays*”, Ann. Geophys., 18, 223-234, 2000.
- [52] C. ROCKEN, J. BRAUN, T. VANHOVE, J. JOHNSON, B. KUO,, “*Developments in Ground-based GPS Meteorology. Presentation at International Workshop on GPS Meteorology*”, Tsukuba, Japan, Meteorological Society of Japan, 11, 1.01.1- 1.01.6., 2003.
- [53] A. E. MACDONALD, Y. F. XIE , “*On The Use of Slant Observations from GPS to Diagnose Three Dimensional Water Vapour using 3DVAR. Presentation at Fourth Symposium on Integrated Observing Systems*”, Ann. Geophys., 18, 223-234, 2000.
- [54] M. C. VOWLES, “*An Investigation of Tropospheric Refractive Effects On Ka - Band terrestrial Links* ”, Ph.D thesis work, University of Bath, Department of Electronic and Electrical Engineering, July 2006.
- [55] B. GOUDAR, R. J. WATSON, “*Variability in Propagation Path Delay for Atmospheric Remote Sensing*”, Geoscience and Remote Sensing Symposium (IGARSS), IEEE International, 2014.
-

-
- [56] R. J. WATSON, N. DUMONT, B. WILTSHIRE AND C. COLEMAN, “*Measurement of Atmospheric Refractivity Using Signals of Opportunity*”, Geoscience and Remote Sensing Symposium (IGARSS), IEEE International, 2012.
- [57] V. NAFISI, “*Ray-Traced Tropospheric Delays in VLBI Analysis*”, Radio Science, 2012.
- [58] SENDIK, OMRY AND H. MESSER, “*On the Achievable Coverage of Rain Field Mapping Using Measurements from a Given Set of Microwave Links*”, 2014 IEEE 28th Convention of Electrical & Electronics Engineers in Israel(IEEEI), 2014.
- [59] A. A. JALBANI, “*Single Frequency Network*”, Institute for Informatik, University of Goettingen, 2012.
- [60] R. GHODDOUSI-FARD, “*A Web-Based Package for Ray Rracing the Neutral Atmosphere Radiometric Path Delay*”, Computers and Geosciences, 2009.
- [61] J. NETO, “*Principal Component Analysis*”, Department of Computer Science, University of Lisbon, 2013.
- [62] A. T. ADEDIJI, “*Microwave Anomalous Propagation(AP) Measurement Over Akure South-Western Nigeria*”, Journal of Atmospheric and Solar-Terrestrial Physics, 2010.
- [63] V. GRIMM, “*On the Use of the Gautschi - Type Exponential Integrator for Wave Equations*”, Numerical Mathematics and Advanced Applications, 2006.
- [64] L. FERAL, H. SAUVAGEOT, L. CASTANET, AND J. LEMORTON , “*A New Hybrid Model of the horizontal Distribution for Propagation Studies: 1. Modelling of the Rain Cell*”, Radio Science, 2003.
- [65] P. MUVVALA, “*Feasibility of Troposphere Propagation Delay Modeling of GPS Signals using Three-Dimensional Weather Radar Reflectivity Returns*”, Russ College of Engineering and Technology of Ohio University, 2011.
- [66] M. TURK, A. PENTLAND, “*Eigenfaces for Recognition*”, Journal of Cognitive Neuroscience, 1991.
- [67] P. PRATS-IRAOLA, “*High precision SAR focusing of TerraSAR-X experimental staring spotlight data*”, IEEE IGARSS, 2012.
-

- [68] Z. YU, Z. LI, AND S. WANG, “*An imaging compensation algorithm for correcting the impact of tropospheric delay on spaceborne high-resolution SAR*”, IEEE Trans. Geo. & Rem. Sens, vol 53, pp 4825-4835, 2015.
- [69] R. J. WATSON AND N. DUMONT, “*Measurement of atmospheric refractivity using digital audio broadcast radio signals*”, EuCAP 2013.
- [70] R. GHODDOUSI-FARD, “*Modelling tropospheric gradients and parameters from NWP models: Effects of GPS estimates*”, 2009.
- [71] P-C. HANSEN, D. P. O’LEARY, “*The use of the L-curve in regularization of discrete ill-posed problems*”, vol. 14, no. 6, pp. 1487-1503, November 1993.